Vol. 17 No. 1 June 2020

P-ISSN 0216-6739; E-ISSN 2549-516X
Accreditation No. 30/E/KPT/2018

International Journal of Remote Sensing and Earth Sciences

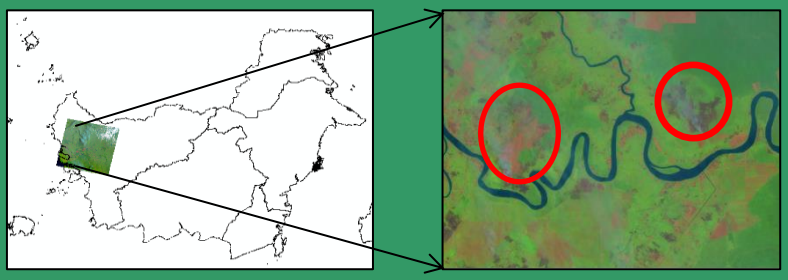

Vol. 17 No. 1 June 2020

P-ISSN 0216-6739; E-ISSN 2549-516X
Accreditation No. 30/E/KPT/2018

Published by
Indonesian National Institute of Aeronautics and Space
(LAPAN)

International Journal of Remote Sensing and Earth Sciences

Published by
Indonesian National Institute of Aeronautics and Space
(LAPAN)

Editorial Committee Preface

Dear IJReSES Readers,

We sincerely thank you for reading the International Journal of Remote Sensing and Earth Sciences Vol. 17 No 1, June 2020. In general, this journal is expected to enrich the serial publications on earth sciences. In particular this journal is aimed to present improvement in remote sensing studies and its applications on earth sciences. This journal also serves as the enrichment on earth sciences publication, not only in Indonesia and Asia but also worldwide.

This journal consists of papers discussing the particular interest in remote sensing field. Those papers are having remote sensing data for image processing, geosciences, oceanography, environment, disaster, mining activities, etc. A variety of topics are discussed in this seventeen edition. Briefly, the topics discussed in this edition are the studies of remote sensing data processing issues such as rice field classification, potential fishing zone, burned areas, total suspended solid, land surface temperature change, and bathymetri. There some new methods, new analysis, and new novelties on this edition.

Finally, enjoy your reading of the IJRESES Vol. 17 No. 1 June 2020, and please refer this journal content for your next research and publication. For editorial team members and the journal secretariat, thank you very much for all big supports for this volume publication.

Editor-in-Chief,

Dr M. Rokhis Khomarudin

Vol. 17 No. 1 June 2020
P-ISSN 0216-6739; E-ISSN 2549-516X

Contribution Paper to:

IJReSES Secretariat
Indonesian National Institute of Aeronautics and Space (LAPAN)
Jl. Kalisari No. 8, Pekayon, Pasar Rebo, Jakarta 13710, INDONESIA
Telp. (021) 8710065, Fax. (021) 8722733
www.jurnal.lapan.go.id

Published by:
National Institute of Aeronautics and Space of Indonesia
(LAPAN)

INTERNATIONAL JOURNAL OF
REMOTE SENSING AND EARTH SCIENCES
Vol. 17 No. 1 June 2020
P-ISSN 0216-6739; E- ISSN 2549-516X
Accreditation No. 30/E/KPT/2018

Contents

Published by:
National Institute of Aeronautics and Space of Indonesia (LAPAN)

DETECTING THE SURFACE WATER AREA IN CIRATA DAM UPSTREAM CITARUM USING A WATER INDEX FROM SENTINEL-2

Suwarsono[1,2*], Fajar Yulianto[1], Hana Listi Fitriana[1,3], Udhi Catur Nugroho[1], Kusumaning Ayu Dyah Sukowati[1], Muhammad Rokhis Khomarudin[1]

[1]Remote Sensing Application Center, LAPAN

[2]Department of Physics, Faculty of Mathematic and Natural Sciences, Universitas Indonesia

[3]Department of Geography, Faculty of Mathematic and Natural Sciences, Universitas Indonesia

*e-mail: suwarsono@lapan.go.id / suwarsono81@ui.ac.id

Received: 31 December 2019; Revised: 20 February 2020; Approved: 17 June 2020

Abstract. This paper describes the detection of the surface water area in Cirata dam, upstream Citarum, using a water index derived from Sentinel-2. MSI Level 1C (MSIL1C) data from 16 November 2018 were extracted into a water index such as the NDWI (Normalized Difference Water Index) model of Gao (1996), McFeeters (1996), Roger and Kearney (2004), and Xu (2006). Water index were analyzed based on the presence of several objects (water, vegetation, soil, and built-up). The research resulted in the ability of each water index to separate water and non-water objects. The results conclude that the NDWI of McFeeters (1996) derived from Sentinel-2 MSI showed the best results in detecting the surface water area of the reservoir.

Keywords: *Surface water area, NDWI, Sentinel-2, Cirata dam, Upstream Citarum*

1 INTRODUCTION

Remote sensing technology has long been utilised in water assessment and coastal management (Xu, 2006). These applications have involved the identification of water surfaces and other matters related to the object, such as floods and soil moisture.

Optical sensors capable of acquiring visible and near infrared wavelengths are essential for monitoring the objects and other phenomena. The Normalized Difference Water Index (NDWI), an index measured using Near Infrared (NIR) 0.86 μm and Short Wave Infra Red (SWIR) 1.24 μm, was first proposed by Gao (1996) to detect the liquid water content of vegetation canopies.

The NDWI of Gao is calculated as follows:

$$NDWI = \frac{\rho 0.86 - \rho 1.24}{\rho 0.86 + \rho 1.24} \quad (1\text{-}1)$$

where ρ0.86 μm is the reflectance value of the NIR 0.86 μm band, and ρ1.24 is that of the SWIR 1.24 μm band.

NDWI was later developed to delineate surface water features and enhance their presence in remotely-sensed digital imagery (McFeeters, 1996). The NDWI of McFeeters is calculated as follows:

$$NDWI = \frac{\rho Green - \rho NIR}{\rho Green + \rho NIR} \quad (1\text{-}2)$$

where ρGreen is the reflectance value of the green channel, and ρNIR is that of NIR channel.

In spite of the fact that McFeeters' and Gao's NDWIs employ the same terminology, the concepts of the two NDWIs are totally distinctive. Gao's NDWI is measured as the normalized difference between the NIR and SWIR wavelengths. Other researchers, Rogers and Kearney (2004),

http://dx.doi.org/10.30536/j.ijreses.2020.v17.a3286

preferred red and SWIR bands (channels 3 and 5 of Landsat TM) to generate NDWI, as follows:

$$NDWI = \frac{\rho Red - \rho SWIR}{\rho Red + \rho SWIR} \quad (1\text{-}3)$$

Xu (2006) found that McFeeters' NDWI was incapable of totally separating built-up objects from water objects. The modification of the NDWI by employing a MIR channel instead of an NIR band can substantially improve the enhancement of open water objects, and can rapidly and precisely segregate water from non-water objects. To compensate for this disadvantage of McFeeters' NDWI, Xu (2006) proposed a modified NDWI (MNDWI), in which the SWIR band was utilised to replace the NIR channel in McFeeter's NDWI formula:

$$MNDWI = \frac{\rho Green - \rho SWIR}{\rho Green + \rho SWIR} \quad (1\text{-}4)$$

Ding (2009) developed the new water index (NWI) using four spectral bands from blue to the MIR region. In this new index, the green band was replaced by the blue band, and the NIR band was replaced by the total reflectance from three infrared bands in Landsat TM imagery. The index is measured as follows:

$$NWI = \frac{\rho Blue - (\rho NIR + \rho SWIR1 + \rho SWIR2)}{\rho Blue + (\rho NIR + \rho SWIR1 + \rho SWIR2)} \quad (1\text{-}5)$$

where ρBlue is the reflectance on the blue band, corresponding to Band 1 in TM imagery. SWIR1 and SWIR2 are two SWIRs, corresponding to Bands 5 and 7 in TM imagery respectively.

Several studies have showed that the normalized difference water index (NDWI) has been successfully used to delineate surface water features better than other indices. Wang et al. (2017) succesfully applied the normalized difference water index (NDWI) and the modified normalized difference water index (MNDWI) to Landsat time-series images during the period 1976–2015 to discriminate surface water and land features in order to understand the spatio-temporal changes of the Ningbo coastline.

Du et al. (2012), who conducted research on estimating surface water area changes using time-series Landsat data in the Qingjiang River Basin, China, found that NDWI and MNDWI could extract surface water areas from Landsat data and could also be used to monitor surface water dynamic changes and detect flood disasters.

Spectral water indices, such as the normalized difference water index (NDWI) (McFeeters, 1996) and modified NDWI (MNDWI) (Xu, 2006), can extract water body information more accurately, quickly and easily than supervised/unsupervised classification methods (Li et al., 2013). Szabo et al. (2016) found that water-related indices (NDWI, MNDWI) were more effective in enhancing water features.

Acharya et al. (2016) compared the NDVI, NDWI and MNDWI to detect the changes in lakes in Pokhara, Nepal using Landsat data. Their results show the NDWI gave better results than NDVI and MNDWI. In addition, Ashraf et al. (2015) conducted change detection analysis using the NDVI, NDWI, MNDWI and NDMI (Normalized Difference Moisture Index) from Landsat multitemporal data (Landsat-2, Landsat-4, Landsat-5, Landsat-7 and Landsat-8), and showed that NDWI performed better than the other indices in all the related base years and also had the best accuracy with the ground.

Until now, water surface identification and mapping based on water indices has been dominated by the use of optical images from Landsat TM,

ETM+ and OLI data. However, ESA's newest generation of medium-resolution optical satellites, Sentinel-2, are now available.

Sentinel-2 is a European wide swath, high resolution, multispectral imaging mission. The twin satellites of Sentinel-2 (Sentinel-2A and Sentinel-2B) will provide continuity of SPOT and Landsat-type image data (ESA, 2015). Sentinel-2 carries an optical instrument payload of a Multi Spectral Instrument (MSI), consisting of 13 spectral bands spanning from the visible, to the near infrared, and to the short wave infrared. The spatial resolution varies from 10 m to 60 m, depending on the spectral band, with a 290 km field of view. This unique combination of high spatial resolution, wide field of view and spectral coverage will represent a major step forward compared to current multi-spectral missions. The mission foresees a series of satellites, each having a 7.25-year lifetime over a 15-year period, starting with the launch of Sentinel-2A in 2013. Sentinel-2 will directly contribute to the land monitoring, emergency response, and security services (Drusch et al., 2012).

Table 1-1: Sentinel-2 spectral specification (ESA, 2013)

Band number	Central wavelength (µm)	Bandwidth (nm)	Resolution (m)
1	0.443	20	60
2	0.490	65	10
3	0.560	35	10
4	0.665	30	10
5	0.705	15	20
6	0.740	15	20
7	0.783	20	20
8	0.842	115	10
8A	0.865	20	20
9	0.945	20	60
10	1.375	30	60
11	1.610	90	20
12	2.190	180	20

Sentinel-2 data are acquired on 13 spectral bands in the VNIR and SWIR, with four bands at 10 m: 490 nm (B2), 560 nm (B3), 665 nm (B4), 842 nm (B8); six bands at 20 m: 705 nm (B5), 740 nm (B6), 783 nm (B7), 865 nm (B8A), 1 610 nm (B11), 2 190 nm (B12); and three bands at 60 m: 443 nm (B1), 945 nm (B9) and 1.375 nm (B10) (ESA, 2015) (Table 1-1).

Figure 1-1: Location of the study area, Cirata dam, a large reservoir located on upstream Citarum, West Java Province. Map source: http://landsat-catalog.lapan.go.id

Considering the spectral and spatial characteristics of the MSI Sentinel-2, it is clear that these imagery data have the potential to be used in the identification and mapping of water surface areas.

This research was conducted to attempt to use the MSI Sentinel-2 imagery to identify surface water areas using several water indices in regions in Indonesia. The chosen location was the Cirata dam, a large reservoir located on upstream Citarum, West Java Province (Figure 1-1).

2 MATERIALS AND METHODOLOGY

2.1 Data

Sentinel-2 MSI Level 1C (MSIL1C) data were used in this research. Their acquisition date was 16 November 2018, with a coverage of around 106:48:27.51E / 6:19:45.67S (Top Left) - 107:48:19.24E / 7:19:1.24S (Bottom Left). This coverage covers most regions of upstream Citarum. The data were obtained from the European Space Agency (ESA) through the Copernicus Open Access Hub.

The Sentinel-2 MSI Level-1C (MSIL1C) has ortho-rectified and UTM geocoded Top-of-Atmosphere Reflectance with sub-pixel multispectral and multi-date registration. The tile covers a 100x100km UTM tile covered within one orbit (ESA, 2015). The MSIL1C tile consists of a Level-1C_Tile_Metadata_File (Tile Metadata); an XML main metadata file (DIMAP mandatory file) containing the requested level of information and referring to all the product elements describing the tile; an IMG_DATA folder containing image data files compressed using the JPEG2000 algorithm, one file per band; a QI_DATA folder containing QLQC XML reports of quality checks, mask files and PVI files; an Inventory_Metadata.xml: inventory metadata file (mandatory); a manifest.safe: XML SAFE manifest file (mandatory); and a rep-info: folder containing the XSD schema provided inside a SAFE Level-0 granule (ESA, 2015).

2.2 Methods

2.2.1 Sentinel-2 MSI Data Pre-processing

MSIL1C are already provided in the Top of Atmosphere (TOA) Reflectance, scaled prior to output, which can be converted to TOA reflectance by a simple calculation using the quantification value provided in the metadata (ESA, 2015).

The conversion formula to apply to image digital numbers (DNs) to obtain physical values is (ESA, 2015):

$$\text{Reflectance (float)} = \text{DC} / (\text{QUANTIFICATION\_VALUE}) \quad (2\text{-}1)$$

Furthermore, atmospheric correction was made by the DOS (Dark Object Subtraction) method (Chavez, 1988; Chavez, 1989).

2.2.2 Water Index Extraction

Several water indices were extracted from the calibrated data resulting from the pre-processing. Taking into account the spectral characteristics of the Sentinel-2 MSI channels, the water indices were extracted using following equations:

$$NDWI_{Gao} = \frac{\rho 0.842 - \rho 1.610}{\rho 0.842 + \rho 1.610} \quad (2\text{-}2)$$

$$NDWI_{McFeeters} = \frac{\rho 0.560 - \rho 0.842}{\rho 0.560 + \rho 0.842} \quad (2\text{-}3)$$

$$NDWI_{Roger\&\ Kearney} = \frac{\rho 0.665 - \rho 2.190}{\rho 0.665 + \rho 2.190} \quad (2\text{-}4)$$

$$MNDWI_{Xu} = \frac{\rho 0.560 - \rho 2.190}{\rho 0.560 + \rho 2.190} \quad (2\text{-}5)$$

http://dx.doi.org/10.30536/j.ijreses.2020.v17.a3286

3 RESULTS AND DISCUSSION

Figure 3-1 shows the water index extracted from Sentinel-2 MSI in Cirata dam. In the figure, the water surface area can be detected from several water indices. Compared with the colour composite image in natural colours, RGB 11-8-4 (Figure 3-2), and taking into account the results using and comparing various water-based indices, it can generally be seen that, among the NDWI models, but Gao's, are appropriate for detecting surface water areas. However, when examined in more detail, it can be seen that the NDWI of McFeeters (1996) shows the best results in detecting the surface water area.

Previous studies have attempted to use such imagery data for the identification and mapping of water surface areas and have obtained different results. Kwang et al. (2018) attempted to compare Landsat 8 and Sentinel 2A using water extraction indexes along the Volta River. Their results show that the modified normalized water difference index ($MNDWI_{Xu}$) proved to be the universal water body enhancement index because of its performance with both the Landsat 8 and Sentinel 2A images.

The modified normalized water difference index can therefore be recommended for use with either Landsat 8 or Sentinel 2A over other water indexes such as the normalized water difference index and the automatic water extraction index. Du et al. (2006) also attempted using Sentinel-2 imagery for mapping with the modified normalized difference water index, and their results show that $MNDWI_{Xu}$ can enhance water bodies and suppress built-up features more efficiently than NDWI. However, research conducted by Sekertekin et al. (2018) on identifying surface water resources in Çatalan and Yedigöze dam reservoirs in Turkey using Sentinel-2 found that $NDWI_{McFeeters}$ produced slightly more accurate results than $MNDWI_{Xu}$.

In another study, Yang et al. (2017) performed mapping of urban surface water bodies using Sentinel-2 MSI in Beijing, which is located inland, and Yantai, which is located in a coastal area. Their results show that the NDWI-based $MNDWI_{Xu}$ images exhibit higher separability and are more effective for both classification-level and boundary-level final water maps than traditional approaches.

Research conducted in Indonesia by Yulianto et al. (2018), who attempted to observe inundated areas using Landsat-8 multitemporal images in Bandung basin, found that MNDWI was the most appropriate parameter to use to detect flooded areas in the Bandung basin which had heterogeneous land surface conditions. In other studies, by using Landsat-7 ETM+ image data, the extent of inundated areas caused by floods in lowland regions could be identified and separated based on NDWI, MNDWI, and NWI. However, the NDWI method of McFeeters (1996) provided more appropriate results when compared to the other three methods (Suwarsono et al., 2013). These different results are most likely due to the influence of water environment characteristic on which model produces the more accurate results.

However, in principle, the NDWI of McFeeters utilises reflected near-infrared radiation and visible green light to enhance the presence of features, while eliminating the presence of soil and terrestrial vegetation. The NDWI of McFeeters may moreover provide analysts with turbidity estimations of water bodies utilising remote sensing data (McFeeters, 1996). The band selection of McFeeters's NDWI was chosen to maximise the typical

reflectance of water features by using the green light channel, to minimise the low reflectance of NIR by water objects, and to take advantage of the high reflectance of NIR by terrestrial vegetation and soil (McFeeters, 1996).

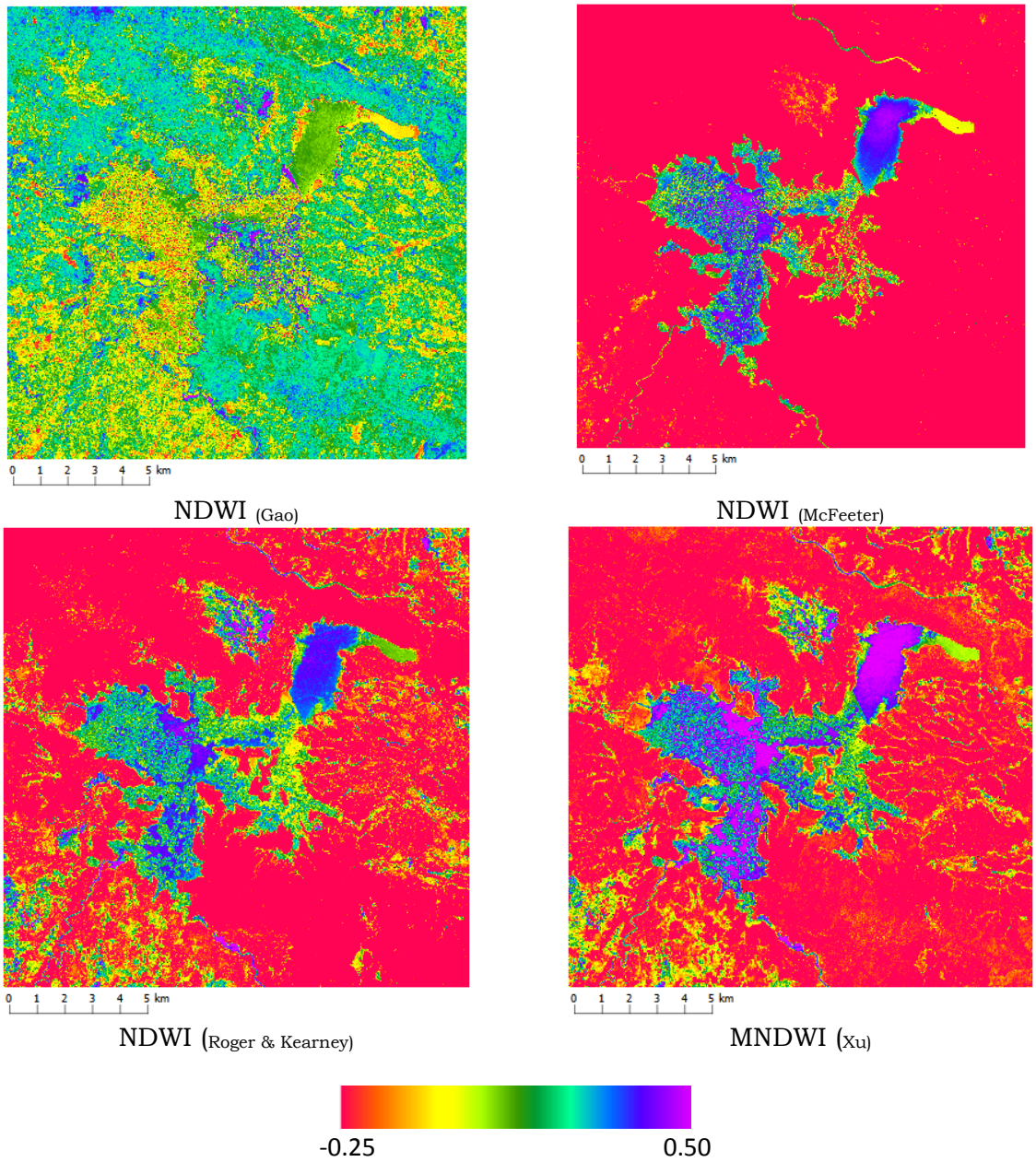

Figure 3-1: Water indices extracted from Sentinel-2 MSI.

4 CONCLUSION

The results conclude that the NDWI of McFeeters (1996) derived from Sentinel-2 MSI produces the best results in detecting the surface water area of the reservoir compared to other water indices. This model was conducted to maximize the typical reflectance of water features by using a green light channel, to minimize the low reflectance of NIR by water objects, and to take advantage of the high reflectance of NIR by terrestrial vegetation and soil. However, applications using Sentinel-2 MSI imagery for other regions that have different water environment conditions probably give different results. Therefore, further research is still

needed for different water environment conditions of other regions in Indonesia.

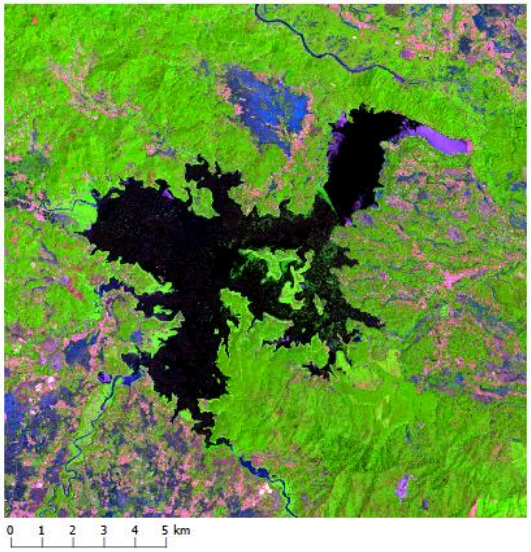

Figure 3-2: Sentinel-2 MSI natural colour composite (RGB 11-8-4).

ACKNOWLEDGEMENTS

This paper is a part of the research activities entitled 'The utilization of remote sensing data for disaster mitigation in Indonesia'. This research was funded by the Program of National Innovation System Research Incentive (INSINAS) in 2019, and the Ministry of Research Technology and Higher Education, Republic of Indonesia. Thanks to Dr Dony Kushardono, the group leader of this activity. SRTM30 DEM was provided by the U.S. Geological Survey (USGS), and Sentinel-2 was provided by European Space Agency (ESA) through the Copernicus Open Access Hub. We would like to thank Balai Besar Wilayah Sungai Citarum, Ministry of Public Work, for discussion, collaboration, field surveys, and sharing spatial data to support this research.

AUTHOR CONTRIBUTIONS

Detecting The Surface Water Area In Cirata Dam Upstream Citarum Using A Water Index From Sentinel-2. Lead Author: Suwarsono and Fajar Yulianto, Co-Author: Hana Listi Fitriana, Udhi Catur Nugroho, Kusumaning Ayu Dyah Sukowati, and Muhammad Rokhis Khomarudin.

REFERENCES

Acharya, T.D., Yang, I.T., Subedi, A. et al. (2016). Change detection of lakes in Pokhara, Nepal using Landsat data. *Proceedings 1*(17), doi:10.3390/ecsa-3-E005.

Ashraf, M., & Nawaz, R. (2015). A Comparison of Change Detection Analyses Using Different Band Algebras for Baraila Wetland with Nasa's Multi-Temporal Landsat Dataset. *Journal of Geographic Information System, 17*,1-19.

Chavez, Jr. P.S. (1988). An improved dark-object subtraction technique for atmospheric scattering correction of multispectral data. *Remote Sensing of Environment 24*, 459–79.

Chavez, Jr. P.S. (1989). Radiometric Calibration of Landsat Thematic Mapper Mutispectral Images. *Photogrammetric Engineering and Remote Sensing*, *55*(9),1285-1294.

Ding, F. (2009). A New Method for Fast Information Extraction of Water Bodies Using Remotely Sensed Data. *Remote Sensing Technology and Application, 24*(2), 167–171.

Drusch, M., Del Bello, U., Carlier, S. et al., (2012). Sentinel-2: ESA's Optical High-Resolution Mission for GMES Operational Services. *Remote Sensing of Environment* 120, 25-36.

Du, Z., Linghu, B., Ling, F. et al. (2012). Estimating surface water area changes using time-series Landsat data in the Qingjiang River Basin, China, *Journal of Applied Remote Sensing, 6*(1), 063609.

Du, Y., Zhang, Y., Ling, F. et al. (2016). Water Bodies' Mapping from Sentinel-2 Imagery with Modified Normalized Difference Water Index at 10-m Spatial Resolution Produced by Sharpening the SWIR Band. *Remote Sensing* 8(4),

354; https://doi.org/10.3390/rs8040354

ESA (2013). Sentinel 2, The Operational Copernicus Optical High Resolution Land Mission. Https://www.esa.int/copernicus.

ESA (2015). Sentinel-2 Products Specification Document. Ref : S2-PDGS-TAS-DI-PSD, Issue : 13.1, Date : 18/11/2015. Https://sentinel.esa.int/web/sentinel/user-guides/document-library.

Feng, D. (2009). A new method for fast information extraction of water bodies using remotely sensed data. *Remote Sensing Technology and Application, 24*(2), http:// www.oalib.com/paper/1468694#.XgQY7EczZ1s.

Gao, B.C. (1996). NDWI a normalized difference water index for remote sensing of vegetation liquid water from Space. *Remote Sensing of Environment, 58*, 257-266.

Kwang, C., Osei Jr, E.M., & Amoah, A.S. (2018). Comparing of Landsat 8 and Sentinel 2A using Water Extraction Indexes over Volta River. *Journal of Geography and Geology, 10*(1), doi:10.5539/jgg.v10n1p1.

Li, W., Du, Z., Ling, F. et al. (2013). A Comparison of Land Surface Water Mapping Using the Normalized Difference Water Index from TM, ETM+ and ALI. *Remote Sensing 5*(11), 5530–5549. doi:10.3390/rs5115530.

Li, P., Jiang, L., & Feng, (2014). Cross-Comparison of Vegetation Indices Derived from Landsat-7 Enhanced Thematic Mapper Plus (ETM+) and Landsat-8 Operational Land Imager (OLI) Sensors., *Remote Sensing, 6,* :310-329., DOI:10.3390/ rs6010310

McFeeters, S.K. (1996). The use of the Normalized Difference Water Index (NDWI) in the delineation of open water features. *International Journal of Remote Sensing 17*(7), 1425-1432. DOI: 10.1080/ 01431169608948714.

Rogers, A.S., & Kearney, M.S. (2004). Reducing Signature Variability in Unmixing Coastal Marsh Thematic Mapper Scenes Using Spectral Indices. *International Journal of Remote Sensing* 25(12), 2317–2335.

Sekertekin, A., Cicekli, S.Y., & Arslan, N. (2018). Index-Based Identification of Surface Water Resources Using Sentinel-2 Satellite Imagery. *2018 2nd International Symposium on Multidisciplinary Studies and Innovative Technologies (ISMSIT)*, Ankara, 2018, pp. 1-5, doi: 10.1109/ISMSIT.2018.8567062.

Suwarsono, Nugroho, J.T., & Wiweka. (2013). Identification of Inundated Area Using Normalized Difference Water Index (NDWI) on lowland region of Java Island. *International Journal of Remote Sensing and Earth Sciences, 10*(2), 114-121.

Szabó, S., Gácsi, Z., & Balász, B.B. (2016). Specific features of NDVI, NDWI and MNDWI as reflected in land cover categories. *Landscape & Environment, 10*(3-4), 194-202.

Wang, X., Liu, Y., Ling, F. et al. (2017). Spatio-Temporal Change Detection of Ningbo Coastline Using Landsat Time-Series Images during 1976–2015. *International Journal of Geo-Information, 6*(68), doi:10.3390 /ijgi6030068.

Xu, H. (2006). Modification of normalised difference water index (NDWI) to enhance open water features in remotely sensed imagery. *International Journal of Remote Sensing 27*(14), 3025–3033.

Yang J., & Du, X. (2017). An enhanced water index in extracting water bodies from Landsat TM imagery. *Annals of GIS, 23*(3), 141-148. DOI:10.1080/ 19475683.2017.1340339.

Yulianto, F., Suwarsono, Sulma, S. et al. (2018). Observing the inundated area using Landsat-8 multitemporal images and determination of flood-prone area in Bandung basin. *International Journal of Remote Sensing and Earth Sciences, 15*(2), 131-14

ANALYSIS OF POTENTIAL FISHING ZONES IN COASTAL WATERS: A CASE STUDY OF NIAS ISLAND WATERS

Anang Dwi Purwanto[1]*, Teguh Prayogo, Sartono Marpaung, and Argo Galih Suhada
[1]Remote Sensing Applications Center,
National Institute of Aeronautics and Space
*e-mail: anang.dwi@lapan.go.id

Received: 29 January 2020; Revised: 26 May 2020; Approved: 17 June 2020

Abstract. The need for information on potential fishing zones based on remote sensing satellite data (ZPPI) in coastal waters is increasing. This study aims to create an information model of such zones in coastal waters (coastal ZPPI). The image data used include GHRSST, SNPP-VIIRS and MODIS-Aqua images acquired from September 1st-30th, 2018 and September 1st-30th, 2019, together with other supporting data. The coastal ZPPI information is based on the results of thermal front SST detection and overlaying this with chlorophyll-a. The method of determining the thermal front sea surface temperature (SST) used Single Image Edge Detection (SIED). The chlorophyll-a range used was in the mesotropic area (0.2-0.5 mg/m^3). Coastal ZPPI coordinates were determined using the polygon centre of mass, while the coastal ZPPI information generated was only for coastal areas with a radius of between 4-12 nautical miles and was divided into two criteria, namely High Potential (HP) and Low Potential (LP). The results show that the coastal ZPPI models were suitable to determine fishing locations around Nias Island. The percentage of coastal ZPPI information generated was around 90% information monthly. In September 2018, 27 days of information were produced, consisting of 11 HP sets of coastal ZPPI information and 16 sets of LP information, while in September 2019 it was possible to produce 29 days of such information, comprising 11 sets of HP coastal ZPPI information and 18 LP sets. The use of SST parameters of GHRSST images and the addition of chlorophyll-a parameters to MODIS-Aqua images are very effective and efficient ways of supporting the provision of coastal ZPPI information in the waters of Nias Island and its surroundings.

Keywords: *Potential Fishing Zones, Coastal ZPPI, GHRSST, Single Image Edge Detection (SIED), Nias Island*

1 INTRODUCTION

Indonesia is a country that has a larger water area than land area. The International Convention of the Law of the Sea 1982 states that the total area of Indonesian waters is 5.9 million km^2 consisting of 3.2 million km^2 of territorial waters and 2.7 million km^2 of Exclusive Economic Zone (EEZ) waters (Lasabuda, 2013). The total area of these waters shows that 2/3 of Indonesian territory is water, with the remainder being land. The waters of Indonesia have a very high potential for fish resources. Based on data from the annual report of the Ministry of Maritime Affairs and Fisheries (KKP) of 2017, Indonesian fisheries production amounted to 6.99 million tons in 2017. In order to support the increase in the level of fishing, the National Institute of Aeronautics and Space (LAPAN) remains committed to provide fishing area information based on remote sensing satellite imagery data, known as potential fishing zones (ZPPI) (Hasyim, 2015). The ZPPI information produced by LAPAN is currently used by most fishermen in Indonesia.

http://dx.doi.org/10.30536/j.ijreses.2020.v17.a3298

Distribution of the ZPPI information is made using an android application, a website and e-mail to both central and local government users, the private sector, state-owned enterprises and other stakeholders.

The current ZPPI information does not include waters under 12 nautical miles from the coastline due to various considerations, including the avoidance of the fishing activities of large vessels (loading capacity above 30 GT) fishing in coastal waters (under 12 nautical miles from the coastline) and to provide flexibility for small/traditional fishermen with small vessels (loading capacity below 30 GT) in fishing activities in coastal areas. In addition, if fishermen with small boats fish in the open sea (above 12 miles), this will greatly endanger their safety. Based on data of the Ministry of Maritime Affairs and Fisheries (2008), cited in Retnowati (2011), the number of Indonesian fishermen in in 2009 was 2,752,490, with a total number of boats of 596,230; 90% of the fishermen were small-scale. Therefore, it is necessary to develop ZPPI information related to waters within 12 nautical miles of the coastline which is specifically intended for small or traditional fishermen.

Along with the rapid development of science and technology, remote sensing technology can be optimised for the detection of oceanographic parameters, including the determination of potential fishing zones. Oceanographic conditions can be used as an indicator of the presence of fish, as a cold water mass rich in nutrients is suitable for the presence of fish (Balaguru, Ramakrishnan, Vidhya & Thanabalan, 2014). Purwanto et al. (2012) conducted a study of sea surface temperatures in the Western Java Sea using NOAA and MODIS satellite imagery. In addition, Marpaung et al. (2018) conducted research related to information on potential fishing zones based on SNPP-VIIRS and Himawari 8 imagery. Sea surface temperature and chlorophyll concentration can be measured to determine fishing ground prediction models using MODIS data (Suwargana et al., 2004). Hamzah et al. (2016) used the polygon mass centre method to determine the coordinates of potential fishing zones.

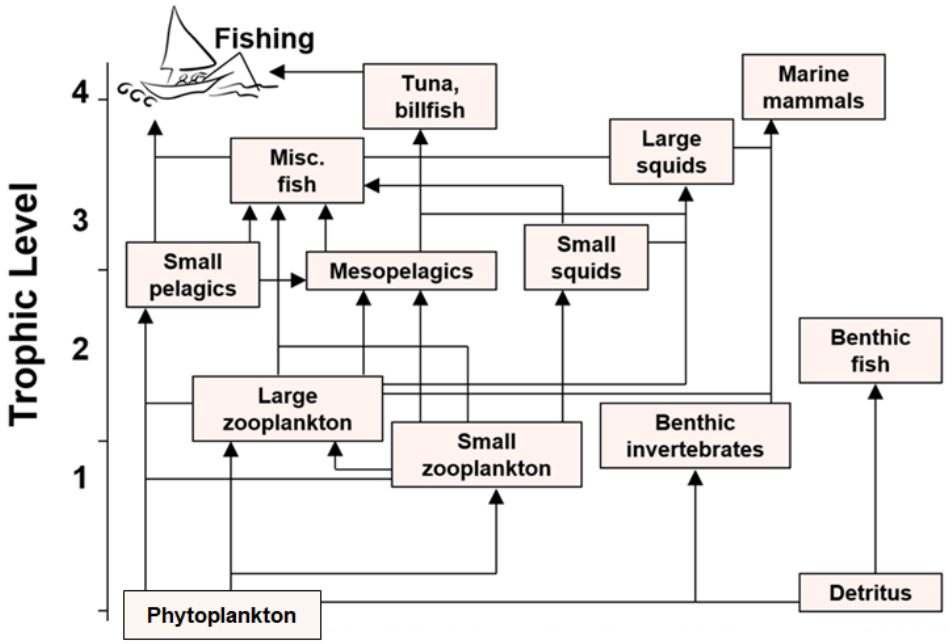

Figure 1-1: Food chain in the sea (Pauly & Christensen, 1993)

Figure 1-1 shows the food chain process in waters where the chlorophyll-a parameter plays an important role. Using satellite imagery, Zainuddin et al. (2006) found that there was a relationship between albacore tuna fish catches and the concentration of chlorophyll-a, with its value in the highest catchment area in the northwestern North Pacific being in the range of 0.2-0.4 mg/m^3. Another study conducted by Zainuddin (2011) showed the highest number of skipjack tuna catches in Bone Bay was in areas with chlorophyll concentrations of between 0.1-0.4 mg/m^3. In addition, the results of a study conducted by Nurdin et al. (2017) also showed that the highest concentration of rastrelliger kanagurta catches in Spermonde Islands waters was at a concentration of chlorophyll-a of between 0.2-05 mg/m^3.

The results of the evaluation of socialisation activities and focus group discussions with the local government, private sector and the fishing community show that the requirements for potential fishing zones in coastal areas is increasing, one of these being for fishermen in Nias Island waters. The large sea area and diverse types of fish with a sufficiently high market value indicate that the Nias region has great potential for marine fisheries (Zebua et al., 2014). Based on data from the North Nias Regency Fisheries Office, catches by fishermen in the area in the period 2000-2018 were dominated by tuna and cakalang. In addition, the fishing boats in the area were dominated by small vessels with a loading capacity of 0.5-1 GT, with fishing operations carried out over a relatively short period of time, commonly known as one day fishing activity. This type of fishing operation takes place within a range fairly close to the coast and is usually done on a daily basis; that is, leaving in the morning and returning in the afternoon, or leaving in the afternoon and returning in the morning.

The aim of this study is to create a model of potential fishing zones in the coastal waters of Nias Island (coastal ZPPI) based on remote sensing satellite imagery. It is hoped that the availability of such information will help and facilitate fishing activities, especially for traditional or small fishermen, and support the increase in the volume of fish catches, thus improving the welfare of fishermen in the area.

2 MATERIALS AND METHODOLOGY

2.1 Location and Data

This research was located in the western waters of Indonesia, specifically around Nias Island, with the coordinates 3 ^{0}N-0.9 ^{0}S and 95.8-99.2 ^{0}E. This area was chosen chosen to represent open sea waters directly facing the Indian Ocean, but also with closed waters on the eastern side. The research location is bordered by the Indian Ocean to the west, north and south, while to the east it is bordered by Sumatra Island. The waters have steep coastal depths. Figure 2-1 shows the location.

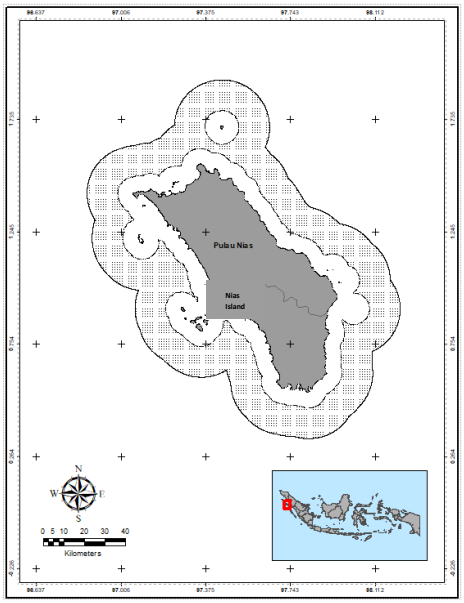

Figure 2-1: Map of the research area

The image data used were low resolution satellite imagery, including Visible/Infrared Imager Radiometer Suite (SNPP-VIIRS) Level 2 with a spatial resolution of 750 meters and Group for High Resolution Sea Surface Temperature (GHRSST) Level 4, with a spatial resolution of 1 kilometer, which was used to extract daily sea surface temperatures. SNPP-VIIRS images were obtained from the LAPAN Pustekdata catalog website (modis-catalog.lapan.go.id), while the GHRSST image data were obtained from the NASA website (http://podaac.jpl.nasa.gov/). Paena et al. (2015) explain that GHRSST images are the result of interpolation from several data sensors, namely microwave (Advanced Microwave Scanning Radiometer-AMSR and Tropical Rainfall Measuring Mission Microwave Imager-TMI) and infrared (Moderate Resolution Imaging Spectroradiometer-MODIS). The use of the GHRSST images is expected to be able to cover the lack of current potential fishing zone information, which has been one of the obstacles to the operationalisation of ZPPI in LAPAN. Other image data used were MODIS Aqua imagery Level 2, with a spatial resolution of 1 kilometer, used to extract daily and eight daily chlorophyll-a, which was obtained from NASA's Ocean Color website (https://oceancolor.gsfc.nasa.gov).

The three types of image data used were acquired in September 2018 and September 2019. The time of image selection was adjusted to the time of field data retrieval, which was conducted twice, namely in September 2018 and September 2019. Two types of field measurement data were employed: oceanographic measurement data and interviews with coastal fishermen in North Nias and Gunungsitoli about fishing operations (fishing locations, fish catches, fishing time, number of personnel, fishing gear, etc). Other supporting data used were Nias Island administrative boundaries, Gebco water depth data, grid vector data size of 1 nautical mile, and buffer area data of 4 and 12 nautical miles.

2.2 Methods

Sea surface temperature and chlorophyll-a data were used as the main parameters in the determination of coastal ZPPI information. These were downloaded in netcdf (.nc) format, so it was necessary to convert them into geotiff format using Seadas 7.5.1 software to make further processing easier using other image processing software. Generally, the stages of determining coastal ZPPI information include determining the thermal front of sea surface temperature using the Single Image Edge Detection (SIED) method; determining the value of chlorophyll-a in the mesotropic area (0.2-0.5 mg/m^3); an overlay process between the thermal front and chlorophyll-a (mesotropic area); grouping the overlay results into grid sizes of 1 nautical mile; and determining coastal ZPPI coordinates using the polygon mass centre method.

The thermal front parameters were obtained from daily SST data from GHRSST and SNPP-VIIRS satellite imagery. Thermal front detection was conducted in several stages, including selection of SST channels (specifically SNPP-VIIRS); geometric and atmospheric corrections; data selection based on recording time; cropping image data based on area of interest (AOI); and thermal front detection using the SIED algorithm (Cayula & Cornillon, 1992). Jatisworo and Murdianto (2013), Hamzah et al. (2014) and Hanintyo et al. (2015) have also employed the SIED algorithm in Indonesian waters using a threshold parameter of 0.5 ^0C.

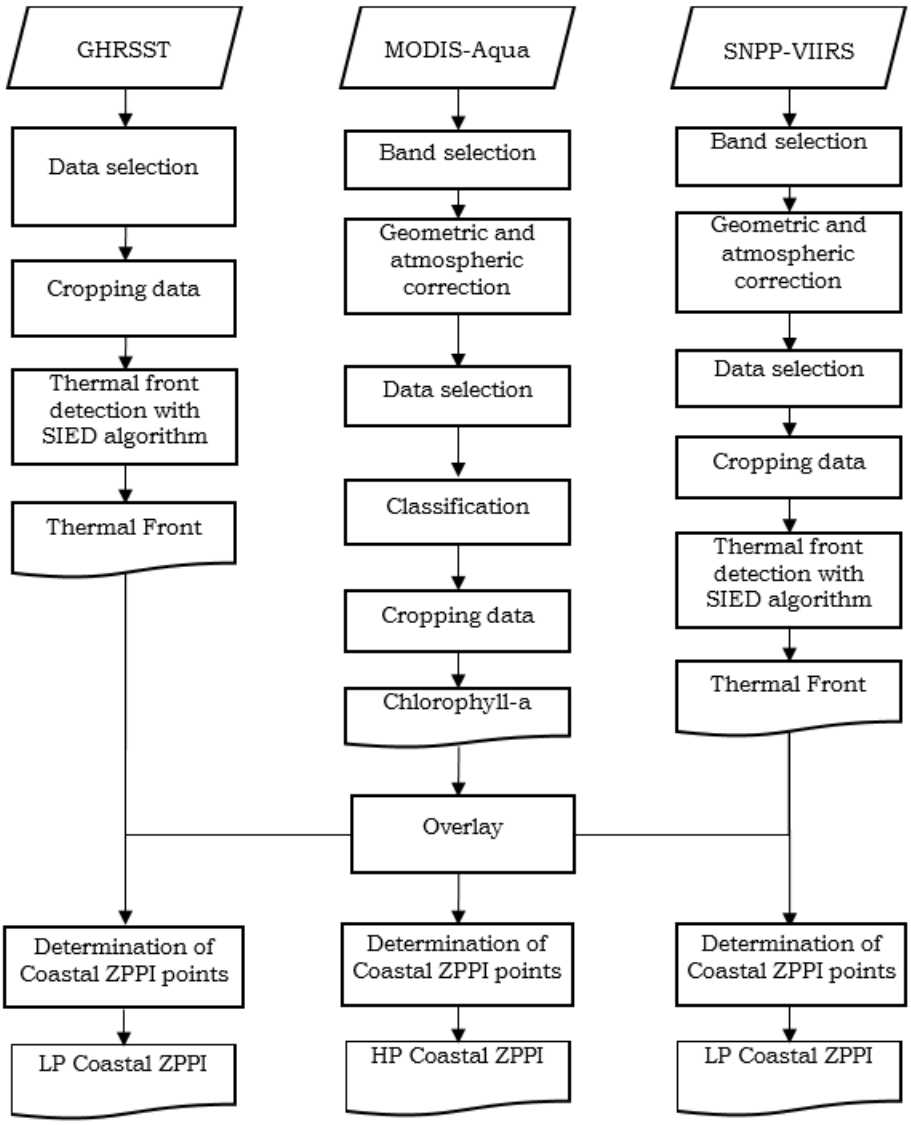

Figure 2-2: Detection Flow Chart of Thermal Front and Chlorophyll-a

Chlorophyll-a information was obtained from MODIS Aqua images, with stages including chlorophyll-a channel selection, geometric and atmospheric corrections, data selection based on recording time and concentrations in the range of 0.2-0.5 mg/m^3, and cropping image data based on AOI. A range of chlorophyll values of 0.2-0.5 mg/m^3 was used, in line with Nurdin et al. (2017), who explain that pelagic fishing is dominated by chlorophyll concentration. Reclassification was performed to separate chlorophyll-a from the existing day unit, with a class length of 0.05 mg/m^3. The flow diagram of this study is shown in Figure 2-2, relating to the detection of thermal front parameters and chlorophyll-a, while Figure 2-3 shows the stages of determining coastal ZPPI points.Determination of the coordinates of coastal ZPPI starts with the conversion of raster data to polygons, removal of small polygons, polygon smoothing, determination of areas containing a fishnet grid size of 1 nautical miles, determination of the midpoint of each polygon, and extraction of the midpoint coordinate values of each polygon.

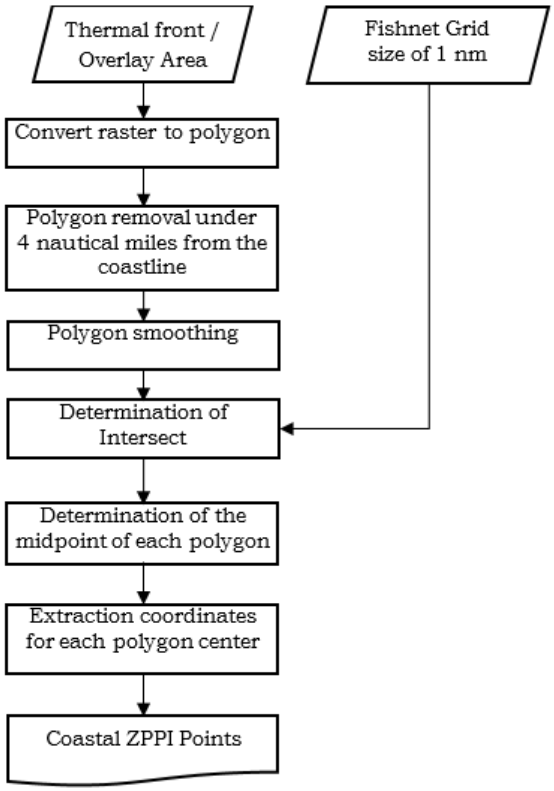

Figure 2-3: Determination Flow Chart of Coastal ZPPI Point

The resulting coastal ZPPI information is divided into two criteria, high potential (HP) and low potential (LP), as shown in Table 2-1. A coastal ZPPI with HP criteria is obtained from the overlay between sea surface temperature parameters and chlorophyll-a, while coastal ZPPI with LP criteria are obtained from only one of the parameters of sea surface temperature or chlorophyll-a. HP coastal ZPPI information has tended to be of higher potential than that in the LP category because it is strengthened by the presence of two main parameters, namely the thermal front and chlorophyll-a. Angraeni et al. (2014) explain that there is a tendency for a relationship between thermal fronts and large pelagic fish catches. A thermal front is defined as a meeting area of two water masses that have different temperature characteristics (Hanintyo et al., 2015) and can be used as an indicator of potential fishing areas (Simbolon et al., 2013). In addition, Simbolon et al. (2009) also explain that the chlorophyll-a parameter plays a role as a primary producer in marine ecosystems and can also be used in estimating fishing grounds.

Table 2-1: Coastal ZPPI Criteria

Parameter		**Coastal ZPPI Criteria**
Thermal Front	**Chlorophyll -a**	
✓	✓	High Potential (HP)
✓		Low Potential (LP)
	✓	Low Potential (LP)

To establish the quality of the resulting spatial model, it is necessary to compare it with the actual conditions in the field related to fishing areas, especially in the coastal waters of Nias Island. In this study, a qualitative suitability test was conducted. The resulting coastal ZPPI model was

matched with data on fishing locations around the island. Fishing location data were obtained from interviews with several fishermen in North Nias District and Gunung Sitoli City.

3 RESULTS AND DISCUSSION

3.1 Extraction of Sea Surface Temperature and Chlorophyll-a

The main imagery data used for the extraction of sea surface temperature information were GHRSST images, while extraction of chlorophyll-a information was from MODIS Aqua imagery. Sea surface temperature information from the SNPP VIIRS imagery was used to provide data which was lacking and complete the SST thermal front information from the GHRSST satellite imagery. The use of such imagery is very effective in supporting the provision of sea surface temperature information in the waters around Nias Island. Almost all of SST information is produced completely in September 2018 and September 2019. In September 2018, the thermal front information generated included 21 days from the GHRSST images and 4 days from the SNPP-VIIRS images, while the chlorophyll-a (mesotropic area) information produced covered 15 days. In September 2019, thermal front information was generated for 29 days from the GHRSST imagery and 6 days from the SNPP-VIIRS imagery, while the chlorophyll-a (mesotropic area) information produced covered 11 days. Figures 3-1 and 3-2 show an example of the results of the extraction of SST information from GHRSST images and chlorophyll-a information from MODIS-Aqua images for daily periods in waters around Nias Island.

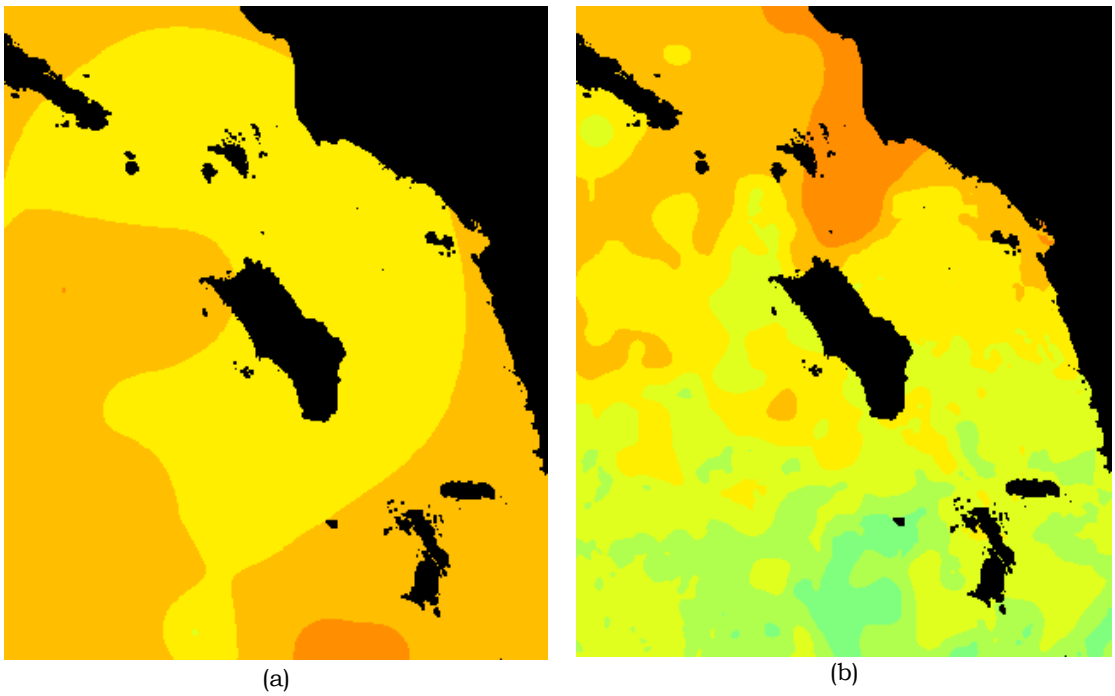

(a) (b)

Figure 3-1: SST Extraction Results of GHRSST Images (a) September 22th, 2018, and (b) September 22th, 2019

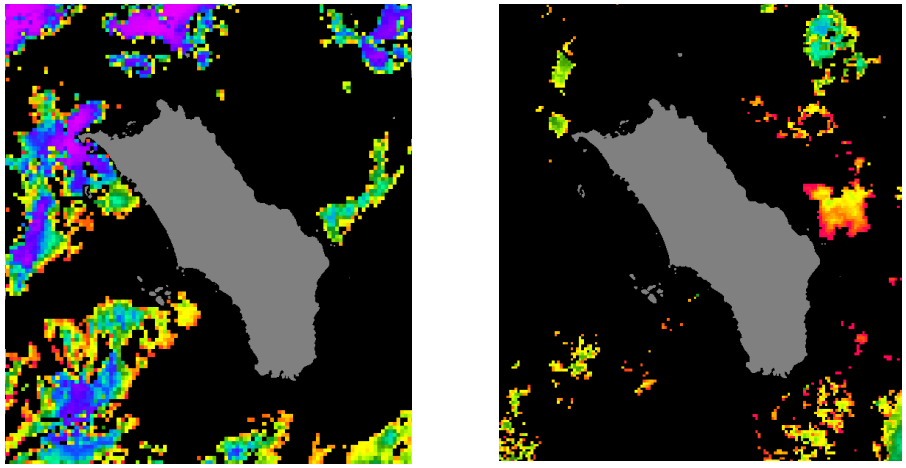

(a) (b)

Figure 3-2: Chlorophyll-a Extraction Results (a) September 22th, 2018, and (b) September 18th, 2019

3.2. Determination Results of Coastal ZPPI

Overlay analysis was performed on polygons that intersect the thermal front and chlorophyll-a parameters. This intersection area is assumed to have a better correlation with the presence of pelagic fish because each parameter can be used as an indication of habitat from the presence of a shoal of fish. Examples of the intersect results of several parameters used to produce coastal ZPPI information are shown in Figure 3-3.

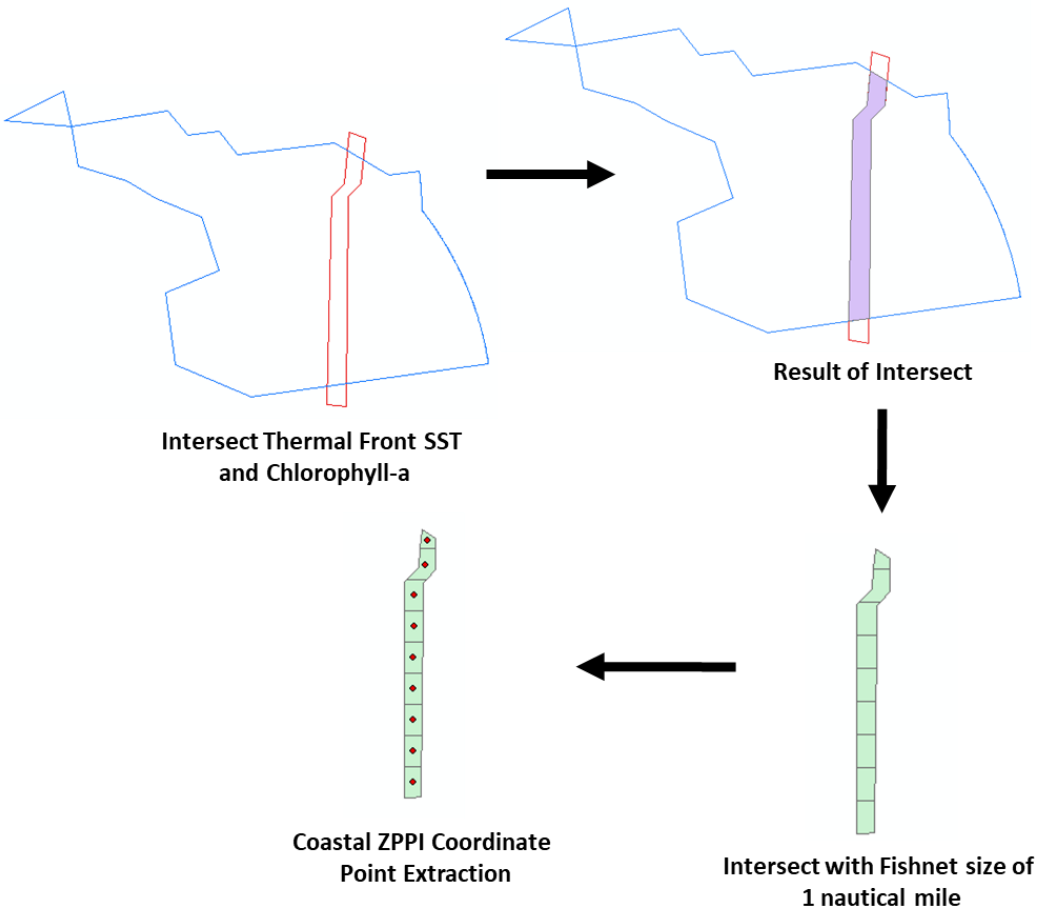

Figure 3-3: Intersection Results of several coastal ZPPI parameters

Table 3-1: Recapitulation of the results of coastal ZPPI determination

Date	Sept 2018			Coastal ZPPI	Sept 2019			Coastal ZPPI
	Front-GHRSST	Front-VIIRS	Chl-a		Front - GHRSST	Front-VIIRS	Chl-a	
1	✓		✓	HP	✓			LP
2	✓		✓	HP	✓			LP
3	✓		✓	HP	✓			LP
4	✓		✓	HP	✓			LP
5	✓		✓	HP	✓			LP
6	✓		✓	HP	✓	✓		LP
7	✓		✓	HP	✓			LP
8	✓		✓	HP	✓			LP
9	✓			LP	✓		✓	HP
10		✓		LP	✓		✓	HP
11					✓	✓	✓	HP
12			✓	LP	✓	✓		LP
13			✓	LP	✓		✓	HP
14					✓			LP
15	✓		✓	HP	✓			LP
16	✓			LP	✓			LP
17	✓			LP	✓	✓	✓	HP
18					✓		✓	HP
19			✓	LP	✓			LP
20			✓	LP	✓		✓	HP
21		✓		LP	✓		✓	HP
22	✓		✓	HP	✓	✓	✓	HP
23	✓			LP	✓	✓	✓	HP
24	✓			LP	✓		✓	HP
25	✓	✓		LP	✓			LP
26	✓	✓		LP	✓			LP
27	✓		✓	HP	✓			LP
28	✓			LP	✓			LP
29	✓			LP				
30	✓			LP	✓			LP

The use of satellite imagery to extract the two main parameters of coastal ZPPI, namely sea surface temperature and chlorophyll-a is able to increase the number coastal ZPPI information. From the overall data used, 27 days of ZPPI coastal information was generated in September 2018, and 29 days in September 2019. A recapitulation of the results of the determination can be seen in Table 3-1.

The results of the coastal ZPPI recapitulation in Table 3-1 show that within a period of one month the percentage of related information generated was around 90%. In September 2018, coastal ZPPI information was generated over 27 days, consisting of 11 sets of information with high potential (HP) criteria and 16 with Low Potential (LP) criteria, whereas in September 2019 coastal ZPPI information was generated for 29 days, with 11 sets of HP criteria and 18 of LP criteria. From the calculation details, it can be seen that the developed model is able to support the provision of coastal ZPPI information to small-scale fishermen, especially in the waters around Nias Island. Figure 3-4 shows a comparison between HP and LP coastal ZPPI information.

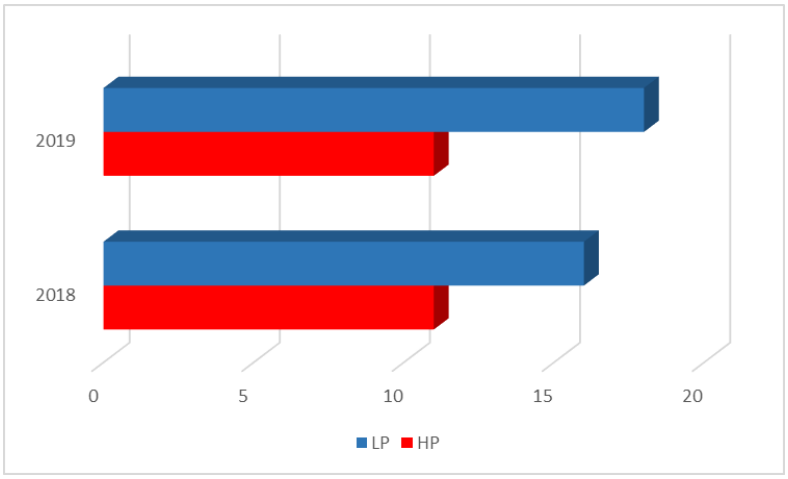

Figure 3-4: Comparison of Coastal ZPPI information based on High Potential (HP) and Low Potential (LP) criteria

Information on potential fishing zones in coastal areas (coastal ZPPI) is needed by small-scale fishermen who have small vessels with a loading capacity of under 5 GT. Such information is produced by two methods, namely the overlay of thermal front SST and chlorophyll-a parameters, as well as the results of determining thermal front SST. HP coastal ZPPI indicates there is a high potential for fish shoals because they are supported by a suitable environment and high nutrient conditions. LP coastal ZPPI indicates there is low potential for fish shoals because they are only supported by appropriate environmental factors, but not by the level of water nutrients.

Coastal ZPPI information was only generated for coastal areas with a radius of between 4-12 nautical miles. The lowest limit of 4 nautical miles was obtained based on the interviews with fishermen on Nias Island on 24-20 September 2019, while the highest limit of 12 nautical miles was based on the lowest limit of the exclusive economic zone of Indonesian waters. The results of determining coastal ZPPI information for Nias Island waters are shown in Figure 3-5.

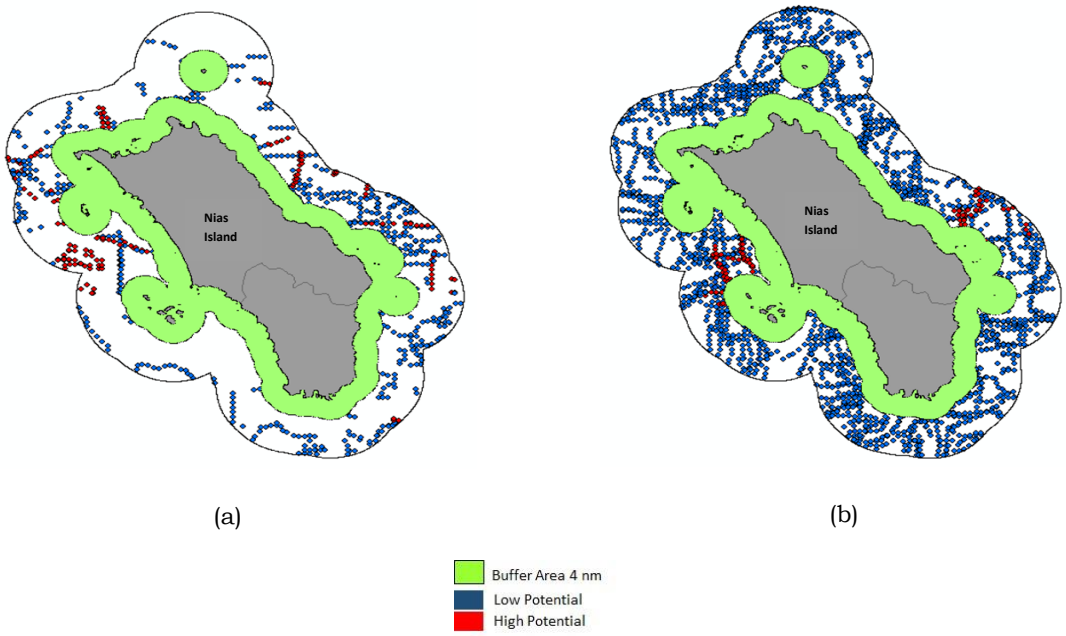

Figure 3-5: Coastal ZPPI Information for Nias Island Waters: (a) September 2018, (b) September 2019

The distribution of coastal ZPPI information in 2019, both HP and LP, was higher than that of 2018. The recapitulation data in Table 3-1 show that in September 2018 there was an information vacuum fof 3 days, namely on the 11th, 14th and 18th. This was due to several factors, including the lack of thermal front events on these dates from both GHRSST and SNPP VIIRS images, the value of chlorophyll-a concentrations being outside the limits of the mesotrophic area, as well as the fact that there was cloud cover around the research location. In September 2019, there was only one day of information vacuum, on the 29th. Even though the chlorophyll-a information was lower than in September 2018, the SST information from the GHRSST images was higher, meaning that the coastal ZPPI information generated in September 2019 was higher than in September 2018.

HP coastal ZPPI distribution was found in the west and east of the study site. The distribution of HP coastal ZPPI on the western part of Nias Island was adjacent to the location of the reef (or locally 'gosong') which is often used as a fishing ground. Based on information from the local fishermen, coral reefs are located at a depth of around 15-20 meters. Purwanto et al. (2020) mapped the distribution of 'gosong karang' around the waters of North Nias using Sentinel 2A images, with the location of the reef distribution is in accordance with the fishing locations of fishermen in North Nias Regency (Winardi et al., 2007, cited in Telaumbana, 2009). Distribution of the HP coastal ZPPI in the eastern part of Nias Island was in the water depth transition area, as shown in Figure 3-6. This area indicates the mixing of water masses, so it can be assumed that underwater masses rise to the surface carrying a high level of nutrients that will be used as food by the fish. This natural event is often known as the upwelling process.

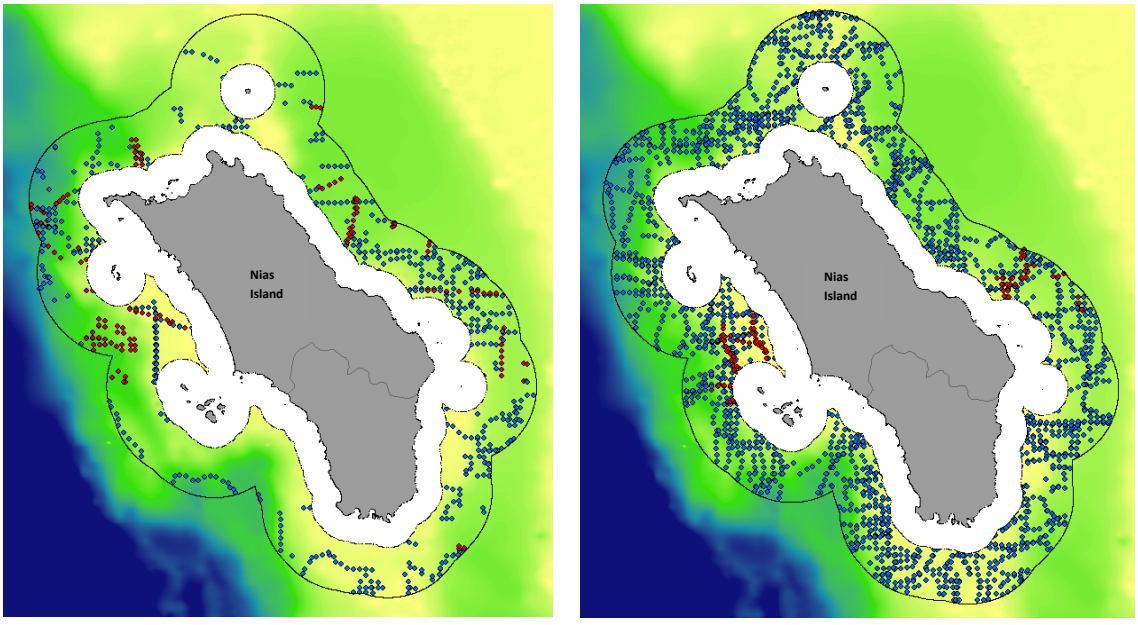

(a) (b)

Figure 3-6: Overlay of Water Depth Map and Coastal ZPPI Information: (a) September 2018, (b) September 2019 (Source: Gebco Data 2014)

3.3 Effectiveness of the Use of GHRSST Imagery for Determining Coastal ZPPI

One obstacle to producing current ZPPI information (using SNPP-VIIRS imagery) is cloud cover, which is very high on certain days, so ZPPI information cannot be generated. GHRSST imagery can be optimised to solve some the weaknesses of the use of certain previous satellite imagery. Figure 3-7 shows the suitability of coastal ZPPI information from thermal front GHRSST images and SNPP VIIRS images on September 25th and September 26th, 2018. The figure shows the suitability of the two locations circled to the east and west of the sland, with the two images used (GHRSST and SNPP-VIIRS) producing the coastal ZPPI information at that location.

A suitability test was also peformed on the results of the determination of coastal ZPPI based on thermal fronts from the GHRSST and SNPP VIIRS images on adjacent dates, i.e. September 6th, 11th, 17th and 22th, 2019, as shown in Figure 3-8. On September 6th and 11th, suitable coastal ZPPI points from the GHRSST and SNPP VIIRS images were found in the western and southern parts of the study site, while suitable coastal ZPPI distribution on September 17th and 22th from both images was also found in the northern and eastern parts of the study location.

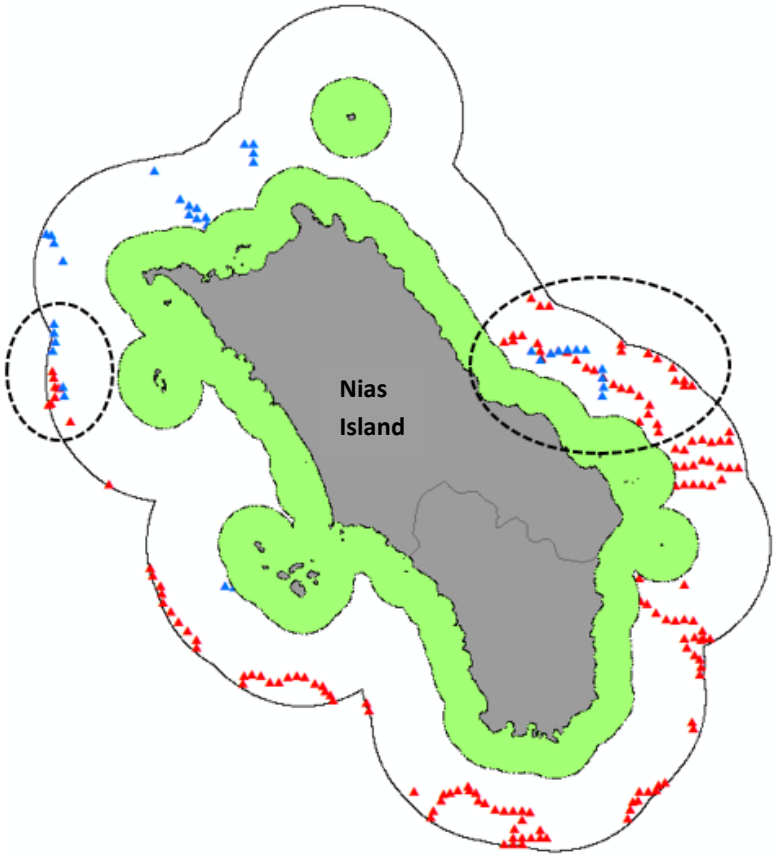

Figure 3-7: Suitability of Coastal ZPPI information from GHRSST (blue) and SNPP VIIRS (red) on September 25th and 26th, 2018

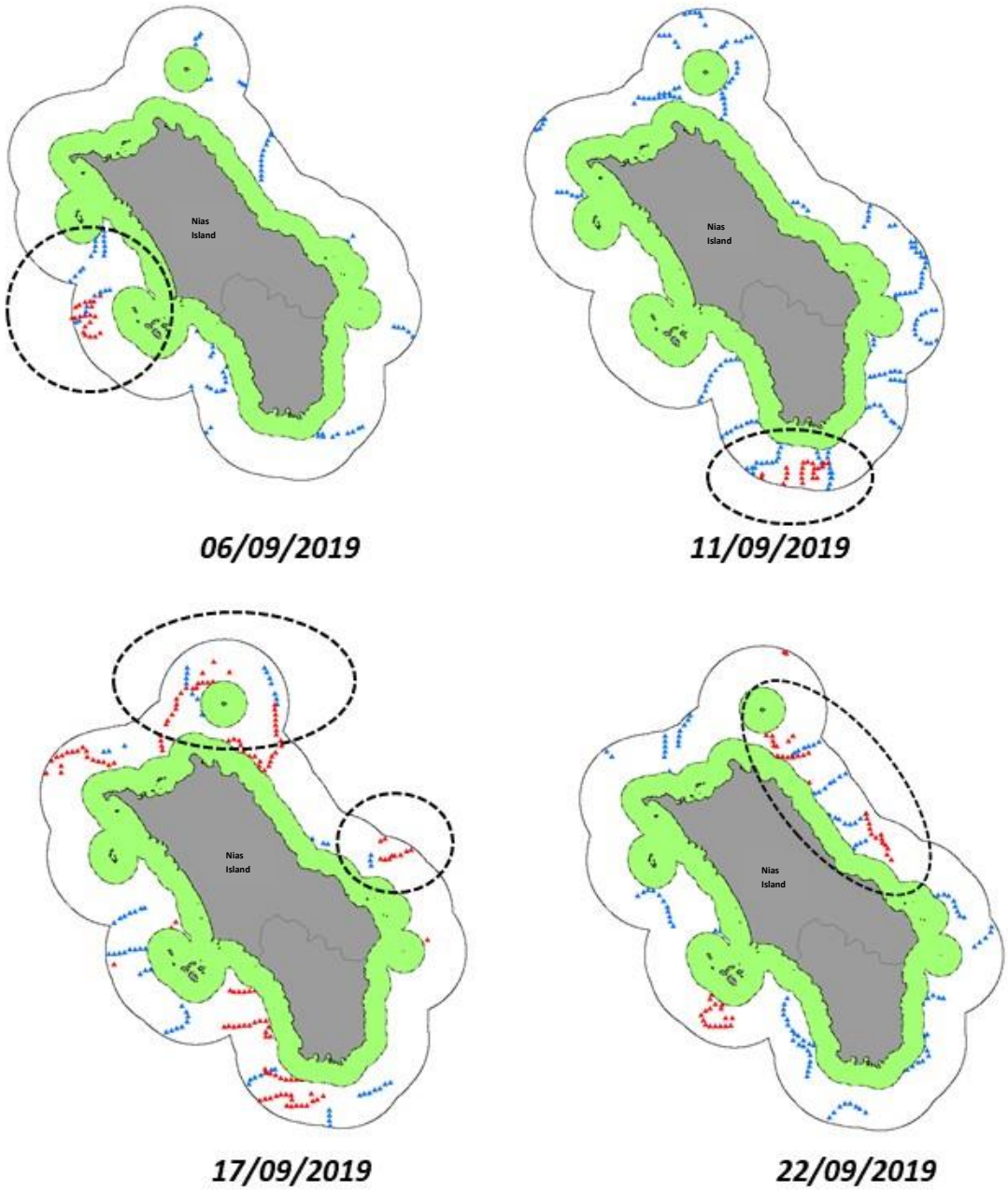

Figure 3-8: Suitability of Coastal ZPPI information from GHRSST (blue) and SNPP-VIIRS (red) on September 6th and 11th, and 17th and 22th, 2019

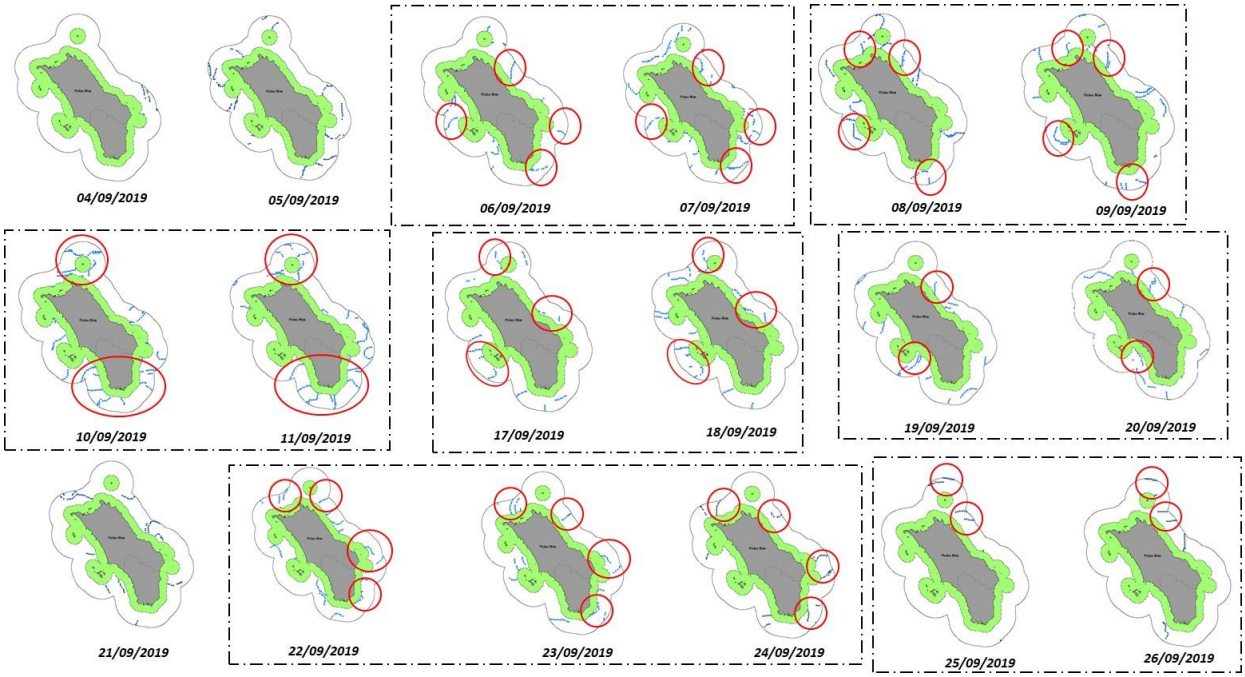

Figure 3-9: Coastal ZPPI Distribution Pattern based on Thermal Fronts from GHRSST Images on September 6th-22th and 17th-22th, 2019

Figure 3-9 shows the distribution pattern of the coastal ZPPI in September 2019 based on thermal front GHRSST images. In general, the thermal front has almost the same pattern over a two day period, while a difference in thermal front patterns over a 2-3 day period is seen in some parts of Nias Island. Thermal fronts occur in the western and southern parts of the island because the oceanographic conditions in these waters are more dynamic than in other parts, while the fronts that occur in the eastern and northern parts of the island tend to be in water depth transition areas.

4 CONCLUSION

The use of SST parameters from GHRSST images and the addition of chlorophyll-a parameters from MODIS Aqua images are very effective and efficient in supporting the provision of coastal ZPPI information in the waters of Nias Island and its surroundings. The use of GHRSST image data is able to complete the lack of daily ZPPI information due to weaknesses in the SNPP-VIIRS imagery. The results of determining the information on coastal ZPPI in Nias Island waters can be divided into two categories, namely high potential (HP) and low potential (LP) coastal ZPPI.

The resulting coastal ZPPI model is suitable for fishing locations around Nias Island. About 90 percent of ZPPI Coastal information is generated monthly. In September 2018, 27 days of coastal ZPPI information were produced, consisting of 11 sets of HP information and 16 of LP information, while in September 2019 there were 29 coastal ZPPI information days, consisting of 11 HP sets of information and 18 LP sets. The limit of the coastal ZPPI information was at a distance of 4-12 nautial miles from the coastline. The model that have been developed should also be tested in other water locations in Indonesia because the character of marine waters, especially in coastal areas, differs greatly.

ACKNOWLEDGEMENTS

We are grateful to the Remote Sensing Application Center of LAPAN for providing facilities during the implementation of the research; to the Remote Sensing Technology and Data

Center of LAPAN for providing access to SNPP-VIIRS satellite data; to NASA for providing access to GHRSST and MODIS satellite data; and to the Head of North Nias Regency Fisheries Office, who helped in the field survey activities. Special thanks also go to Mr Widodo S. Pranowo and Mrs Ety Parwati for providing many suggestions for the research and also to those who helped in its completion.

AUTHOR CONTRIBUTIONS

Analysis of Potential Fishing Zones In Coastal Waters: A Case Study Of Nias Island Waters. Lead Author: Anang Dwi Purwanto, Co-Author: Teguh Prayogo, Sartono Marpaung, and Argo Galih Suhada.

REFERENCES

Angraeni, Rezkyanti, N.I., Safruddin, & Zainuddin, M. (2014). Spatial and Temporal Analysis of Skipjack Tuna (Katsuwonus pelamis) Catch and Thermal Front during the Transition Season in the Bone Bay. *Jurnal IPTEKS PSP, 1*(1), 20 – 27.

Balaguru, B., Ramakrishnan, S.S., Vidhya, R., & Thanabalan, P. (2014). A Comparative Study on Utilization Of Multi-Sensor Satellite Data To Detect Potential Fishing Zone (PFZ). *The International Archives of the Photogrammetry, Remote Sensing and Spatial Information Sciences, XL-8*, 2014. ISPRS Technical Commission VIII Symposium, 09 - 12 December 2014, Hyderabad, India.

Departemen Kelautan dan Perikanan. (2008). Implementation Guidelines for Fisheries Port Management, Jakarta.

Hamzah, R., Prayogo, T., & Marpaung, S. (2016). Method Of Determination Points Coordinate for Potential Fishing Zone Based on Detection of Thermal Front Sea Surface Temperature. *Jurnal Penginderaan Jauh, 13*(2), 97–108.

Hasyim, B. (2015). Indonesian Institute of Aviation and Space Develop the Potential Fishing Zones. https://berita2bahasa.com/berita/1/15591610-lapan-kembangkan-zppi-bantu-nelayan-identifikasi-zona-ikan. Accessed 20 Jan 2020.

Hanintyo, R., Hadianti, S., Mahardhika, R.M.P., Aldino, & Islamy, F. (2015). Seasonal Distribution of Thermal Front Events Based on Aqua-MODIS Imagery in WPP-RI 714, 715, WPP-RI 716. Prosiding Seminar Nasional Penginderaan Jauh Nasional 2015.

Lasabuda, R. (2013). Regional Development in Coastal and Ocean in Archipelago Perspective of The Republic of Indonesia. *Jurnal Ilmiah Platax, I*-2, 92-101.

Marpaung, S., Prayogo, T., Parwati, E., Setiawan, K.T & Roswintiarti, O. (2018). Study On Potential Fishing Zones (PFZ) Information Based On S-Npp Viirs and Himawari-8 Satellites Data. *International Journal of Remote Sensing and EarthSciences, 15*(1), 51–62.

Nurdin, S., Mustapha, M., Lihan, T., & Zainuddin, M. (2017). Applicability of remote sensing oceanographic data in the detection of potential fishing grounds of Rastrelliger kanagurta in the archipelagic waters of Spermonde, Indonesia. *Fisheries Research, 196,* 1-12.

Paena, M., Suhaimi, R.A., & Undu, M.C. (2015). Analysis of Dissolved Oxygen Concentration (DO), pH, Salinity and Temperature in the rainy season on the decline in water quality in the Punduh Waters Pesawaran Regency Lampung Province. Seminar Nasional Kelautan X, Sinergitas Teknologi dan Sumber Daya Kelautan untuk Mewujudkan Indonesia sebagai Poros Maritim Dunia. Fakultas Teknik dan Ilmu Kelautan Universitas Hang Tuah, Surabaya 21 Mei 2015.

Pauly, D., & Christensen, V. (1993). Stratified Models of Large Marine Ecosystem: A General Approach and an Application to the South China Sea. In: K. Sherman,

L.M Alexander and B.D Gold (Eds.), *Large Marine Ecosystems: Stress, mitigation and Sustainability*. Washington, D.C: AAAS Press:3-14.

Purwanto, A.D & Harsanugraha, W.K. (2012). Analysis of Sea Surface Temperature (SST) in the Western Java Sea Based on NOAA-AVHRR and MODIS Data. Prosiding PIT MAPIN XIX. Makassar.

Purwanto, A.D., Prayogo, T., & Marpaung, S. (2020). Identification of Coral Reef Using Sentinel 2A Satellite Imagery (Case Study: Coastal Waters of Northern Nias). *Jurnal Teknologi Lingkungan, 21*(1), , 095-108.

Retnowati, E. (2011). Indonesian fishermen in the vortex of structural poverty (social, economic and legal perspectives)*Jurnal Perspektif, XVI*(3), 149-159.

Simbolon, D. & Girsang, H.S. (2009). Relationship between chlorophyl-a concentration and frigate mackerel catches in fishing ground of Pelabuhanratu waters. *Jurnal Penelitian Perikanan Indonesia, 15*(4), 297-305.

Simbolon, D., Silvia, S & Wahyuningrum, P.I. (2013). The Prediction of Thermal Front and Upwelling as Indicator of Potential Fishing Grounds in Mentawai Water. *Marine Fisheries, 4*(1), 85-95.

Suwargana, N., & Ariel, M., (2004). Determination of Sea Surface Temperature and Chlorophyll Concentration for Developing of Predictional / Fishing Ground Models using MODIS Data. *Jurnal Penginderaan Jauh dan Pengolahan Data Citra Digital, 1*(1), 1-13.

Telaumbanua, S.B. (2009). *A Study of Capture Fisheries Development in Nias Regency*. Tesis. Sekolah Pascasarjana Institut Pertanian Bogor: Bogor.

Winardi, & Manuputy, A.E.W. (2007). Nias Ecology Baseline. Jakarta: COREMAP II–LIPI.

Zainuddin, M., Kiyofuji, H., Saitoh, K., & Saitoh, S. (2006). Using multi-sensor satellite remote sensing and catch data to detect ocean hot spots for albacore (Thunnus alalunga) in the northwestern North Pacific. *Deep-Sea Research II 53*(3-4) 419–431.

Zainuddin, M. (2011). Skipjack Tuna In Relation To Sea Surface Temperature And Chlorophyll-A Concentration Of Bone Bay Using Remotely Sensed Satellite Data. *Jurnal Ilmu dan Teknologi Kelautan Tropis, 3*(1), 82-90.

Zebua, N.D. & Ramli. (2014). Analyze the effect of the number of fleets, the number of fisherman, GDP, and investment to the production of fisheries in the region of Nias (Panel Data Analysis).. *Jurnal Ekonomi dan Keuangan, 2*(8), 463-474.

ANALYSIS OF WATER PRODUCTIVITY IN THE BANDA SEA BASED ON REMOTE SENSING SATELLITE DATA

Sartono Marpaung[1]*, Rizky Faristyawan, Anang Dwi Purwanto, Wikanti Asriningrum, Argo Galih Suhadha, Teguh Prayogo, and Jansen Sitorus

[1]National Institute of Aeronautics and Space of Indonesian (LAPAN), Jakarta

*e-mail: sartonjam@gmail.com

Received: 20 December 2019; Revised: 1 June 2020; Approved: 17 June 2020

Abstract. This study examines the density of potential fishing zone (PFZ) points and chlorophyll-a concentration in the Banda Sea. The data used are those on chlorophyll-a from the Aqua MODIS satellite, PFZ points from ZAP and the monthly southern oscillation index. The methods used are single image edge detection, polygon center of mass, density function and a Hovmoller diagram. The result of the analysis show that productivity of chlorophyll-a in the Banda Sea is influenced by seasonal factors (dry season and wet season) and ENSO phenomena (El Niño and La Niña). High productivity of chlorophyll-a occurs during in the dry season with the peak in August, while low productivity occurs in the wet season and the transition period, with the lowest levels in April and December. The variability in chlorophyll-a production is influenced by the global El Niño and La Niña phenomena; production increases during El Niño and decreases during La Niña. Tuna conservation areas have as lower productivity of chlorophyll-a and PFZ point density compared to the northern and southern parts of the Banda Sea. High density PFZ point regions are associated with regions that have higher productivity of chlorophyll-a, namely the southern part of the Banda Sea, while low density PFZ point areas are associated with regions that have a low productivity of chlorophyll-a, namely tuna conservation areas. The effect of the El Niño phenomenon in increasing chlorophyll-a concentration is stronger in the southern part of study area than in the tuna conservation area. On the other hand, the effect of La Niña phenomenon in decreasing chlorophyll-a concentration is stronger in the tuna conservation area than in the southern and northern parts of the study area.

Keywords: *PFZ point, density, chlorophyll-a, water productivity, Hovmoller diagram, Banda Sea*

1 INTRODUCTION

Daily PFZ information has become a routine service for users in Indonesia. The information is generated automatically from ZPPI Auto Processing (ZAP) software with sea surface temperature satellite image data input. The distribution of PFZ information has densities that vary spatially and temporally. There are several factors that have an influence on density, namely: water productivity factors, seasonal factors and global phenomenon factors.

Sea waters that have high productivity rates are identified as potential fishing grounds or indicators of predicting fishing locations (Kasma, Osawa & Adnyana, 2007). Productivity of waters can be analysed through oceanographic parameters; for example, the concentration of chlorophyll-a. Chlorophyll-a is an active pigment in phytoplankton which plays an important role in the process of photosynthesis in seawaters and is a major food source for marine organisms (Hatta, 2014).

http://dx.doi.org/10.30536/j.ijreses.2020.v17.a3280

Chlorophyll-a has spatial and temporal variability. The spatial variation in the distribution of chlorophyll-a in the ocean depends on the geographical location and depth of water. This variation is caused by differences in sunlight intensity and nutrient concentrations in the waters. In addition, variations in chlorophyll-a concentration at sea level are closely related to upwelling events, seasonal changes and global phenomena in the ocean such as the El Niño Southern Oscillation (ENSO) (Kunarso, Hadi, Ningsih & Baskoro, 2011). Chlorophyll-a variability over the years is influenced by the ENSO phenomenon and the Indian Ocean Dipole (IOD) (Hottua, Kunarso & Rifai, 2015). However, the ENSO factor does not have a large influence (correlation of 0.33) on primary productivity in the Banda Sea (Sukresno & Iwan, 2008).

With the development of remote sensing technology, oceanographic parameter data are easily obtained and widely used in research. Nowadays remote sensing technology is an important instrument in obtaining overall sea water measurement data (Semedi & Hadiyanto, 2013). The advantage of using satellites for monitoring chlorophyll-a is because they can record data with a sweep width or a very wide area coverage. Research on the use of chlorophyll-a data from Aqua MODIS (Moderate Resolution Imaging Spectroradiometer) has been conducted by researchers in the marine field. Based on the results of research using chlorophyll-a data from MODIS, it's centration in the seas relates to the number of phytoplankton; more phytoplankton will increase chlorophyll-a concentration. High concentrations of chlorophyll-a can be found in coastal zones, and low concentrations in the open ocean (Winarso & Marini, 2014). Variations in chlorophyll-a and sea surface temperature during the period 2002-2017 were significantly influenced by the monsoon and Indian Ocean Dipole phenomena (Mashita & Lumban-Gaol, 2019).

This research aims to analyse the density of PFZ points and their relationship with water productivity based on chlorophyll-a parameters. Subsequently, certain factors that affect the productivity of chlorophyll-a spatially and temporally in the Banda Sea are analysed.

2 MATERIAL AND METHODOLOGY

The data used in this study consisted of chlorophyll-a, PFZ points and the southern oscillation index. The chlorophyll-a data from the Aqua MODIS satellites had a spatial resolution of 4 kilometers and a mothly temporal resolution. The chlorophyll-a data period was used from January 2003 to December 2018 (16 years), with data sourced from https://oceancolor.gsfc.nasa.gov/. PFZ point data were obtained from ZAP software, with daily sea surface temperature data from Aqua MODIS and S-NPP VIIRS satellites. The PFZ point data covered the period 2016 to 2018. The supporting data for the research were monthly data from the southern oscillation index, used as an indicator of the ENSO phenomenon. These data were sourced from Bureau of Meteorology Australian Government, http://www.bom.gov.au/climate/. The region of interest for the research was the Banda Sea and surrounding areas, at longitude 124°E to 132°E and latitude 2.5°S to 7°S, as shown in Figure 2-1. The sea area that is restricted by the red dashed line is a tuna conservation area. This area has been declared as a spawning and breeding ground for tuna fish and it is prohibited to conduct fishing operations there during the three months of October, November and

December (Menteri Kelautan dan Perikanan, 2015).

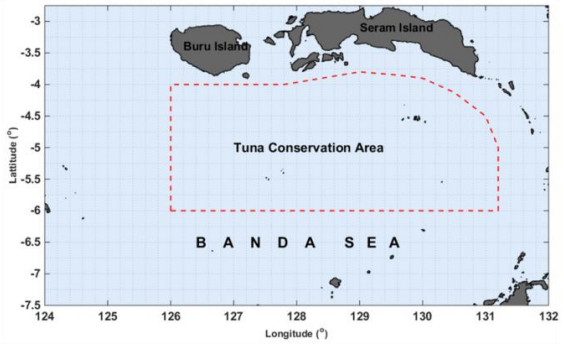

Figure 2-1: Region of interest

To achieve optimal research results and well-structured research implementation, the study was conducted based on the flow chart shown in Figure 2-2. The method used to detect thermal front events from sea surface temperature data was the single image edge detection (SIED) method (Cayula & Cornillon, 1995). From the results of the front detection, the polygon centre point was determined as the PFZ point, using the centre of mass of the polygon area (Hamzah et al., 2016). The annual distribution of PFZ points in the study area represented the PFZ point density. The spatially distributed PFZ point were placed into gridboxes sized 0.25° x 0.25° to produce density of PFZ. Each gridbox contained a number of PFZ points that ould be calculated using the counts of points in the polygon function. The purpose of producing PFZ points in the form of density is to facilitate analysis and to determine areas that have high or low density. To analyse the chlorophyll-a data, the statistical average composite method was used (the same month was averaged). To further develop the chlorophyll-a analysis, the Hovmoller diagram method was used. The Hovmoller diagram is a diagram to presents meteorological data or oceanographic parameters in form of xy coordinates; longitude versus time or time versus latitude (Hovmoller, 1949). In a Hovmoller diagram, the data are averaged for the same latitude or longitude over time. The application of a diagram aims to temporarily examine variations in the distribution of chlorophyll-a data based on latitude or longitude. From these variations, areas that have high or low water productivity can be determined. In this study, averaging of chlorophyll-a for the same longitude with respect to time was conducted to produce a plot of chlorophyll-a distribution data based on the time series versus latitude. In this way, variations in the distribution of chlorophyll-a data based on spatial latitude temporally can be analysed.

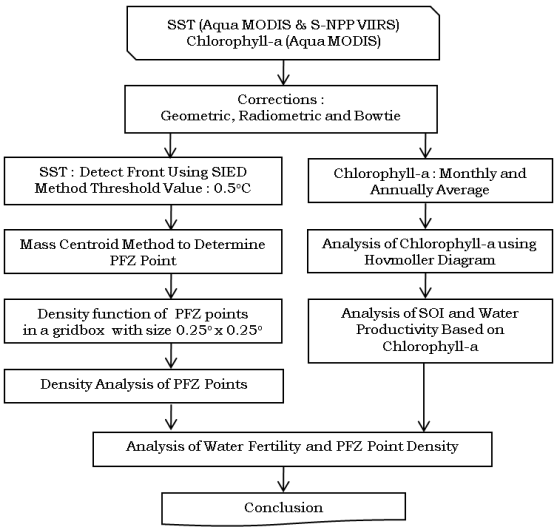

Figure 2-2: Research flowchart

3 RESULTS AND DISCUSSION

Daily PFZ information based on sea surface temperature from satellite data was generated automatically from the ZAP software. The annual spatial distribution of PFZ points per year for the study area from 2016 to 2018 was arranged in the form of a grid box sized 0.25° x 0.25° as shown in Figure 3-1. In 2016, there were no PFZ points in some regions, while most had an information density of 1-6 PFZ point per year. In 2017, there was an increase in PFZ point

information density compared to 2016. The study areas lacking PFZ point information steadily decreased, while those with an information density of 16-21 PFZ points or more significantly increased. In 2018, there was a further increase in PFZ point information density compared to 2016 and 2017. Temporally, there was an increase in PFZ point information density from 2016 to 2018, with the highest density occurring in 2018. Cases of low density and regions without PFZ point information in 2016 were likely due to the operation of the ZAP software which was not optimal that year. However, in 2017 and 2018 the ZAP operation was optimal. In general, the information density of PFZ points in the Banda Sea varied. Spatially, high PFZ point information density is found in the southern part of the Banda Sea, outside the tuna conservation area. Low information density is found in the tuna conservation area. In this study the results of the analysis of the information density of the PFZ points will be linked to the analysis of water productivity based on the chlorophyll-a parameter in the Banda Sea.

The results of the monthly chlorophyll-a data processing from the Aqua MODIS satellite from January 2003 to December 2018, namely the monthly composite average, is shown in Figure 3-2. Chlorophyll-a concentration ranges from 0.05 mg/m^3 to 5 mg/m^3 it has both spatial and temporal variability. Temporally, high chlorophyll-a concentrations occur from May to October (6 months), with the highest concentrations occurring in July and August. Low concentrations occur from November to April (6 months), with the lowest concentrations occurring in April and December. Periodically, there is an increase or decrease in the concentration of chlorophyll-a in the Banda Sea. This shows that the seasons, namely the wet season, dry season and the transition period have a strong influence on the variability (increase or decrease) of chlorophyll-a concentration in the Banda Sea. Spatially, the higher concentrations of chlorophyll-a were found in the southern part of the study area and the lower concentrations in the tuna conservation area. This result is very similar to the PFZ point density. A high density of PFZ points is found in the southern part of the study area and a low density in the tuna conservation area. To complete this analysis, follow-up analysis using the Hovmoller diagram was performed.

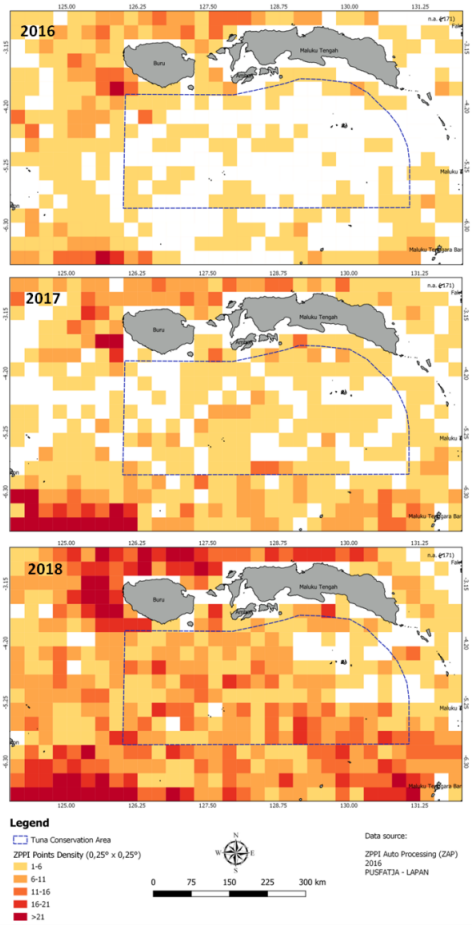

Figure 3-1: Density of PFZ points per year from 2016 to 2018

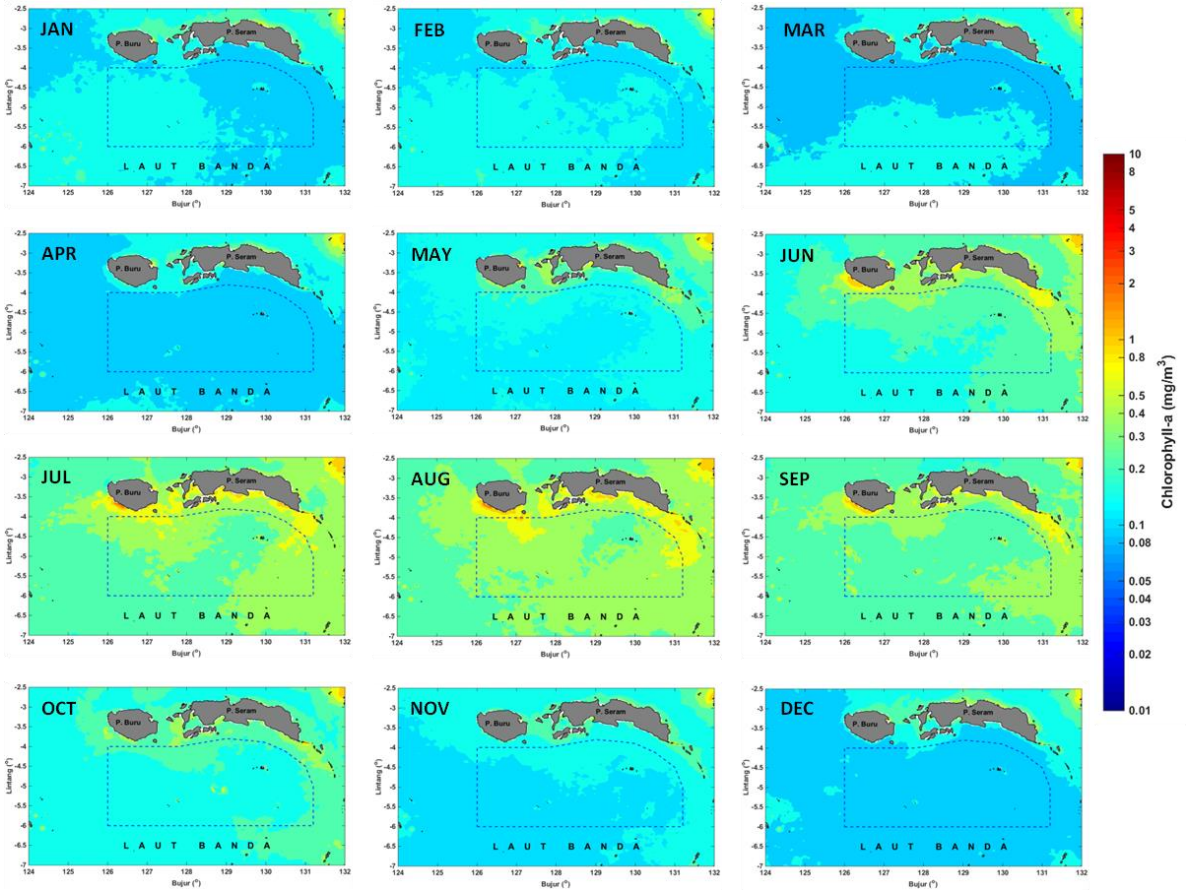

Figure 3-2: Monthly composite average of chlorophyll-a

After applying the Hovmoller diagram, the results of the distribution of chlorophyll-a were obtained in the form of xy coordinates; time (month) versus latitude as shown in Figure 3-3. In the Hovmoller diagram, chlorophyll-a averaging between pixels in the same longitude was performed to research the variability of chlorophyll-a based on latitude. On the basis of this, the tuna conservation area is located 4°S to 6°S (dashed red line). Chlorophyll-a concentration values range from 0.1 mg/m^3 to 0.7 mg/m^3. Based on the latitude of the study area, the coastal areas of Buru and Seram Islands (2.5°S to 4°S) have higher chlorophyll-a concentrations than in the tuna conservation area (4°S to 6°S) or the southern part of the study area (6°S to 7°S). In general, coastal areas have higher chlorophyll-a concentrations compared to the high seas. Temporally, low chlorophyll-a concentrations occur from January to April and from November to December. The lowest concentrations occur in April, November and December. High concentrations occur in May to October. The highest chlorophyll-a concentrations occur in July and August. The results of this analysis corroborate those shown in Figure 3-2. The monsoon system that occurs in Indonesia, or seasonal change factors, has a strong influence on the chlorophyll-a variability in the Banda Sea. In the dry season, which occurs in June, July and August (JJA), the concentration of chlorophyll-a increases significantly and reaches its peak in July and August. Increased chlorophyll-a is due to the influence of increased upwelling events in the dry season, which causes nutrients to rise to the surface. In wet season, in December, January and February (DJF) and in the transition period, the concentration of chlorophyll-a is lower than in the dry

season. The decrease in concentration is thought to be due to a fall in the intensity of upwelling events and an increase in the volume of seawater from rainfall. The overall results show that water productivity based on chlorophyll-a concentration is high in the east monsoon (dry season) and low in the west monsoon (wet season) and transition period due to the influence of seasonal factors.

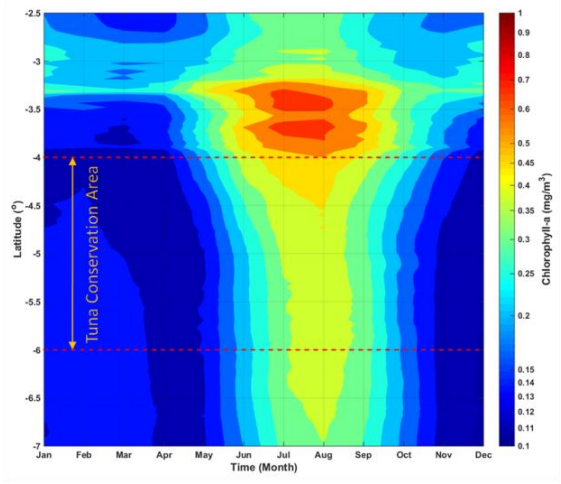

Figure 3-3: A Hovmoller diagram of monthly chlorophyll-a concentration (time vs latitude)

The monthly chlorophyll-a average shows the relationship between the influence of seasons on productivity variation between months and seasons (temporal). The following analysis examined the annual variability of chlorophyll-a from 2003 to 2018, as shown in Figure 3-4. From these results variations in chlorophyll-a over the years can be investigated, namely the increases and decreases in chlorophyll-a concentration. The results show that the average chlorophyll-a concentration per year varied in value between 0.1 mg/m^3 to 3 mg/m^3. In general, chlorophyll-a is higher on the southern coasts of Buru and Seram Islands, and in the southern part of the study area. Chlorophyll-a concentration showed an increase in 2006 and 2015. The lowest chlorophyll-a concentration during the observation period occurred was in 2010. For more detailed analysis, a Hovmoller diagram and El Niño Southern Oscillation (ENSO) index data were analysed during the period of observation.

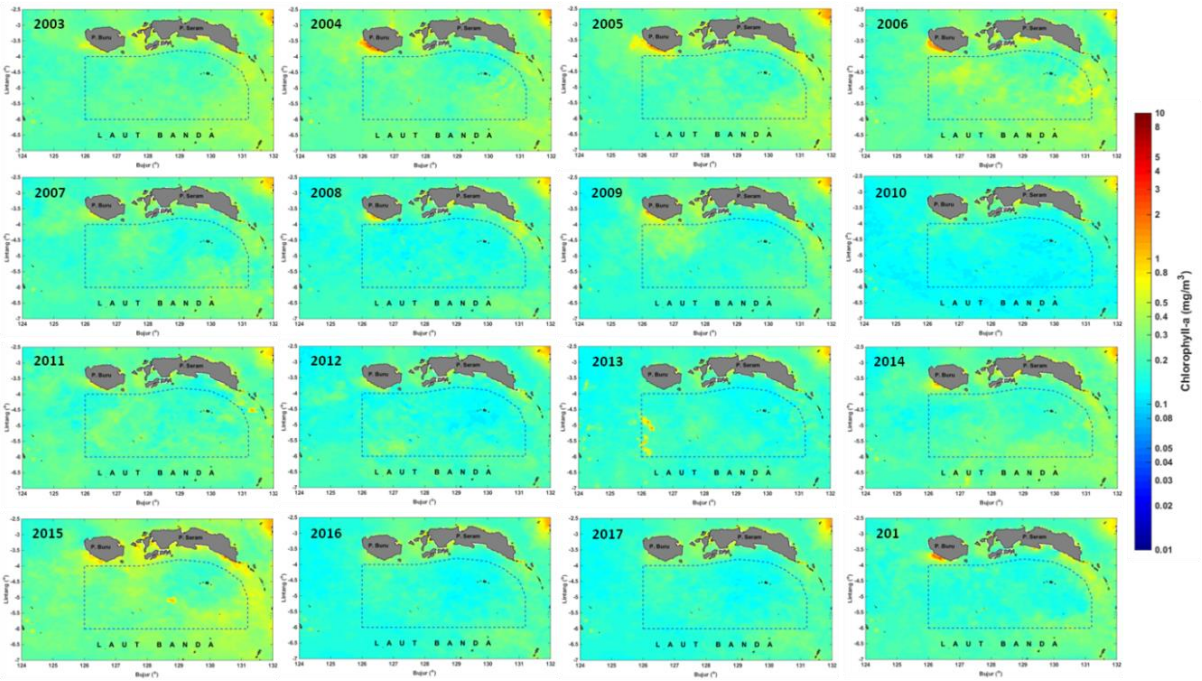

Figure 3-4: Average annual levels of chlorophyll-a from 2003 to 2018

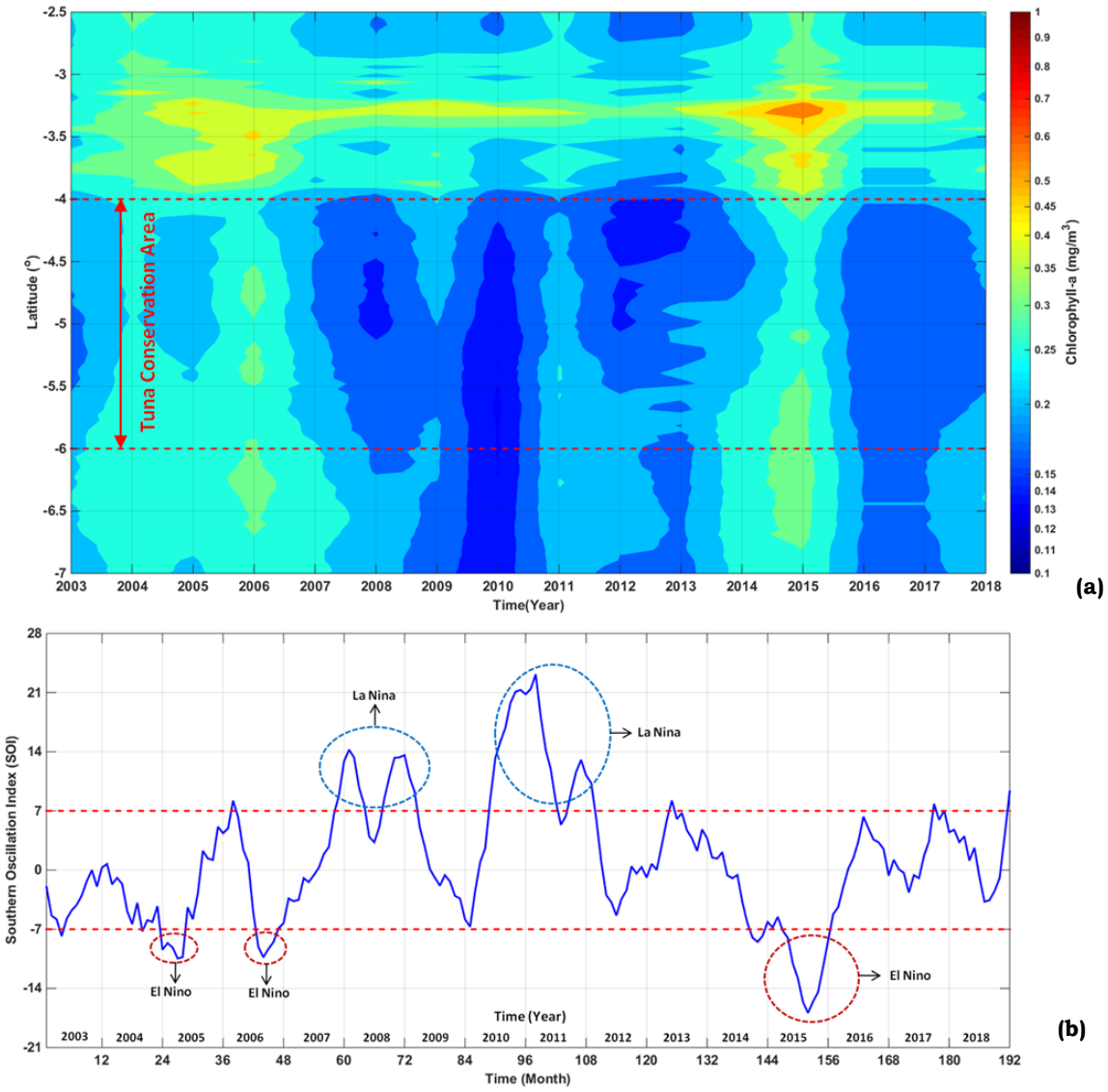

Figure 3-5: (a) Hovmoller diagram of annual chlorophyll-a from 2003 to 2018; (b) Time series of southern oscillation index from 2003 to 2018

The application of the Hovmoller diagram method aimed to analysed the variability in chlorophyll-a between latitudes and years (years versus latitudes) and their relation to ENSO phenomena. The results from applying the Hovmoller diagram and the southern oscillation index values of ENSO phenome are shown in Figure 3-5. Spatially based on latitude, the lowest chlorophyll-a concentration is found in the tuna conservation area with higher chlorophyll-a concentrations in the southern part of the study area and the highest ones in the north. Temporally, the concentration of chlorophyll-a increased in 2005, 2006 and 2015. During these year, there were El Niño events (shown by red dashed lines), resulting in an increase in chlorophyll-a in the study area. The effect of El Niño phenomena in increasing chlorophyll-a concentration is stronger in the southern part of study area than in the tuna conservation area. In 2008 and 2010 there were the La Niña events (shown by blue dashed lines), which resulted in a decrease in chlorophyll-a concentration in the study area. The biggest decrease in chlorophyll-a concentration occurred

with the La Niña event of 2010, with the highest SOI value. The effect of La Niña phenomena in decreasing chlorophyll-a concentration was stronger in the tuna conservation area than in the southern and northern parts of the study area. The results of the analysis also show that the tuna conservation area had lower water productivity based on chlorophyll-a concentration compared to the northern and southern parts. Water productivity in the Banda Sea is strongly influenced by the ENSO phenomenon. El Niño events result in an increase in upwelling whereas during La Niña events there is a decrease. In upwelling events, there occurs a movement of seawater mass from the bottom layer to surface of the sea bringing nutrients or phytoplankton up to the surface (Ramansyah, 2009; Putra, 2012; Ratnawati, 2017). This causes the concentration of chlorophyll-a to rise at the sea surface.

The results of the analysis show that the high density PFZ point regions were associated with those with higher water productivity based on chlorophyll-a concentration, namely in the southern part of the study site. The low density PFZ point regions corresponds to those with low water productivity/ chlorophyll-a concentration, namely in the tuna conservation area. Seasonal factors, namely the wet season (west monsoon) and the dry season (east monsoon) have a strong influence on the variability of chlorophyll-a concentration/water productivity in the Banda Sea. In the east season, the productivity of chlorophyll-a increases significantly and reaching its peak value in August. In the wet season, chlorophyll-a decreases in productivity, with the lowest levels occurring in December. During the transition from the wet season to the dry season and from the dry season to the wet season, the value of chlorophyll-a concentration varies (either increasing or decreasing). Chlorophyll-a levels are lowest in April and November. The global phenomena of El Niño and La Niña have a strong influence on productivity variability in the Banda Sea. The El Niño phenomenon results in increased chlorophyll-a concentrations while La Niña events result in decreased chlorophyll-a concentrations. The increases occurring during El Niño are due to the increase in upwelling events which bring nutrients or phytoplankton to the surface of the sea. On the other hand during La Niña events upwelling events decreases due to lower sea surface temperatures than in the layers below.

4 CONCLUSION

The variability of water productivity based on chlorophyll-a concentration in the Banda Sea is influenced by seasonal factors (dry season and wet season) and ENSO phenomena (El Niño and La Niña). In the dry season the water productivity of chlorophyll-a increases and peaks in August. During the wet season and transition period, productivity decreases with the lowest levels occuring in April and December. Water productivity of chlorophyll-a is influenced by global phenomena, namely El Niño and La Niña. In El Niño events chlorophyll-a increases, and in La Niña event it decreases. The high density PFZ point regions were associated with higher water productivity of chlorophyll-a concentration, namely in the southern part of the study area. The low density PFZ point regions corresponded to areas of low chlorophyll-a productivity, namely in the tuna conservation area. The effect of the El Niño phenomenon in increasing chlorophyll-a concentration is stronger in the southern part of study area than in the tuna conservation area while the effect of La Niña in decreasing

chlorophyll-a concentration is stronger in the tuna conservation area than in the southern and northern parts of the study area.

ACKNOWLEDGEMENTS

We would like to thank Dr. M. Rokhis Khomarudin, Syarif Budhiman, M.Sc., Dr. Ratih Dewanti, Dr. Ing. Widodo Pranowo and Dr. Bidawi Hasyim for some directions and suggestions for this paper. This research was supported and funded by Remote Sensing Applications Centers of National Institute of Aeronautics and Space of Indonesia.

AUTHOR CONTRIBUTIONS

Analysis of Water Productivity In The Banda Sea Based On Remote Sensing Satellite Data. Lead Author: Sartono Marpaung, Co-Author: Rizky Faristyawan, Anang Dwi Purwanto, Wikanti Asriningrum, Argo Galih Suhadha, Teguh Prayogo, and Jansen Sitorus.

REFERENCES

Cayula, J.F. & Cornillon, P. (1995). Multi-image Edge Detection for SST Images. *Journal of Atmospheric and Oceanic Technology*. *12*(4), 821–829.

Hamzah, R., Prayogo, T. & Marpaung, S. (2016). Method of Determination Points Coordinate for Potential Fishing Zone Based on Detection of Thermal Front. *Journal of Remote Sensing and Digital Image Processing*, *13*(2), 97-108.

Hatta, M. (2014). Relationship between Oceanographic Parameter and Chlorophyll-a Concentration in the East Season in the Northern of Papua. *Torani Jurnal Ilmu Kelautan dan Perikanan*, *24*(3), 29 – 39.

Hottua, E.N., Kunarso & Rifai, A. (2015). Variability of Sea Surface Temperature and Chlorophyll-a, It's Relationship to El Niño Southern Oscillation (ENSO) and Indian Ocean Dipole (IOD) in Upwelling Period from 2010 to 2014 in the Indian Ocean). *Jurnal Oseanografi*, *4*(4), 661-669.

Hovmoller, E. (1949). The Trough-and-Ridge Diagram. *Tellus*, 1(2), 62–66, doi:10.1111/j.2153-3490.1949.tb01260.x.

Kasma, E.T., Osawa, I.W.S. & Adnyana (2007). Estimation of Primary Productivity for Tuna in Indian Ocean. *Ecotrophioc*, *4* (2), 86-91.

Kunarso, Hadi, S., Ningsih, N.S. & Baskoro, M.S. (2011). Variability of Temperature and Chlorophyll-a in Upwelling Regions on Variations in ENSO and IOD Events in the Sea Waters of Southern Java to Timor. Indonesian *Journal of Marine Sciences*, *16* (3), 171-180.

Mashita, M. & Lumban-Gaol, J. (2019). Variability of Sea Surface Temperature (SST) and Chlorophyll-A Concentrations in the Eastern Indian Ocean during the Period 2002–2017. *International Journal of Remote Sensing and Earth Sciences*, *16*(1), 55–62.

Menteri Kelautan dan Perikanan, (2015). Prohibition of Fish Catching in the Territory of Republic of Indonesia Fisheries Management WPP 714. *PERMEN-KP* No. 4.

Putra, E. (2012). Variability of Chlorophyll-a Concentration and Sea Surface Temperature from MODIS Satellite Imagery and Its Relationship with the Results of Catches Pelagic Fish in the Java Sea Waters. *Skripsi*, Departemen Ilmu dan Teknologi Kelautan, Fakultas Perikanan dan Ilmu Kelautan, Institut Pertanian Bogor.

Ramansyah, F. (2009). Determination of Pattern the Chlorophyll-a Concentration Distribution in the Sunda Strait and Surroundings by Using Aqua MODIS Data). *Skripsi*, Program Studi Ilmu dan Teknologi Kelautan, Fakultas Perikanan dan Ilmu Kelautan Institut Pertanian Bogor,

Ratnawati, H.I., Hidayat, R., Bey, A., & June, T. (2017). Upwelling in the Banda Sea and Southern Java Coast and its Relationship with ENSO and IOD. *Omni-Akuatika*, *12*(3), 119–130.

Semedi, B. & Hadiyanto, A.L. (2013). Forecasting the Fishing Ground of Small Pelagic Fishes in Makasar Strait using Moderate Resolution Image Spectro radiometer Satellite Images. *Journal of Applied Environmental and Biological Sciences*, *3* (2), 29 – 34.

Sukresno, B. and Iwan, K.S. (2008). Observation of the Influence of ENSO on Primary Productivity and Fisheries Potential Using Satellite Data in the Banda Sea. *Globe*, *10*(2), 97-107.

Winarso, G. & Marini, Y. (2014). MODIS Standard (OC3) Chlorophyll-A Algorithm Evaluation in Indonesian Seas. *International Journal of Remote Sensing and Earth Sciences*, *11*(1), 11–20.

ASSESSMENT OF THE ACCURACY OF DEM FROM PANCHROMATIC PLEIADES IMAGERY (CASE STUDY: BANDUNG CITY. WEST JAVA)

Rian Nurtyawan[1]* and Nadia Fiscarina
[1]Department of Geodesy Engineering, National Institute of Technology,
23 PH.H. Mustofa Street, 40124 Bandung, Indonesia
*e-mail: nurtyawan70@gmail.com
Received: 2020-04-26; Revised: 2020-06-20; Approved: 2020-06-23

Abstract. Pleiades satellite imagery is very high resolution. with 0.5 m spatial resolution in the panchromatic band and 2.5 m in the multispectral band. Digital elevation models (DEM) are digital models that represent the shape of the Earth's surface in three-dimensional (3D) form. The purpose of this study was to assess DEM accuracy from panchromatic Pleaides imagery. The process conducted was orthorectification using ground control points (GCPs) and the rational function model with rational polynomial coefficient (RFC) parameters. The DEM extraction process employed photogrammetric methods with different parallax concepts. Accuracy assessment was made using 35 independent check points (ICPs) with an RMSE accuracy of ± 0.802 m. The results of the Pleaides DEM image extraction were more accurate than the National DEM (DEMNAS) and SRTM DEM. Accuracy testing of DEMNAS results showed an RMSE of ± 0.955 m. while SRTM DEM accuracy was ± 17.740 m. Such DEM extraction from stereo Pleiades panchromatic images can be used as an element on base maps with a scale of 1: 5.000.

Keywords*: Pleiades. Digital Elevation Model. Stereo. Accuracy*

1 INTRODUCTION

Remote sensing satellites and Earth observation satellites are currently used in various applications. including mapping. resource management. disaster simulation. and recently in geo-online applications such as Google Earth (Bignone & Umakawa, 2008). Satellite imagery continues to improve from low resolution to very high resolution. Since 2000. the development of optical sensors with very high resolution such as IKONOS. QuickBird and GeoEye has been rapid. with Pleiades being very high-resolution satellites recently launched (Benarchid. Raissouni. Adib. Abbous. Azyat. Achhab. Lahraoua. Chahboun. 2013). Pleiades satellite imagery comprises high-resolution optical images used for Earth observation missions with civil and military purposes, under the development of the Centre National d'Etudes Spatiales (CNES). CNES is the French space agency, and develops satellites with very high resolution. This study involves one satellite that provides panchromatic and multispectral high resolution images (Baillarin, Panem, & Cazalet, 2012). In the panchromatic band. Pleiades satellite imagery has a spatial resolution of 0.5 m. and 2 m in its multispectral band (Aryani, Harto, & Soeksmantono, 2017).

The Pleiades are examples of very high resolution (VHR) satellites. VHR is superior to the resolution of other satellites in producing DEMs. VHR optical satellites offer the most widely available overlapping area and B/H ratio in stereo images. which results in exceptional image matching accuracy and in the resulting DEM. In addition. the

http://dx.doi.org/10.30536/j.ijreses.2020.v17.a3329

opportunity to revisit frequencies every 3 to 5 days increases the ongoing monitoring of variations in the Earth's surface (Deilami & Hashim, 2011)

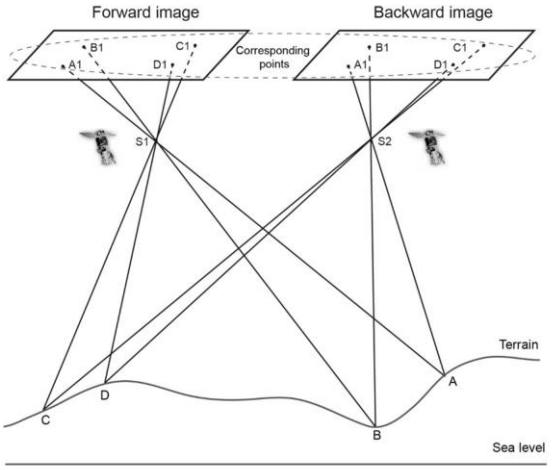

Figure 1-1: Principle diagram of DEM generation from stereo imagery (Wang et al.. 2019).

The basic theory for obtaining DEMs using satellite stereo images is to synchronise feature points according to overlapping images and to produce coordinates in the 3D position of these points. then to reconstruct the spatial stereo model further and obtain 3D information according to the actual position on the ground (Figure 1-1) (Wang. Ren. Wu. Lei. Gong. Ou. Zhang. Huiping. 2019). The Pleiades provide a rational polynomial coefficient (RPC) file containing a rational function model that represents the relationship between objects and image coordinates (Dolloff & Theiss, 2014). The ratio polynomial is defined as follows:

$$L = L_S \times \frac{NUM_1(U.V.W)}{Den_1(U.V.W)} + L_0.S = S_S \times \frac{NUM_s(U.V.W)}{Den_s(U.V.W)} + S_0 \quad (1\text{-}1)$$

$$\frac{NUM_1(U.V.W)}{Den_1(U.V.W)}.\frac{NUM_s(U.V.W)}{Den_s(U.V.W)}$$

where is the normalised image coordinates; (U.V.W) are the normalised ground coordinates; (L_s.S_s) is the normalised proportional parameter; and (L_0.S_0) is the normalised translation parameter. Num_l *(U.V.W). Denl(U.V.W). Num*$_s$*(U.V.W).* and Den_s*(U.V.W)* can be expressed as the following polynomials:

$$m = a_1 + a_2V + a_3U + a_4W + a_5VW + a_6VW + a_7UW + a_8V^2 + a_9U^2 + a_{10}W^2 + a_{11}UVW + a_{12}V^3 + a_{13}VU^2 + a_{14}VW^2 + a_{15}V^2U + a_{16}U^3 + a_{17}UW^2 + a_{18}V^2W + a_{19}U^2W + a_{20}W^3 \quad (1\text{-}2)$$

All the coefficients of the four polynomial functions are stored in one file containing 80 rational polynomial coefficients (RPCs). through which the ground coordinates can be calculated.

The spatial resolution of the Pleiades satellites makes them an alternative choice for creating a digital elevation model (DEM). In principle. DEMs are digital models that represent the shape of the Earth's surface in three dimensions (Indarto & Prasetyo, 2014). DEMs can be obtained by various techniques such as stereo photogrammetry from aerial photo surveys. Light Detection and Ranging (LiDAR). Interferometric Synthetic Aperture Radar (IFSAR). and mapping surveys. Other methods that can be used to produce DEMs include RTK-GPS. block adjustments from satellite imagery and topographic maps (Naim, Abdullah, & Hashim, 2014).

This study aims not only to determine the accuracy of the results of the DEM extraction using panchromatic Pleiades satellite imagery. but also to determine the scale that matches the resulting DEMs. The method used is extraction. which in mainly employs the parallax concept. The scope of the research is limited to the following issues:

1. The data used are Pleiades panchromatic satellite stereo image acquired in July 2014.
2. Nine ground control points (GCPs) are used for orthorectification of the images.

3. The orthorectification process uses the rational function model (RFM) method with rational polynomial coefficient (RPC) parameters.
4. 36 independent check points (ICPs) are used to test the accuracy of the DEM extraction results.

2 MATERIALS AND METHODOLOGY

2.1 Data

The Pleiades satellite system was designed for both civil and military purposes under the French-Italian ORFEO (Optical & Radar Federated Earth Observation) program in 2001-2003. The constellation comprises two satellites. Pleiades 1A and Pleiades 1B. operating in the same phased orbit. The data used in this study were panchromatic Pleiades stereo images acquired on 17 July 2014. Detailed product parameters are shown in Figures 2-1 and 2-2.

Product Parameters			
Product Id	DS_PHR1B_201407170319013_JP3_PX_E107S07_0803_00992		
Acquisition date	2014-07-17 03:19:36.4		
Platform	PHR 1B		
Band ID	PA		
Incidences and orientation			
	start	middle	end
Orientation	179.9747768	179.9812635	180.0486867
Global incidence	9.826442716	9.894546537	9.963007981
Accross / along the track	-6.149603156094127 /	-6.246824334654747 /	-6.351652715977125 /
incidence	-7.722987556	-7.733928909	-7.738542377

Figure 2-1: Product Parameters of Left-hand Side Image

Product Parameters			
Product Id	DS_PHR1B_201407170319304_JP3_PX_E107S07_0803_00987		
Acquisition date	2014-07-17 03:20:05.5		
Platform	PHR 1B		
Band ID	PA		
Incidences and orientation			
	start	middle	end
Orientation	179.9655127	180.0307129	180.130577
Global incidence	13.81085112	13.86180214	13.91234192
Accross / along the track	-9.854213176964146 /	-9.937346268356288 /	-10.01376001475964 /
incidence	9.867501346	9.858379709	9.855044538

Figure 2-2: Product Parameters of Right-hand Side Image

2.2 Location

The research location was the city of Bandung. West Java. Indonesia. located at latitude 6°55' south and longitude 107°36' east. The total area of Bandung City is 16.729.65 Ha. The location can be seen in Figure 2-3.

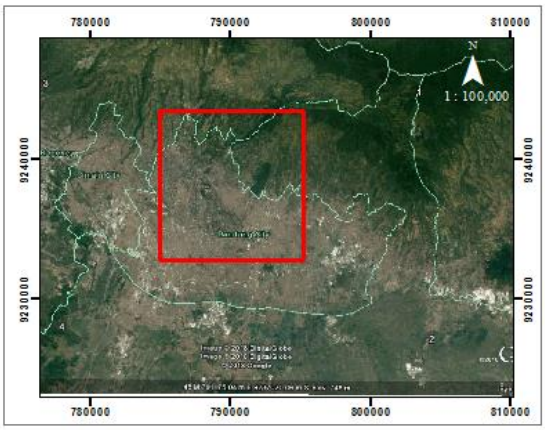

Figure 2-3: Research Area (shown in red rectangle)
(Source: Google Earth.2018)

2.3 Methods

The implementation of the research consisted of several steps (Figure 2-4):

1. Panchromatic Pleiades Stereo Images.

This study uses panchromatic Pleiades stereo image data with a spatial resolution of 0.5 m (see Figures 2-5A and 2-5B).

2. Image Orthorectification.

An image orthorectification process was conducted to reduce the effect of geometric distortion of objects on the images. using nine ground control points (GCPs) obtained by GPS measurements. The distribution of the GCPs can be seen in Figure 2-6 (shown by yellow dots).

Subsequently the root mean square error (RMSE) was calculated. The orthorectification process was performed using the rational function model (RFM) method (Rudianto, 2011). with rational polynomial coefficient (RPC) parameters. In the implementation of image orthorectification. the RMSE value must comply with the tolerance. which is calculated by Algorithm 0.5 x spatial resolution (Rudianto, 2011). accordingly. the tolerance to comply requirements is ≤ 0.25 m.

3. Epipolar Images

Epipolar images are stereo pairs in which the left and right images are oriented in such a way that ground feature points have the same coordinates on both images. Using epipolar images removes one dimension of variability. thus greatly increasing the speed of image-matching processing as well as the reliability of the matching results.. Hence epipolar images are used for the extraction of the DEM.

4. DEM extraction

The stages of DEM extraction are as follows:

a. Convert raw images to epipolar images.
b. DEM extraction from the epipolar images. The result of this stage is a DEM which has not been georeferenced.
c. DEM geocoding. which is the process of forming georeferenced DEMs.

5. Accuracy Test

An accuracy test was then performed using 36 independent check points (ICPs) obtained from the GPS measurement results (shown as red dots in Figure 2-7).

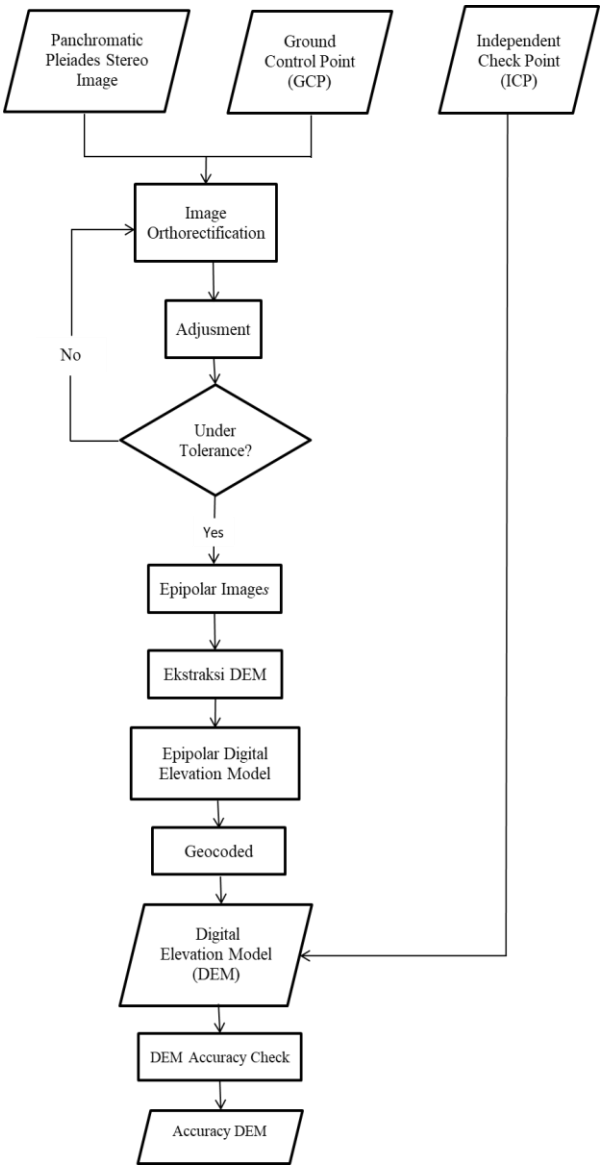

Figure 2-4: Research Flowchart

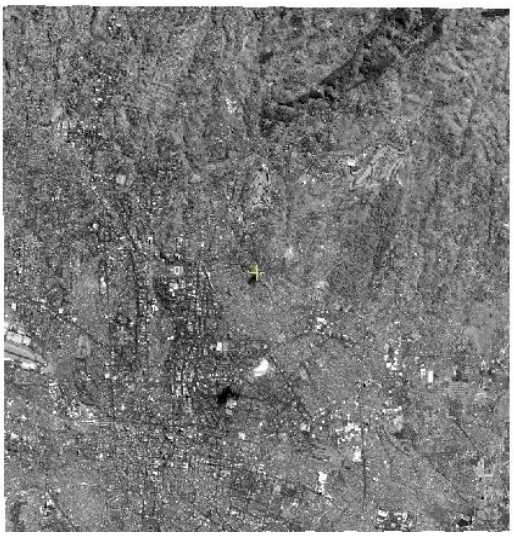

Figure 2-5A: Left-hand Side Image

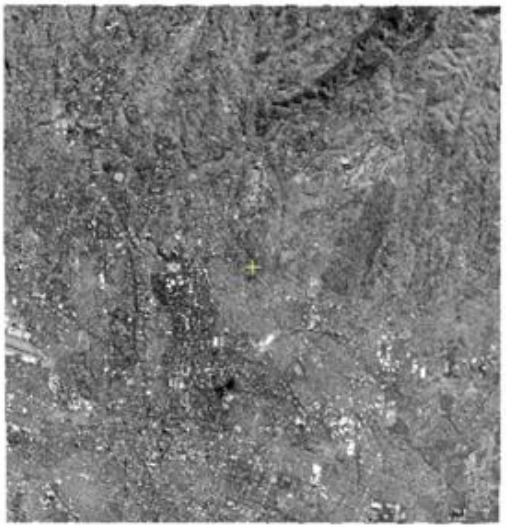

Figure 2-5B. Right-hand Side Image

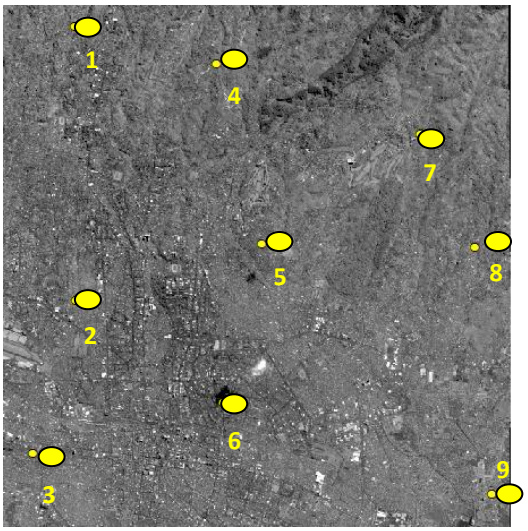

Figure 2-6. Distribution of GCPs

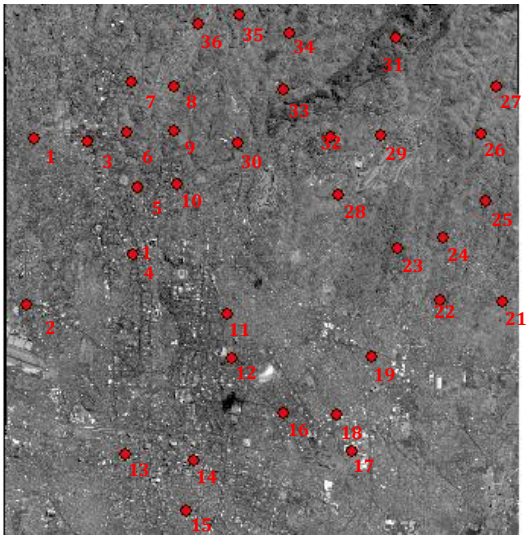

Figure 2-7: Distribution of ICPs

3 RESULTS AND DISCUSSION

The DEM extraction research using panchromatic Pleiades satellite imagery produced a DEM map. The research results can be seen in Figure 3-1.

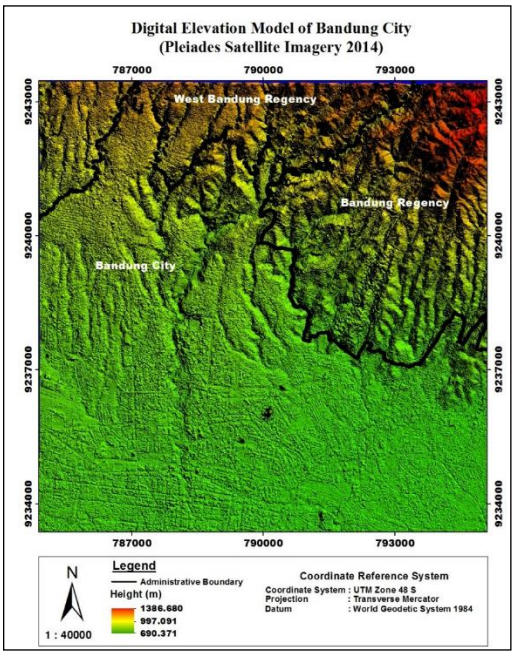

Figure 3-1: Digital Elevation Model Map

The DEM extraction results provide information on a height range of 690.70 m-1386.68 m (Figure 3-1). DEM surface roughness shows the surface representation of the city of Bandung.

The orthorectification process employed nine GCPs. The results of the process can be seen in Table 3-1. By using nine GCPs. an RMSE of 0.218 m (Equation 3-1) was obtained. therefore complying with the tolerance used. The DEM accuracy testing process was then conducted. with the results using high ICP data shown in Table 3-2.

$$RMSE_{horizontal} = \sqrt{\frac{\sum(\Delta X)^2+(\Delta Y)^2}{n}} \quad (3\text{-}1)$$

n = number of sample observations
ΔX = difference in the coordinates of the x-axis observations and models
ΔY = difference in the coordinates of the y axis observations and models

$$RMSE_{vertikal} = \sqrt{\frac{\sum(\Delta Z)^2}{n}} \quad (3\text{-}2)$$

n = number of sample observations
ΔZ = difference in the coordinates of the Z-axis observations and models

Table 3-1: Orthorectification Results

GCP	ΔX (m)	ΔY (m)	$(\Delta X^2+\Delta Y^2)$
GCP9	0.160	0.180	0.058
GCP59	0.180	-0.140	0.052
GCP90	-0.050	0.100	0.0125
GCP16	0.110	0.180	0.0445
GCP45	-0.010	-0.050	0.0026
GCP76	-0.050	0.150	0.025
GCP22	0.230	0.290	0.137
GCP41	0.180	-0.130	0.0493
GCP91	-0.040	0.200	0.0416
		Σ=	0.3809
		RMSE=	0.218

Z GCP is the coordinate height of the GCP point. Z Pleiades is the coordinate height obtained from DEM extraction. and ΔZ is the coordinate difference between the height of the extraction result (model) and the GCP height (GPS). An accuracy test was performed using 35 independent check points (ICPs) and an RMSE (Equation 3-2) of 0.802 m was generated. The level of accuracy was influenced by Bandung's topographical conditions. For example. ICP11. ICP5 and ICP24 displayed high accuracy. while the level of accuracy was not so good at low levels. for example ICP26. ICP34 and ICP97. The highlands generally comprise open land. while the lowlands generally consist of buildings and settlements. facts which affect noise when recording and consequently the level of accuracy.

In this study. an accuracy test for the national DEM and SRTM DEM was also performed. The accuracy of the test results for the DEMNAS image produced an RMSE of ±0.955 m. while the test results on the SRTM image produced an RMSE of ±17.740 m.

Furthermore. the accuracy of the vertical geometry was calculated using the linear error (LE90) (Equation 3-3) formula obtained from Perka BIG Number 6 of 2018. The calculation process was as follows:

$$\mathbf{LE90 = 1.6499 \times RMSEz} \quad (3\text{-}3)$$
$$= 1.6499 \times 0.802$$
$$= 1.323$$

After calculation. vertical accuracy was used to determine the scale of the base map that corresponds to the magnitude of LE90. The vertical accuracy standards can be seen in Table 3-3.

Table 3-2: GPS and Pleiades DEM Accuracy Test Results

No.	ICP	Z GCP/Z_1 (m)	Z Pleiades/Z_2 (m)	(ΔZ^2)
1.	ICP51	816.883	816.746	0.019
2.	ICP26	886.426	889.912	12.155
3.	ICP3	987.997	987.571	0.181
4.	ICP34	856.929	858.606	2.811
5.	ICP48	812.813	811.914	0.808
6.	ICP42	831.725	831.052	0.453
7.	ICP87	721.956	722.415	0.211
8.	ICP15	965.263	965.973	0.505
9.	ICP30	903.376	903.839	0.215
10.	ICP84	706.705	706.001	0.496
11.	ICP21	1141.258	1141.464	0.206
12.	ICP11	1260.063	1260.165	0.101
13.	ICP28	935.231	934.199	-1.031
14.	ICP18	1005.249	1005.691	0.442
15.	ICP88	728.064	728.804	0.740
16.	ICP17	1017.145	1018.033	0.889
17.	ICP63	714.930	715.563	0.634
18.	ICP60	774.584	774.409	-0,.174
19.	ICP31	936.756	937.104	0.348
20.	ICP66	751.702	752.240	0.537
21.	ICP75	719.183	719.182	-0.001
22.	ICP24	956.858	956.781	-0.077
23.	ICP74	711.489	711.995	0.506
24.	ICP29	927.524	927.430	-0.095
25.	ICP5	1088.176	1088.154	-0.022
26.	ICP27	942.342	942.050	-0.293
27.	ICP97	716.974	717.792	0.818
28.	ICP7	1102.241	1102.826	0.585
29.	ICP38	872.076	872.101	0.024
30	ICP43	855.554	856.628	1.074
31.	ICP52	743.244	743.152	-0.092
32.	ICP37	862.308	862.050	-0.259
33.	ICP23	941.857	941.906	0.049
34.	ICP56	773.491	773.577	0.086
35.	ICP6	1118.624	1118.295	-0.329
			Σ=	**22.5207**
			N=	**35**
			RMSE=	**0.802**

Table 3-3: Vertical Accuracy Standards

No.	Map Scale	Vertical Accuracy (m)		
		Class 1	Class 2	Class 3
1	1 : 10000	2	3	4
2	1 : 5000	1	1.5	2
3	1 : 2500	0.5	0.75	1

(Source: (Perka BIG, 2018)

Based on the accuracy of the DEM Pleiades test results using high ICP an RMSE value of 0.802 was obtained. with the LE90 result being 1.323. According to Perka BIG No. 6 of 2018 concerning Technical Guidelines for the Accuracy of Basic Maps. the results of the extraction of DEMs from panchromatic Pleiades stereo images can be used as a base map with a scale of 1: 5000 with class 2 accuracy. in which the maximum permissible accuracy allowed is 1.5 m.

4 CONCLUSION

The conclusion that can be drawn from the results of the study is that the DEM extraction using panchromatic Pleiades stereo imagery and GCP for orthorectification stages has a tolerable RMSE value. The value generated at the orthorectification stage was $\pm$0.218 m. The accuracy of the test results using ICP obtained an RMSE value of $\pm$0.802. The results of the Pléaides DEM image extraction were more accurate compared to that of the national or SRTM DEMs. Testing of the accuracy of the national DEM resulted in a *RMSE* of ± 0.955 m. while for SRTM DEM it was *RMSE* ± 17.740 m.

According to Perka BIG No. 6 of 2018 concerning the Technical Guidelines for the Accuracy of Basic Maps. the test results can be used for base maps on a 1: 5000 scale. with class 2 accuracy. namely 1.5 m.

ACKNOWLEDGEMENTS

The author thanks PT. Digital Imaging Geospatial which provided the data for the research.

AUTHOR CONTRIBUTIONS

Assessment Of The Accuracy Of Dem From Panchromatic Pleiades Imagery (Case Study: Bandung City. West Java). Lead Author: Rian Nurtyawan, Co-Author: Nadia Fiscarina.

REFERENCES

Wang, S., Ren, Z., Wu, C., Lei, Q., Gong, W., Ou, Q., & Zhang, H. (2019). DEM generation from Worldview-2 stereo imagery and vertical accuracyassessment for its application in active tectonics. *Geomorphology*, 107-118.

Aryani, D. I., Harto, A. B., & Soeksmantono, B. (2017). Kajian Prosedur Pembuatan Automatic DEM (Digital Elevation Model) Menggunakan Citra Satelite Pleiades (Studi Kasus Kota Bandung-Jawa Barat). *Gea. Jurnal Pendidikan Geografi*, 159-170.

Baillarin, S., Panem, C., & Cazalet, F. B. (2012). Pleiades-HR System Product Performance After In-Orbit Commissioning Phase. *International Archives of the Photogrammetry* (p. B1). Melbourne, Australia: Remote Sensing and Spatial Information Sciences.

Benarchid, O., Raissouni, N., Adib, S. E., Abbous, S., Azyat, A., Achhab, B., . . . Chahboun, A. (2013). Building Extraction

using Object-Based Classification and Shadow Information in Very High Resolution Multispectral Images,a Case Study: Tetuan, Morocco. *Canadian Journal on Image Processing and Computer Vision, 4*, 1.

Bignone, F., & Umakawa, H. (2008). Assessment Of ALOS PRISM Digital Elevation Model Extraction Over Japan. *The International Archives of the Photogrammetry* (pp. 1135-1138). Beijing: Remote Sensing and Spatial Information Sciences.

Deilami, K., & Hashim, M. (2011). Very High Resolution Optical Satellites for DEM. *European Journal of Scientific Research*, 542-554 .

Dolloff, J. T., & Theiss, H. J. (2014). The Specification And Validation Of Predicted Accuracy Capabilities For COmmercial Satellite Imagery. *ASPRS 2014 Annual Conference.* Louisville, Kentucky: ASPRS .

Indarto, & Prasetyo, D. R. (2014). Pembuatan Digital Elevation Model Resolusi 10m dari Peta RBI dan. *Jurnal Keteknikan Pertanian*, 55-63.

Kaveh, D., & Mazlan, H. (2011). Very High Resolution Optical Satellites for DEM. *European Journal of Scientific Research*, 542-554.

Naim, W. M., Abdullah, M. A., & Hashim, S. (2014). Evaluation of Vertical Accuracy of Digital Elevation Models Generated. *FIG Congress*, (pp. 1-17). Kuala Lumpur, Malaysia.

Perka BIG. (2018). *Peraturan BIG Nomor 6 Tahun 2018.* Retrieved from https://jdih.big.go.id/hukumjdih/27330968.

Rudianto, B. (2011). Analisis Pengaruh Sebaran Ground Control Point terhadap. *Jurnal Rekayasa Institut Teknologi Nasional*, 11-18.

SPATIAL AND TEMPORAL ANALYSIS OF LAND SURFACE TEMPERATURE CHANGE ON NEW BRITAIN ISLAND

Rafika Minati Devi[1]*, Tofan Agung Eka Prasetya[2, 3], Diah Indriani[1]

[1]Biostatistics and Demography Department, Public Health Faculty, Airlangga University, Campus C Mulyorejo, Surabaya, East Java, Indonesia

[2]Research Methodology, Mathematics and Computer Science Department, Science and Technology Faculty, Prince of Songkla University, Pattani Campus, Mueang Pattani, Pattani 94000, Thailand

[3]Health Department, Vocational Faculty, Airlangga University,

Jl, Dharmawangsa Dalam Selatan No 68, Airlangga, Gubeng, Surabaya, East Java, Indonesia

*e-mail: rafika.minati.devi-2016@fkm.unair.ac.id

Received: 18 May 2020; Revised: 22 June 2020; Approved: 23 June 2020

Abstract. Land Surface Temperature (LST) is a parameter to estimate the temperature of the Earth's surface and to detect climate change. Papua New Guinea is a tropical country with rainforests, the greatest proportion of which are located on the island of New Britain. Hectares of rainforests have been logged and deforested because of infrastructure construction. This study aims to investigate the change in land surface temperatures on the island from 2000 to 2019. The temperature data were taken from National Aeronautics and Space Administration (NASA) Terra satellites and were analysed using two statistical models: spatial and temporal. The spatial model used multivariate regression, while the temporal one used autoregression (AR). In this study, a cubic spline fitted curve was employed because this has the advantage of being smoother and providing good visuals. The results show that almost all the sub-regions of New Britain have experienced a significant increase in land surface temperature, with a Z value of 7.97 and a confidence interval (CI) of 0.264 – 0.437. The study only investigated land surface temperature change on New Britain Island using spatial and temporal analysis, so further analysis is needed which takes into account other variables such as vegetation and land cover, or which establishes correlations with other variables such as human health.

Keywords: *Land Surface Temperature, New Britain Island, Climate change, Cubic Spline*

1 INTRODUCTION

The systematic changes in the long-term state of the atmosphere which have been taking place for decades or longer is known as climate change (Public Health Institute, 2016). The statistical description of weather and the related conditions of oceans, land surfaces and ice sheets constitute climate in the broadest sense (Australian Academy of Science, 2015). Climate change is a complex problem that is occurring in around the world. It impacts on various sectors, such as agriculture, forestry, coastal ecosystems, human health, fisheries and water (Weatherdon, Magnan, Rogers, Sumaila, & Cheung, 2016). When it lowers water quality and quantity, for example, this will result in more water-borne and vector-borne disease. It will also increase the potential for crop failure because agriculture requires 90% of available water for irrigation purposes in many countries (Ahmed, Scholz, Al-Faraj, & Niaz, 2016).

Papua New Guinea (PNG) is a country with many tropical rainforests, which are mostly found on New Britain Island (Bryan & Shearman, 2015). PNG is prone to a variety of natural hazards,

http://dx.doi.org/10.30536/j.ijreses.2020.v17.a3342

such as cyclones, floods and droughts. Some of these are expected to increase in frequency, magnitude and intensity due to climate change (International Organization for Migration, 2015). An indicator used to predict climate change is Land Surface Temperature (LST). According to a study by Samanta (2009), high land surface temperatures have been found in Morobe Province on Papua New Guinea Island. Oyoshi, Akatsuka, Takeuchi, & Sobue (2014) state that the LST on the island of Papua New Guinea in 2007 was more stable than in Indonesia and Thailand, whereas Australia experienced temperature changes in a short period of time. One of the causes of significant LST changes is the sudden transformation of land use and land cover pattern as the result of rapid urban growth (Choudhury, Das, & Das, 2019).

LST data were obtained from thermal radiation emitted by MODIS (Moderate Resolution Imaging Spectroradiometer), which observes land surfaces at instant viewing angles (Wan & Li, 2010). MODIS is a NASA sensor aboard the Terra and Aqua satellites. Terra MODIS retrieves data at 10:30-12:00 a.m. and p.m. (daytime/nighttime) local time, while Aqua MODIS captures images from 01:00 to 03:00 a.m. and p.m. (daytime/nighttime) (Yang, Cai, & Yang, 2017). LST is a highly variable aspect of the Earth's surface, in both space and time. It analysed with the data spatially and temporally due to the fact that space is spatial and time is temporal (Luintel, Ma, Ma, Wang, & Subba, 2019).

In time series, the concept of autoregressive models refers to ones that are developed by regressing on previous values (Pal & Prakash, 2017). Many processes which are observed through time exhibit autocorrelation, which can be described by using the best autoregressive process (Paolella, 2019). The LST data correlated between time and space are analysed with multivariate regression. In such analysis, the relationships between independent and dependent variables are predicted in order to analyse the effects of the former on the latter (Mansouri, Feizi, Jafari Rad, & Arian, 2018). Land surface temperature is analysed using multivariate regression to examine each point based on latitude and longitude. The cubic spline model is compatible with this process because there is an assumption that seasonal patterns are the same every year, as well as the fact that changes in other parameters such as land cover change have a direct or indirect effect on consistently increasing or decreasing LST (Wongsai, Wongsai, & Huete, 2017). The best cubic spline model is determined by the location and point of the knot. In this study, the cubic spline used 0-knot, 4-knot, and 7-knot. The study aims to investigate LST changes on New Britain Island from 2000 to 2019 using autoregression (AR) and multivariate regression with a cubic spline.

2 MATERIALS AND METHODOLOGY

This study employs secondary data from the NASA MODIS (Moderate Resolution Imaging Spectroradiometer) website. The research focuses on the LST of New Britain Island from 2000 to 2019. A flowchart of the study data analysis is shown in Figure 2-1.

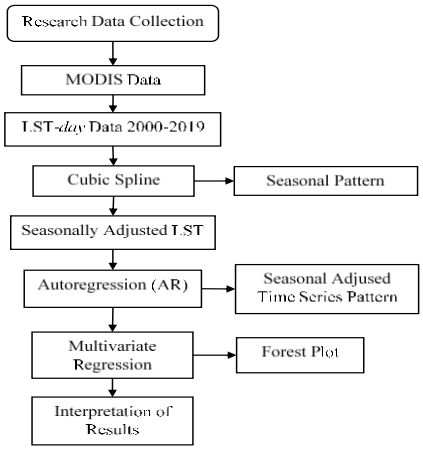

Figure 2-1: Data analysis flowchart

2.1 Location and Data

The study area was on New Britain Island, which is part of Papua New Guinea (PNG). The island was formed from volcanic activity, which makes it the most productive region for the development of geothermal energy resources in Papua New Guinea (PNG) (Lahan, Verave, & Irarue, 2015). Identification of geothermal resources can be made by using remote sensing with LST values (Tampubolon, Abdullah, San, & Yanti, 2016). Geographically, the island of New Britain is located from 148°17'56.20" E to 153° 7'31.50" E, and 6°17'55.88" S to 2°19'57.57" S. It is located to the east of the main island of Papua New Guinea and its size is around 36,520 km^2. It is the second largest island of Papua New Guinea. Its tropical climate is divided into humid and rainy seasons. The rainy season occurs from May to October, with the average peak of the rainy seasons occurs from July to September. Climate transition occurs in April and November.

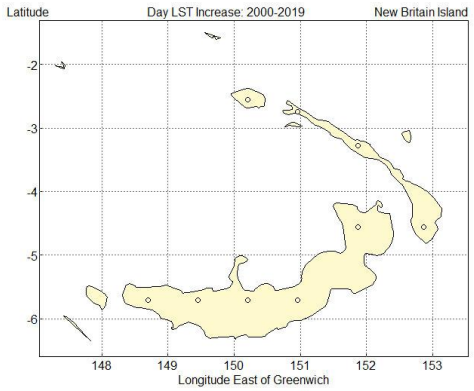

Figure 2-2: Map of New Britain Island with nine sub-region locations (circles) based on longitude and latitude.

Figure 2-2 shows the sample of LST data in relation to sub-regions; these data from the nine sub-regions are referred to as sampling points. Nine such regions were used as sample points to avoid spatial correlation. The sub-region samples were expected to be unbiased and able to represent the population of the whole islands. The island consists of nine sub-regions with point locations based on calculated longitude and latitude. Spatial correlations can occur between sub-regions and must be avoided; therefore, the data were collected minimum of 3 x 3 km^2 area, but the measurements were made with 7 x 7 km^2 area. The Terra satellites of NASA take pictures based on pixels. A pixel represents 1 x 1 km^2 and each sub-region comprises 49 pixels. In the time series, there were 907 observations of each sub-region (February 2000 to November 2019, which covered precisely 19 years of observational data.

2.2 Data Source

The New Britain Island LST data from 2000 to 2019 were obtained free of charge from satellite records. The data were recorded in the Earth Observing System Data and Information System (EOSDIS) and observed every 8 days. LST uses remote sensing technology to observe changes in temperature data. The data are managed by Oak Ridge National Laboratory (ORNL) and are available on the MODIS website.

MODIS is run by NASA, and provides Land Surface Temperature and Emissivity (LST&E) data. The LST data were obtained from the MODIS website https://modis.ornl.gov. The initial stage to obtain the data is to sign in using a personal account. The user then needs to determine the longitude and latitude of the point from which the data will be taken. These are available on Google Earth and can be calculated using tools on the MODLAND website https://landweb.modaps.eosdis.nasa.gov/cgi-bin/developer/tilemap.cgi to find vertical tiles, horizontal tiles, lines, and samples. The distance between sub-regions must be the same for the calculations based on lines and samples.

MODIS has many variables, each of which has a code for observation purposes. Land Surface Temperature and Emissivity (LST&E) have the code MOD11A2, this provides daytime LST data with observations every 8 days for 19 years. MODIS LST data are a geometrically-corrected product with special utility programs (Busygin & Garkusha, 2013). MODIS Terra data are produced with a generalised split-window LST algorithm that is used to minimise the influence of the atmosphere on surface temperature. The data from longitude and latitude points input by selecting the MOD11A2 code are sent via email in CSV format. Data analysis can be made using the point data. The spatial resolution of the LST data used for each region was a 1 km x 1 km grid (Sharma, Tongkumchum, & Ueranantasun, 2018).

2.3 Statistical Methods

2.3.1 Seasonal Pattern

The curve used to smooth periodicity was a spline. A cubic spline function is a piecewise cubic polynomial with continuous second derivatives and is smoothest among all the functions in the sense that it has a minimal integrated squared second derivative, so it is fitted using linear least squares regression (Me-Ead & McNeil, 2019). LST has the characteristics of seasonal patterns; in light of several considerations it was decided that the most appropriate model for use in the study was the cubic spline, with certain boundary conditions that ensured smooth periodicity and reduced the unbiased results in time series by outliers (Wongsai et al., 2017). Each grid in MODIS includes LST time-series data, so the cubic spline could be used for all the LST time-series in each grid (Sharma et al., 2018). The ability to handle any amount of missing data is one of the advantages of using the cubic spline function (Me-Ead & McNeil, 2019). Therefore, the model for the function (Wongsai et al., 2017) is:

$$s(t) = a + bt + \sum_{k=1}^{p} c_k[(t - t_k)_+^3 - d(t - t_{p-2})_+^3 + e(t - t_{p-1})_+^3 - f(t - t_p)_+^3] \quad (2\text{-}1)$$

For each sub-region, seasonal variability is believed to be constant, and the pattern shown by plotting the average response variable value for each sub-region every eight days at several years. Seasonal temperature patterns have been found by the use of the cubic spline function by selecting the right number of knots (Sharma et al., 2018). Such knots are based on the location and number, which must be chosen correctly because this is an important process. More knots would result in a smoother covariance surface, but more parameters would need to be estimated (Wongsai et al., 2017). This study used 0, 4, and 7 knots because these showed the highest r-squared value and the lowest p-value. The knots were represented by three curves, with 0 knot being linear, and 4 and 7 knots being the spline.

2.3.2 Time Series Correlation Models

There are two possible approaches to seasonal series: one is to decompose the series into a trend, a seasonal component and residual, and the other is to apply non-seasonal methods to the residual component (Venables & Ripley, 2002). Statistical tests related to the time series method include the autoregressive (AR) test. Analysis of autoregression can predict future values that may affect past values. Therefore, the AR model is the best for describing the value of the event. The autoregressive model is a stochastic model that is very useful to represent occurring series (Box, Jenkins, & Reinsel, 2015).

Autoregressive models are used to predict model curves according to the

correlation of the time series (Venables & Ripley, 2002). Autoregression can determine seasonal patterns because times series analysis has two goals: to identify the observation and to forecast future data. The effect of lagged values can cause problems such as autocorrelation. Many processes that are observed through time exhibit autocorrelation, or the tendency for the observation in the current time period to be related, or correlated, to previous observations, usually in the very recent past (Paolella, 2019). If in the first-order there is obvious autocorrelation, then it is likely that there will be autocorrelation in the second-order autoregression (Montgomery, Jennings, & Kulahci, 2015).

2.3.3 Adjusting for Spatial Correlation Models

The other statistical test is multivariate regression. Spatial analysis such as LST estimation in the sample region with nine sub-regions employed a multivariate regression model. Multivariate regression is a natural extension of multiple regression because both methods aim to explain possible linear relationships between certain input and output variables. Each output variable can be affected by exactly the same set of inputs (Izenman, 2013). Multivariate regression is performed using prescribed first-order autoregression, AR(1), a model for noise $\varepsilon(t)$ (Fyfe, Gillett, & Thompson, 2010). The estimation used in the model is the multivariate normal maximum likelihood and ordinary least squares (OLS). The equation of multivariate regression (Leufen & Schädler, 2019) is:

$$y_j = \sum_i \beta_{ij}.x_i + \epsilon_j \qquad (2\text{-}2)$$

For the spatial method, weighted least squares (WLS) was added to the statistical test, because such a regression method can be used when the OLS assumption of constant error variation is violated and is less sensitive to big changes in small parts of the observations (Wongsai et al., 2017).

Within the regression model used heteroscedasticity (non-variance) exists, so WLS can be used to resolve this (Kantar, 2016). In addition, WLS is used when the variance is non-constant (Tharmalingam & Vijayakumar, 2019). A multivariate regression model was developed to show the relationship between temperature and time over the 19 years, with a 95% confidence interval. For most linear regression, Z is considered to consist of entries following a normal distribution with zero mean (Zhang, Shi, Sun, & Cheng, 2017).

3 RESULTS AND DISCUSSION

Land Surface Temperature (LST) is a variable that can indicate climate change because it can affect the Earth's ecosystems, such as glaciers, ice sheets, and vegetation. Climate change is an alteration in climate patterns over a long period of time and may be due to a combination of natural and human causes (Australian Academy of Science, 2015). LST changes occur slowly over time because many other associated aspects also change, such us environmental or ecosystem conditions. Temperature variations were observed in nine sub-regions on New Britain Island during the period 2000 to 2019. To ascertain the temperature changes in each sub-region, LST observations were made every 8 days during the period 2000 to 2019 through the MODIS Terra satellite. The research is related to LST using spatially and temporally correlated data analysis and seasonal LST patterns

were analysed using a cubic spline (Wongsai et al., 2017).

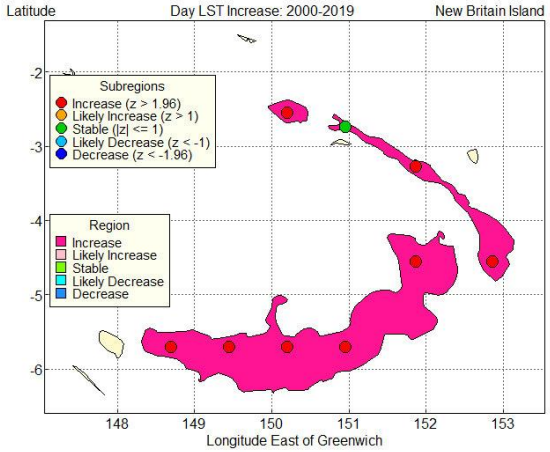

Figure 3-1: Spatial analysis of LST day changes on New Britain Island based on observations from 2000 to 2019

Figure 3-1 illustrates the LST changes in nine sub-regions (shown by circles) and one region on New Britain Island. Sub-region 1 is located in the top left-hand corner, while sub-region 9 is located in the bottom left-hand corner of the map. The location of the sub-regions is from top left to the right, and then from bottom right to the left. In the LST, there were increased temperatures in the regions between 2000 and 2019. The eight sub-regions which experienced an increase are indicated by a red circle, while the one which remained stable is indicated by a green circle. Specific results for each sub-region can be seen in the table 3-1. A red circle shows an increase in LST because the Z value is higher than 1.96, while the green circle represents stable LST because the Z value is lower than 1. There was not only an increase in land surface temperatures, but also in surface air and sea surface temperatures on Papua New Guinea Island. During the period 1950-2009, it is known that there were warming trends in surface air temperatures, whereas the sea surface temperature rose gradually since 1950 (CSIRO & Australian Bureau of Meteorology, 2011).

Table 3-1 shows that the LST-day increased from 2000 to 2019 in the sub-regions based on longitude and latitude. The region on New Britain Island experienced LST changes with a Z value of 7.97. The highest LST change was in sub-region 9, with a value of mean inc/dec of 0.56 ℃ and a p-value 0.003, while the lowest LST change was in sub-region 2, with a value of mean inc/dec of 0.118 ℃ and a p-value of 0.433. Sub-region 9 is located in the west of New Britain Province. Changes to warmer LST conditions are associated with rising concentrations of greenhouse gases and deforestation. It has been shown that the road construction planning that has occurred in the east and west of New Britain has put lowland forests at risk, meaning they will release substantial carbon into the atmosphere and set the stage for future emissions (Alamgir et al., 2019). Land use and land cover on New Britain Island is analysed in a study by Lamo et al. (2018).

Table 3-1: Mean of LST change in the nine sub-regions of New Britain Island

Sub-region	Longitude	Latitude	Mean Inc/Dec	P
1	150.203	-2.554	0.354℃	0.017
2	150.96	-2.746	0.118℃	0.433
3	151.877	-3.279	0.353℃	0.013
4	152.864	-4.563	0.414℃	0.02
5	151.877	-4.563	0.299℃	0.006
6	150.96	-5.704	0.323℃	0.046
7	150.203	-5.704	0.449℃	0
8	149.453	-5.704	0.339℃	0.003
9	148.699	-5.704	0.56℃	0.003

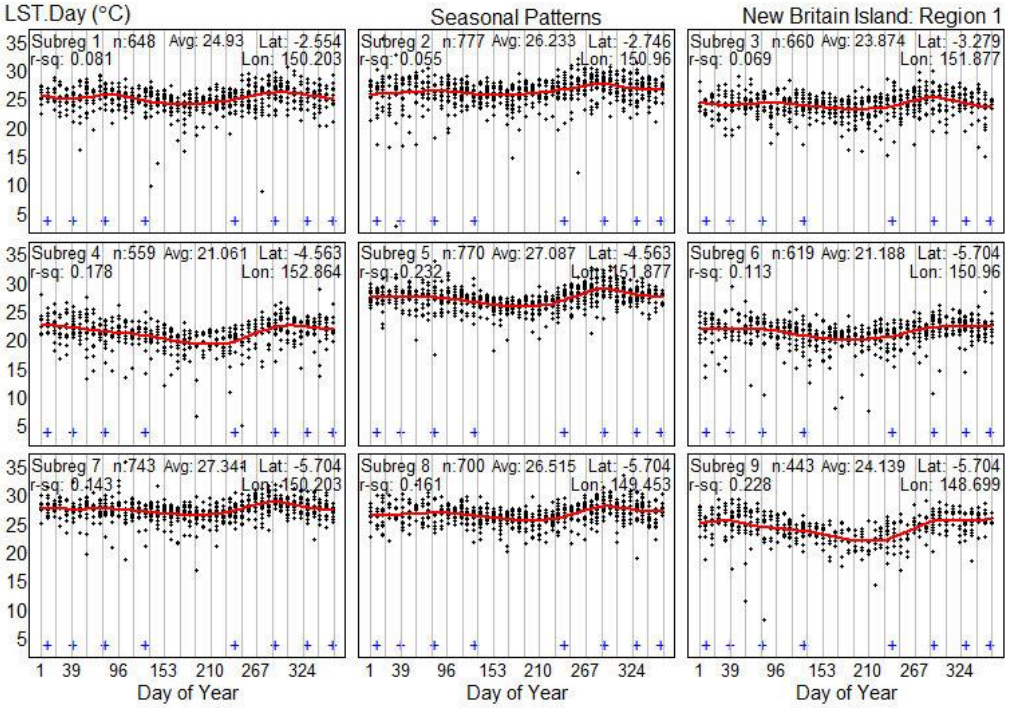

Figure 3-2: Seasonal pattern of Land Surface Temperature (LST) day with cubic spline function in the nine sub-regions of New Britain Island from day 1 to 365

Figure 3-2 represents the LST-day seasonal patterns in New Britain Island observed from 2000 to 2019. There were 19 points for each day as observations took place for 19 years. Each panel shows a sub-region, so there are nine panels with eight knots with a positive shape (+) on each panel. A smooth spline curve in the form of a red line is derived from the cubic spline model to produce an r-square of between 0.05 to 0.23. In sub-regions 1, 2, 3, 5, 7 and 8, there was an increase of LST in October to November (days 286-305). On the other hand, in sub-regions 4, 6, and 9 there was an increase from October to December (days 286-363), with stability at the end of the period. With regard to the seasonal pattern, there was also a decrease in LST on approximately days 172-210 because those days in June to July correspond to the rainy season. This season has a cooling effect on LST because the land is usually covered with vegetation (Khandelwal, Goyal, Kaul, & Mathew, 2018). This shows that seasonal patterns do not occur very often in the sub-regions of New Britain Island. The statistical results with R^2 ranged from 5% - 23%, with an average of around 10%.

Figure 3-3 shows the season-adjusted time series for LST-day on New Britain Island. Three kinds of spline curve were employed, consisting of knots 0, 4, and 7. The fitted models present the seasonal pattern curve in the nine sub-regions, with thick lines for 4-knot, thin lines for 7-knot, and dotted lines for 0-knot. Acceleration is shown from 4-knot, while the 7-year cycle is shown from 7-knot. In some of the sub-regions there are 7-year cycles. From the observations during the 19 years period, it can be seen that the LST of New Britain increased around by 0.12 ^{o}C - 0.56 ^{o}C, with the lowest CI value of 0.264 and the highest of 0.437. The CI (confidence interval) value was significant because the lower and upper values did not exceed 1.

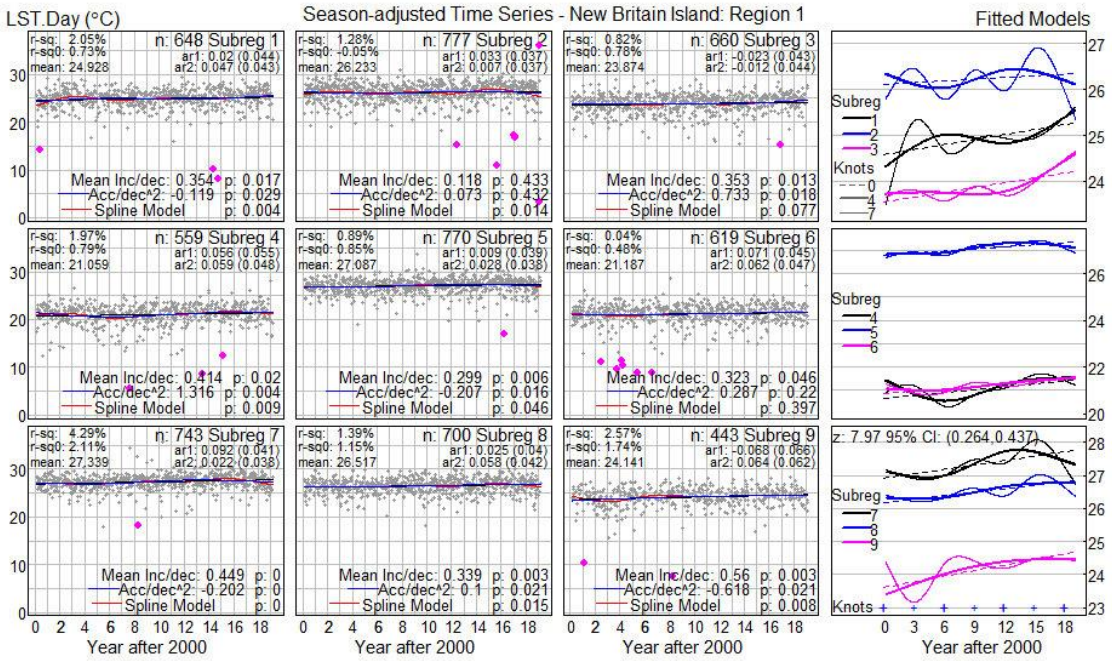

Figure 3-3: Season-adjusted time series of LST-Day in the nine sub-regions of New Britain Island for the period 2000-2019

In addition, Figure 3-3 shows a few outliers in the LST data, depicted by pink dots. These indicate that the LST observations took place when the sky was clear. In addition, sometimes the observations were not optimal because of heavy clouds in the rainy season. Autoregression was used to handle autocorrelation with a model of the p order. Autoregression was conducted in each sub-region in order 2, with observations for 19 years, so it can be called AR(2).

In the cubic spline function, it is given that the end of any year is followed by the beginning of the next year (Suwanwong & Kongchouy, 2016). Seasonal curves are the result of the function of the cubic spline, which produces temperature patterns and trends. The cubic spline function is excellent for observing the adjusted r-squared values for the assumption that the optimal knots and appropriate model (Wongsai et al., 2017). In this study, there were eight knots on different days. The change in LST occurred on the island of New Britain. The observations used a multivariate regression test with a cubic spline of 95% significance, assuming that in great measure of the sub-region in New Britain showed a significant increase in LST.

The Z value result indicates that pixels with high or low LST values are spatially clustered, even though they were measured to be statistically significant. In the case of a statistically significant positive Z value, as well as a greater Z value, they were included in the higher value cluster (hot spot), whereas the lower value cluster (cold spot) included those with a statistically significant negative Z value and a smaller Z value (Mavrakou, Polydoros, Cartalis, & Santamouris, 2018). In this study, the result of the Z value was positive, with a value of 7.97, meaning it is high.

The increase in LST on the island can be an indicator of climate change because it is part of frequent weather change (Ayuningtyas, 2015). LST changes because it is influenced by urbanisation land use and land cover change (such as forest degradation and deforestation) (Fu & Weng, 2016). The island of New Britain has a sizeable amount of rainforest, but it suffered the highest extent of

deforestation and logging from 2002 to 2014 (Bryan & Shearman, 2015). The location of the greatest deforestation is near sub-regions 5 and 7.

The greater levels of human activities which do not pay due care to the environment can cause global warming, especially because of the reduced areas of rainforest or green open space. Warming could occur on the island of New Britain because of increased LST. In addition, the increase in LST can be used as an indicator of heat islands, which are one of the causes of LST becoming warmer. Heat islands can impact on heatwaves, which affect the quality of life and the environment. LST is one of the climatic variables that can be an indicator of drought disasters; droughts can therefore be predicted from geographical conditions (Karnieli et al., 2010).

In the study of Korada, Sekac, Jana, & Pal (2018) related to drought in Papua New Guinea with reference to the LST and Normalized Difference Vegetation Index (NDVI), it was found that there was a risk zone, especially in the Western Highlands province. Based on that study, LST indicates drought from radiation levels. When radiation is high, there is little water content at the surface of the soil. Drought occurs because the temperature is too high, causing the water in the soil to evaporate. Drought can cause hunger and death because water is a source of life. If drought occurs, the community may not have sufficient food supplies because agriculture is experiencing crop failure.

4 CONCLUSION

The island of New Britain has many tropical rainforests, but it is also experiencing much logging and deforestation. This problem has an impact on climate change, which can result in natural disasters such as droughts. New Britain Island consists of one region with nine sub-regions, which comprised the observation area for the LST study. In eight of the nine sub-regions, LST had increased. The greatest change related to sub-region 9, with an average rise of 0.56°℃, while sub-region 2 experienced LST stability.

The method used for the temporal analysis was autoregression (AR). The 19 year time series showed that the increase in temperature was around 0.12℃ - 0.56℃. Therefore, the results clearly indicate that the Island of New Britain is becoming warmer. For the spatial analysis, the study used the multivariate regression method based on the spline curve. The cubic spline was used to observe seasonal patterns in LST-day. Spatial and temporal analyses are very suitable for observing patterns in Land Surface Temperature.

ACKNOWLEDGMENTS

This research could not have been realized without the invaluable help received. Therefore, I would like to thank Prof. Don McNeil for his direction and guidance while the researcher was at Prince of Songkla University, and all the lecturers at Airlangga University.

AUTHOR CONTRIBUTIONS

Spatial and Temporal Analysis Of Land Surface Temperature Change On New Britain Island. Lead Author: Rafika Minati Devi, Co-Author: Tofan Agung, Diah Indriani. Author contributions are as follows:

1. Rafika Minati Devi: collect data, analyse data and write manuscripts.
2. Tofan Agung: help command r software, help determine longitude and skyude/coordinate, help write manuscript.
3. Diah Indriani: help write manuscript.

REFERENCES

Ahmed, T., Scholz, M., Al-Faraj, F., & Niaz, W. (2016). Water-Related Impacts of Climate Change on Agriculture and Subsequently on Public Health: A Review for Generalists with Particular Reference to Pakistan. *International Journal of Environmental Research and Public Health*, *13*(1051), 1–16. https://doi.org/10.3390/ijerph13111051

Alamgir, M., Sloan, S., Campbell, M. J., Engert, J., Kiele, R., Porolak, G., … Laurance, W. F. (2019). Infrastructure Expansion Challenges Sustainable Development in Papua New Guinea. *PLOS ONE*, *14*(7), e0219408. https://doi.org/10.1371/journal.pone.0219408

Australian Academy of Science. (2015). *The Science of Climate Change: Questions and Answers*. Canberra.

Ayuningtyas, V. A. (2015). *Pengolahan Data Thermal (TIRS) Citra Satelit Landsat 8 untuk Temperatur Suhu Permukaan (Studi Lokasi : Kabupaten Banyuwangi) [Thermal Data Processing (TIRS) Landsat 8 Satellite Imagery for Surface Temperatures (Location Study: Banyuwangi Regency)]*. 1–8. Retrieved from http://eprints.itn.ac.id/1484/1/JURNAL1125008.pdf

Box, G. E. P., Jenkins, G. M., & Reinsel, G. C. (2015). *Time Series Analysis: Forecasting and Control* (5th ed.; D. J. Balding, N. A. C. Cressie, G. M. Fitzmaurice, G. H. Givens, H. Goldstein, G. Molenberghs, … S. Weisberg, eds.). New Jersey: John Wiley & Sons, Inc.

Bryan, J. E., & Shearman, P. L. (2015). *The State of the Forests of Papua New Guinea 2014: Measuring Change Over Period 2002-2014*. Port Moresby: University of Papua New Guinea.

Busygin, B., & Garkusha, I. (2013). Technology Mapping of Thermal Anomalies in the City of Dnipropetrovs'k, Ukraine, with Application of Multispectral Sensors. In G. Pivnyak, O. Beshta, & M. Alekseyev (Eds.), *Energy Efficiency Improvement of Geotechnical Systems: International Forum on Energy Efficiency* (pp. 151–160). Boca Raton: CRC Press.

Choudhury, D., Das, K., & Das, A. (2019). Assessment of Land Use Land Cover Changes and its Impact on Variations of Land Surface Temperature in Asansol-Durgapur Development Region. *Egyptian Journal of Remote Sensing and Space Science*, *22*(2), 203–218. https://doi.org/10.1016/j.ejrs.2018.05.004

CSIRO, & Australian Bureau of Meteorology. (2011). *Climate Change in the Pacific : Scientific Assessment and New Research. Volume 2 : Country Reports* (Vol. 2). https://doi.org/10.1108/S0732-1317(2011)0000020013

Fu, P., & Weng, Q. (2016). A Time Series Analysis of Urbanization Induced Land Use and Land Cover Change and its Impact on Land Surface Temperature with Landsat imagery. *Remote Sensing of Environment*, *175*, 205–214. https://doi.org/10.1016/j.rse.2015.12.040

Fyfe, J. C., Gillett, N. P., & Thompson, D. W. J. (2010). Comparing Variability and Trends in Observed and Modelled Global-Mean Surface Temperature. *Geophysical Research Letters*, *37*(16), 2–5. https://doi.org/10.1029/2010GL044255

International Organization for Migration. (2015). *Assessing The Evidence: Migration, Environment and Climate Change in Papua New Guinea*. https://doi.org/10.1163/ej.9789004163300.i-1081.143

Izenman, A. J. (2013). *Modern Multivariate Statistical Techniques* (2nd ed.; G. Casella, S. Fienberg, & I. Olkin, eds.). New York: Springer New York.

Kantar, Y. M. (2016). Estimating Variances in Weighted Least-Squares Estimation of Distributional Parameters. *Mathematical and Computational Applications*, *21*(2). https://doi.org/10.3390/mca21020007

Karnieli, A., Agam, N., Pinker, R. T., Anderson, M., Imhoff, M. L., Gutman, G. G., … Goldberg, A. (2010). Use of NDVI and Land Surface Temperature for Drought Assessment: Merits and Limitations. *Journal of Climate*, *23*(3), 618–633. https://doi.org/10.1175/2009JCLI2900.1

Khandelwal, S., Goyal, R., Kaul, N., & Mathew, A. (2018). Assessment of Land Surface Temperature Variation Due to Change in Elevation of Area Surrounding Jaipur, India. *The Egyptian Journal of Remote Sensing and Space Sciences*, *21*, 87–94. https://doi.org/10.1016/j.ejrs.2017.01.005

Korada, N., Sekac, T., Jana, S. K., & Pal, D. K. (2018). Delineating Drought Risk Areas Using Remote Sensing and Geographic Information Systems– A Case Study of Western Highlands Province, Papua New Guinea. *European Journal of Engineering Research and Science*, *3*(10), 103–110. https://doi.org/10.24018/ejers.2018.3.10.937

Lahan, M., Verave, R., & Irarue, P. (2015). A Preliminary Reconnaissance Geothermal Mapping in West New Britain Province , Papua New Guinea. *Proceedings World Geothermal Congress 2015*, 19–25.

Lamo, X. de, Arnell, A., Pollini, B., Salvaterra, T., Gosling, J., Ravilious, C., & Miles, L. (2018). *Using Spatial Analysis to Support REDD + Land-Use Planning in Papua New Guinea: Strengthening Benefits for Biodiversity , Ecosystem Services and Livelihoods*. Cambridge, UK: UNEP-WCMC.

Leufen, L. H., & Schädler, G. (2019). Calculating The Turbulent Fluxes in The Atmospheric Surface Layer with Neural Networks. *Geoscientific Model Development*, *12*(5), 2033–2047. https://doi.org/10.5194/gmd-12-2033-2019

Luintel, N., Ma, W., Ma, Y., Wang, B., & Subba, S. (2019). Spatial and temporal variation of daytime and nighttime MODIS land surface temperature across Nepal. *Atmospheric and Oceanic Science Letters*, *12*(5), 305–312. https://doi.org/10.1080/16742834.2019.1625701

Mansouri, E., Feizi, F., Jafari Rad, A., & Arian, M. (2018). Remote-Sensing Data Processing with the Multivariate Regression Analysis Method for Iron Mineral Resource Potential Mapping: A Case Study in the Sarvian Area, Central Iran. *Solid Earth*, *9*(2), 373–384. https://doi.org/10.5194/se-9-373-2018

Mavrakou, T., Polydoros, A., Cartalis, C., & Santamouris, M. (2018). Recognition of Thermal Hot and Cold Spots in Urban Areas in Support of Mitigation Plans to Counteract Overheating: Application for Athens. *Climate*, *6*(16), 1–12. https://doi.org/10.3390/cli6010016

Me-Ead, C., & McNeil, R. (2019). Pattern and Trend of Night Land Surface Temperature in Africa. *Scientific Reports*, *9*(1), 18302. https://doi.org/10.1038/s41598-019-54703-z

Montgomery, D. C., Jennings, C. L., & Kulahci, M. (2015). *Introduction to Time Series Analysis and Forecasting* (2nd ed.; D. J. Balding, N. A. C. Cressie, G. M. Fitzmaurice, G. H. Givens, H. Goldstein, G. Molenberghs, … S. Weisberg, eds.). New Jersey: John Wiley & Sons, Inc.

Oyoshi, K., Akatsuka, S., Takeuchi, W., & Sobue, S. (2014). Hourly LST Monitoring with the Japanese Geostationary Satellite MTSAT-1R over the Asia-Pacific Region. *Asian Journal of Geoinformatics*, *14*(3), 1–13.

Pal, A., & Prakash, P. (2017). *Practical Time Series Analysis*. Birmingham: Packt Publishing Ltd.

Paolella, M. S. (2019). *Linear Models and Time-Series Analysis: Regression, ANOVA, ARMA and GARCH* (1st ed., Vol. 52). Hoboken, NJ: John Wiley & Sons Inc.

Public Health Institute. (2016). Climate Change 101 : Climate Science Basics. In *Public Health Institute/ Center for Climate Change and Health* (pp. 1–10). Retrieved from

http://climatehealthconnect.org/wp-content/uploads/2016/09/Climate101.pdf

Samanta, S. (2009). Assessment of Surface Temperature Using Remote Sensing Technology. *Papua New Guinea Journal of Research, Science and Technology*, *1*, 12–18.

Sharma, I., Tongkumchum, P., & Ueranantasun, A. (2018). Modeling of Land Surface Temperatures to Determine Temperature Patterns and Detect their Association with Altitude in the Kathmandu Valley of Nepal. *Chiang Mai University Journal of Natural Sciences*, *17*(4), 275–288. https://doi.org/10.12982/CMUJNS.2018.0020

Suwanwong, A., & Kongchouy, N. (2016). Cubic Spline Regression Model and Gee for Land Surface Temperature Trend Using Modis in the Cloud Forest of Khao Nan National Park Southern Thailand During 2000-2015. *Journal of Engineering and Applied Sciences 11*, *11*, 2387–2395.

Tampubolon, T., Abdullah, K., San, L. H., & Yanti, J. (2016). The Identification of Geothermal with Geographic Information System and Remote Sensing in Distric of Dolok Marawa. *AIP Conference Proceedings*, *1712*, 030011-1-030011–030016. https://doi.org/10.1063/1.4941876

Tharmalingam, T., & Vijayakumar, V. (2019). Linear Kernel with Weighted Least Square Regression Co-efficient for SVM Based Tamil Writer Identification. *International Journal of Recent Technology and Engineering*, *8*(2), 586–591. https://doi.org/10.35940/ijrte.B1629.078219

Venables, W. N., & Ripley, B. D. (2002). *Modern Applied Statistics with S* (4th ed.). New York: Springer New York.

Wan, Z., & Li, Z.-L. (2010). MODIS Land Surface Temperature and Emissivity. In B. Ramachandran, C. O. Justice, & M. J. Abrams (Eds.), *Land Remote Sensing and Global Environmental Change* (pp. 563–577). https://doi.org/10.1007/978-1-4419-6749-7_25

Weatherdon, L. V., Magnan, A. K., Rogers, A. D., Sumaila, U. R., & Cheung, W. W. L. (2016). Observed and Projected Impacts of Climate Change on Marine Fisheries, Aquaculture, Coastal Tourism, and Human Health: An Update. *Frontiers in Marine Science*, *3*(48), 1–21. https://doi.org/10.3389/fmars.2016.00048

Wongsai, N., Wongsai, S., & Huete, A. R. (2017). Annual Seasonality Extraction Using the Cubic Spline Function and Decadal Trend in Temporal Daytime MODIS LST Data. *Remote Sensing*, *9*(12), 1–17. https://doi.org/10.3390/rs9121254

Yang, Y. Z., Cai, W. H., & Yang, J. (2017). Evaluation of MODIS Land Surface Temperature Data to Estimate Near-Surface Air Temperature in Northeast China. *Remote Sensing*, *9*(5), 1–19. https://doi.org/10.3390/rs9050410

Zhang, X., Shi, X., Sun, Y., & Cheng, L. (2017). Multivariate Regression with Gross Errors on Manifold-valued Data. *IEEE Transactions on Pattern Analysis and Machine Intelligence*, *41*(2), 444–458. https://doi.org/10.1109/TPAMI.2017.2776260

MAPPING BURNT AREAS USING THE SEMI-AUTOMATIC OBJECT-BASED IMAGE ANALYSIS METHOD

Hana Listi Fitriana[1,2]*, Suwarsono[2], Eko Kusratmoko[1], and Supriatna[1]
[1] Department of Geography, University of Indonesia
[2] Remote Sensing Application center, LAPAN
*e-mail: hanalisti@yahoo.com
Received: 28 December 2020; Revised: 26 June 2020; Approved: 29 June 2020

Abstract. Forest and land fires in Indonesia take place almost every year, particularly in the dry season and in Sumatra and Kalimantan. Such fires damage the ecosystem, and lower the quality of life of the community, especially in health, social and economic terms. To establish the location of forest and land fires, it is necessary to identify and analyse burnt areas. Information on these is necessary to determine the environmental damage caused, the impact on the environment, the carbon emissions produced, and the rehabilitation process needed. Identification methods of burnt land was made both visually and digitally by utilising satellite remote sensing data technology. Such data were chosen because they can identify objects quickly and precisely. Landsat 8 image data have many advantages: they can be easily obtained, the archives are long and they are visible to thermal wavelengths. By using a combination of visible, infrared and thermal channels through the semi-automatic object-based image analysis (OBIA) approach, the study aims to identify burnt areas in the geographical area of Indonesia. The research concludes that the semi-automatic OBIA approach based on the red, infrared and thermal spectral bands is a reliable and fast method for identifying burnt areas in regions of Sumatra and Kalimantan.

Keyword: *Burnt area, Landsat 8, OBIA*

1 INTRODUCTION

Forest and land fires occur every year in Indonesia, particularly in the dry season. They are a potential threat to sustainable development as they have a direct impact on ecosystems which contribute to increased carbon emissions and on biodiversity (Tacconi, 2003). The occurrence of forest fires in Indonesia also has an impact on regional issues in Southeast Asia, such as creating transportation barriers, especially air transportation ecosystem damage; and a decline in the quality of life of the community, for example in social, economic and health terms. To avoid repeated events, protection of forests from fires is needed by providing fire location data and information. According to Clark and Bobble (2007), the location of fires can be seen from burning areas by using remote sensing technology. Remote sensing is one method that can be used to map burnt areas relatively quickly, it can be done simultaneously, can reach large and remote areas, and it produces reliable accuracy (Cochrane, 2003). Information on burnt area is needed to determine the environmental damage caused, the impact on the environment, the carbon emissions generated, and the rehabilitation process needed. The abilities of remote sensing technology can provide a picture that matches an object on the Earth, so that through its temporal capabilities, it can perform monitoring that can provide information that is compatible with damage to forests in Indonesia.

http://dx.doi.org/10.30536/j.ijreses.2020.v17.a3281

Much research has been conducted on mapping areas using remote sensing data, ranging from the use of low-resolution to medium-resolution satellite imagery. Fuller and Fulk (2001) used NOAA-AVHRR and Landsat TM to map burnt areas in Kalimantan, while Giglio et al. (2009) mapped actively burning areas using MODIS sensors. Bastarrika et al. (2011) used Landsat images to map burnt areas in the European Mediterranean basin. In addition, Torralbo and Benito (2012) employed MODIS and Landsat to map such areas in Spain. Identification of burnt areas in Kalimantan has also been made by Suwarsono et al. (2013) using MODIS.

Various methods have been developed to map areas accurately. By using the difference method of Normalized Burn Ratio (dNBR), Cocke *et al.* (2005) mapped burnt areas from Landsat 7 ETM data. By applying commission errors, contextual hybrid algorithms and logistic regression, Bastarrika et al. (2011) mapped burnt areas in the European Mediterranean basin based on Landsat TM. Likewise, Suwarsono et al. (2013) identified burnt areas from MODIS, based on the vegetation index (NDVI) variable, the burnt index (NBR), and reflectance values. Liu et al. (2017) employed simple algorithms, Burned Area Extraction and Dating (BAED), extract burned parameters from Landsat images, and MODIS NDVI images.

A recent method that has been used in remote sensing is object-based classification. According to Darwish et al. (ND), the basic principle of this method is to utilise information related to form, texture, and context from images. According to Baatz et al. (2008), two steps in OBIA are segmentation and classification. The selection of objects based on image analysis (OBIA) uses image objects that have homogeneous pixels (Comert et al., 2019).

The purpose of this study is to develop remote sensing data models for detecting burnt areas by using the semi-automatic OBIA approach.

2 MATERIAL AND METHODOLOGY

2.1 Location and Data

The locations in this study were Riau, South Sumatra, South Kalimantan and West Kalimantan provinces. These were chosen because forest fires occur in these areas almost every year. The selected fire period was the peak fire season of 2015. This was a season with particularly severe fires in Indonesia because 2015 also coincided with an El Niño event. The data used in the study are Landsat 8 data from September 23, 2015 for Riau and South Sumatra, while for South Kalimantan the data are from September 13 and for West Kalimantan they are from September 9, 2015. The Landsat 8 image data are the result of direct acquisition from the LAPAN ground station.

2.2 Method

2.2.1 Image Processing

Changes in altitude, in satellite position, and rotation of the earth's surface movements when retrieving data and curvature of the earth will cause geometric distortion. It is therefore necessary to perform geometric correction so that the image coordinates are in accordance the with the geographic coordinates, and the position of the images matches others to produce images with certain projection systems (Purwadhi, 2001).

Table 1-1: Description of Landsat 8 Imagery

Characteristic	Description
Spatial Resolution	15m Panchromatic Operational Land Imager (OLI) 30m Multispectral OLI 30m Thermal Infrared Sensor (TIRS)
Temporal Resolution	Resembled 16 Days
Scene Size	170 km x 185 km
Bands	Coastal Aerosol 0.43-0.45 µm Blue 0.45 – 0.51 µm Green 0.53-0.59 µm Red 0.63 – 0.67 µm NIR 0.85 – 0.88 µm SWIR1 1.57 -1.65 µm SWIR2 2.11 – 2.29 µm Pan 0.50 – 0.68 µm Cirrus 1.36 – 1.38 µm TIRS1 10.60 – 11.19 µm TIRS2 11.50 – 12.51 µm

Source: earth observing system, 2019

Atmospheric interference factors will affect the reflectance value of an object, so radiometric correction is needed to increase the value of the original pixel, but ensuring that it does not become larger due to scattering or smaller due to absorption (Ji & Peters, 2007).

To establish the accuracy of the burnt areas, band combination was performed based on the usefulness of each band found on Landsat. Band 4 has a long electromagnetic wave spectrum range of 0.630 –0.680 µm, which functions to distinguish vegetation from the sloping part of the spectrum, which is very important for ecology because it reflects the health of the vegetation. In combination with other bands, there will be a vegetation index can be produce such as NDVI, which allows the measurement of plant health more precisely. Bands 6 and 7, with a short-wave infrared spectrum known as SWIR, are very useful for distinguishing wet soil from dry earth. Rock and soil that look similar in other bands often have a strong contrast in SWIR. Band 10 is an infrared thermal band, or TIR, which is used to observe heat on the surface of the Earth.

The aim of this study is to identify burnt areas by combining the health of vegetation, as the main component affected in fires, and the temperature of the soil, because the forest fire areas usually retain heat for several days. Several band combinations were made in the study. The first of these was of bands 4, 5, and 10, followed the combination of bands 5, 6 and 10, and then of bands 5, 7 and 10. Subsequently, after performing the band combination, the object-based image analysis (OBIA) semi-automatic approach was employed by using the free SAGA software (System for Automated Geoscientific Analyses) GIS. In determining the class of burning, interpretation was made by comparing areas based on high-resolution imagery and field data (Figure 2-1).

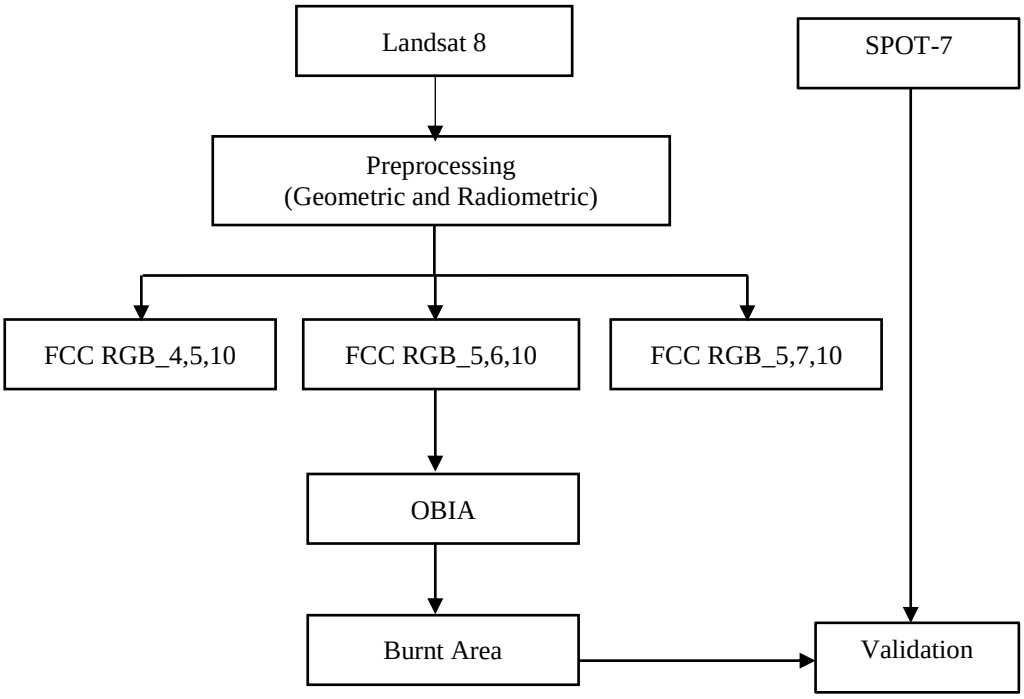

Figure 2-1: Research flow chart

3 RESULTS AND DISCUSSION

Object-based methods using Landsat 8 data can identify areas that have been burnt by land forest fires in Indonesia, especially the study area, which covers Riau province. In the future, it is the intention to also map South Sumatra, South Kalimantan and West Kalimantan. In the various combinations there were visual differences, namely in the combination of bands 4,5 and 10, bands 5,6,10 and bands 5,7,10. In Riau Province, as shown in Figure 3-1, the three combinations were able to identify the burnt areas, even though on the date in question it was cloudy and the burnt area was relatively small.

In South Sumatra, as shown in Figure 3-2, the wider area allowed clear identification of the active burning area, as well as of previously burnt areas. The difference in each band combination is clearly seen in the province of South Kalimantan, as shown in Figure 3-3, where the 4,5,10 combination showed burnt areas less clearly than the 5,6,10 5,7,10 and 6,5,4 combinations. This is probably caused by reflectance from the health of the vegetation itself, which cannot be captured by band red, while the nature of the SWIR band allows it to capture areas of drought on the Earth's surface. This is related to the burnt area that occurred in South Kalimantan Province one of them is caused by drought. This is different to the case of the province of West Kalimantan, as shown in Figure 3-4, where the burnt area is relatively small and there is still visible smoke.

This method is relatively quicker and does not require complex devices, such as those that are visually digitized or otherwise method, so that each stakeholder can do the mapping easily; the speed will also benefit them in making decisions.

In addition, because the method applied is only semi-automatic, it still requires interpretation from the researcher in determining training samples from the burnt areas, so this might cause minor errors. These could occur if the burnt area has the same characteristics as the open land. Further research therefore needs to be conducted

on how to distinguish burnt areas from forest fires on open land. It will be clearly seen pattern of difference burnt areas using band combination at the study site, this can be established by further calculations such as omission or commission error. Determination of the right band combination to be applied needs to be chosen wisely and carefully so that determination of the burned area is more accurate.

It is suggested that further research be conducted on the use of the semi-automatic OBIA method for areas with more specific geographical conditions, taking into account variations in vegetation, soil and topography. It may improve the accuracy.

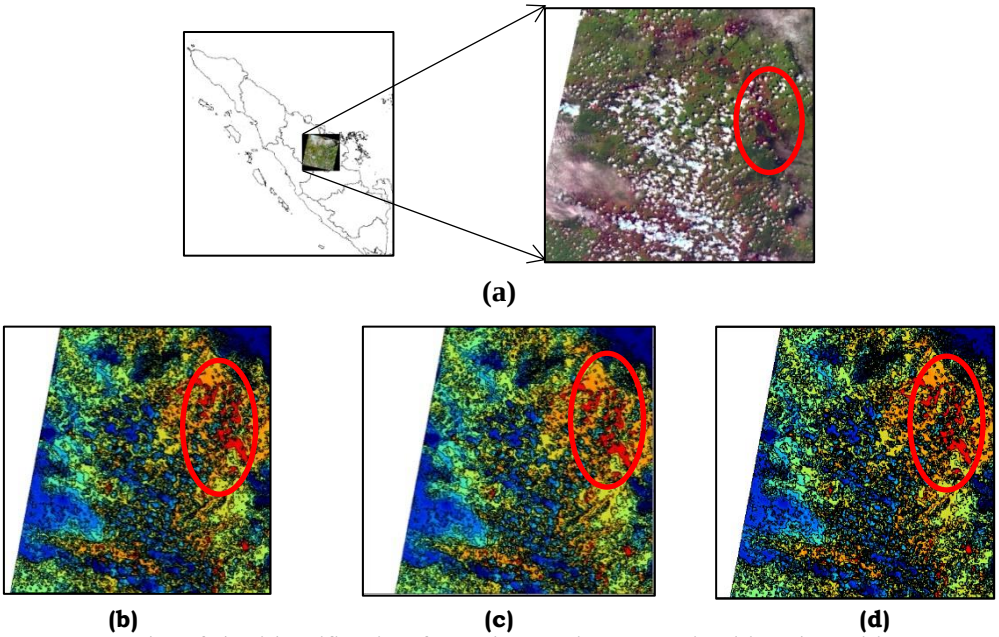

Figure 3-1: Results of the identification from the semi-automatic object-based image analysis of Landsat 8 images on 23 September 2015 for Riau Province, based on the: (a) RGB_6,5,4 band combination; (b) RGB_4,5,10 band combination; (c) RGB_5,6,10 band combination; and (d) RGB_5,7,10 band combination.

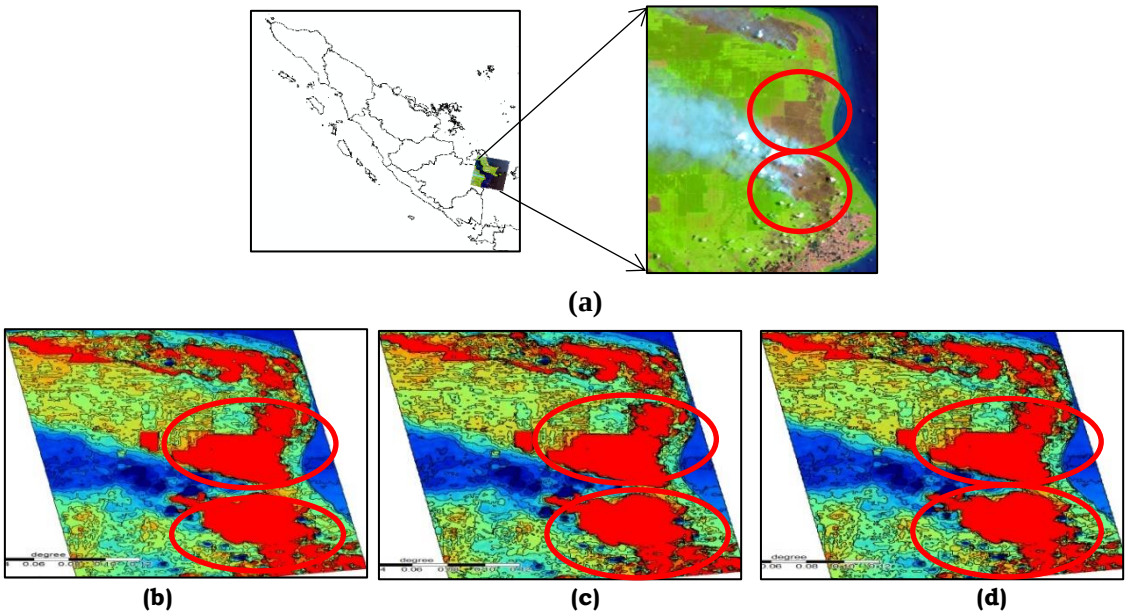

Figure 3-2: Results of the identification from the semi-automatic object-based image analysis of Landsat 8 images dated 23 September 2015 for South Sumatra Province, based on the: (a) RGB_6,5,4 band combination; (b) RGB_4,5,10 band combination; (c) RGB_5,6,10 band combination; and (d) RGB_5,7,10 band combination.

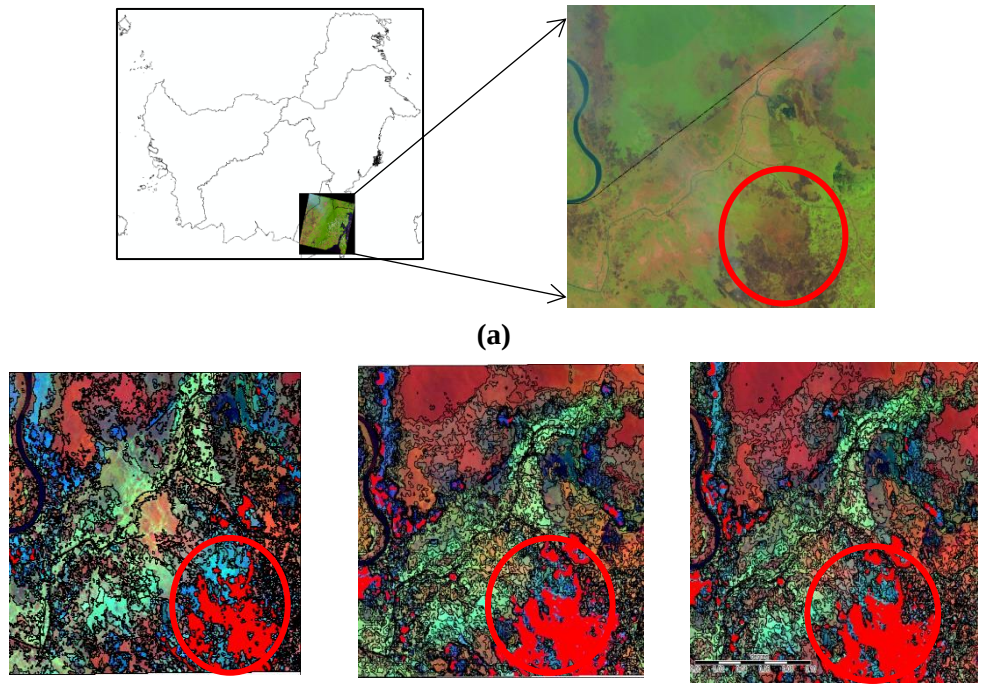

Figure 3-3: Results of the identification from the semi-automatic object-based image analysis of Landsat 8 images on 13 September 2015 for South Kalimantan Province, based on the (a) RGB_6,5,4 band combination; (b) RGB_4,5,10 band combination; (c) RGB_5,6,10 band combination; and (d) RGB_5,7,10 band combination.

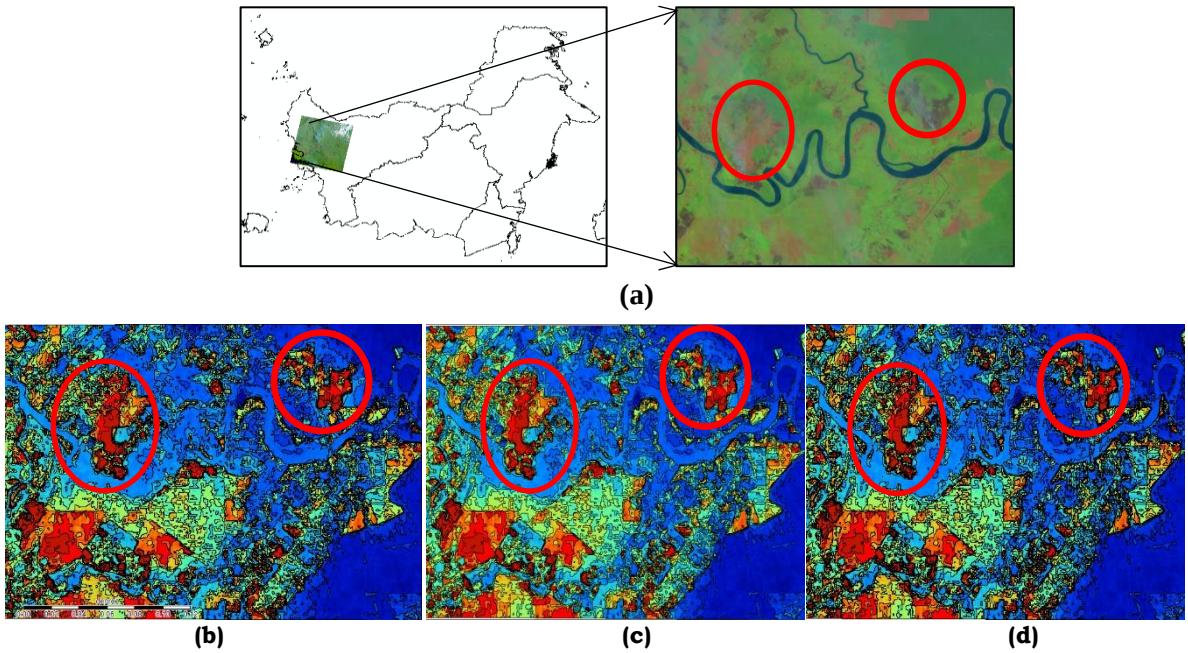

Figure 3-4: Results of the identification from thesemi-automatic object-based image analysis of Landsat 8 images dated 09 September 2015 for West Kalimantan Province, based on the: (a) RGB_6,5,4 band combination; (b) RGB_4,5,10 band combination; (c) RGB_5,6,10 band combination; and (d) band combination RGB_5,7,10.

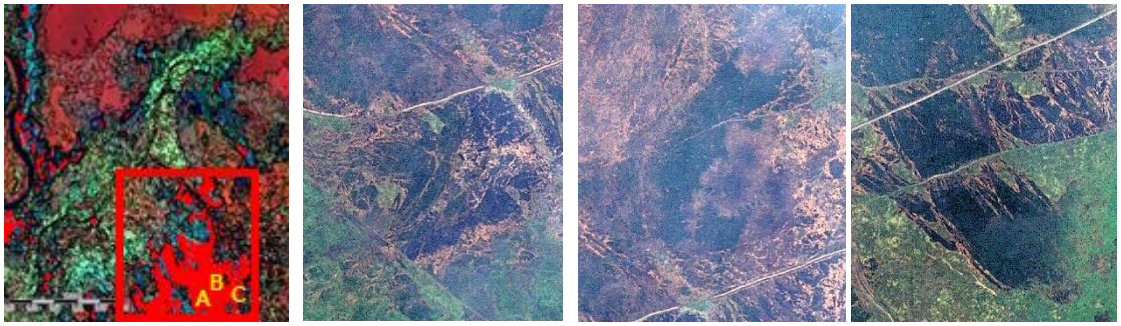

Figure 3-5: Comparison image between burnt areas detected from semi-automatic OBIA Landsat 8 identification and visualization burnt area from SPOT-7, locations A, B and C.

Comparison with high-resolution images

A SPOT-7 image dated 23 September 2015 was available for part of South Kalimantan. The image was composed of RGB true colour, whereas in it, the burnt area looks black or blackish brown. The data were used to visually compare a burnt area detected from semi-automatic OBIA identification and from SPOT-7 (see Fig. 3-5). From the results of the visual comparison, it can be seen that the burnt area detected by the semi-automatic OBIA method was the same as that seen from SPOT-7.

Although this method has been tested to be more effective and quicker, this study chose locations based on the fact that they often experience fires, namely Riau, South Sumatra, West Kalimantan and South Kalimantan. More specific geographical conditions, such as vegetation, soil, and topography, were not considered.

4 CONCLUSION

It is concluded that the semi-automatic object-based image analysis based on red, infrared and thermal spectral bands is a reliable and fast method for identifying burnt areas in regions of Sumatra and Kalimantan. It is suggested that further research be conducted on the use of the semi-automatic OBIA method for areas with more specific geographical conditions, taking into account variations in vegetation, soil and topography.

However, this study has the disadvantage of only focusing on one date in one area; further research should cover different times in one area and also apply these to other areas. In addition, research should focus on relatively small burning areas, as forest fires in Indonesia cover relatively small areas but are spread over several points.

ACKNOWLEDGMENTS

This research was supported by the Australia Award Indonesia in the Integrated Fire Management Program 2017 and supported by SAINTEK Kemenristekdikti 2018. The author would like to thank the Head of the Remote Sensing Application Center LAPAN, Dr. M. Rokhis Khomarudin, who provided support for the research. Thanks also to Dr. Sarah Hobgen and Dr. Rohan Fisher for discussion and advice. The research was presented at a seminar at ICOSAG on August 24, 2019, organized by the Department of Geography, University of Indonesia.

AUTHOR CONTRIBUTIONS

Mapping Burnt Areas Using The Semi-Automatic Object-Based Image Analysis Method. Lead Author: Hana Listi Fitriana and Suwarsono, Co-Author: Eko Kusratmoko and Supriatna.

REFERENCES

Baatz, M., Hoffmann, C., & Willhauck, G. (2008). Progressing from object-based to object-oriented image analysis. In: T. Blaschke, S. Lang & G.J. Hay (Eds), *Object-Based Image Analysis. Lecture Notes in Geoinformation and Cartography*. Berlin: Springer. 29-44.

Bastarrika, A., Chuvieco, E., & Martín, M.P. (2011). Remote Sensing of Environment Mapping burned areas from Landsat TM / ETM + data with a two-phase algorithm: Balancing omission and commission errors. *Remote Sensing of Environment, 115*(4), 1003–1012. https://doi.org/ 10.1016/j.rse.2010.12.005.

Clark, J. & Bobble, T. (2007). Using Remote Sensing to Map and Monitor Fire Damage in Forest Ecosystem. In: M.A. Wulder & S.E. Franklin (Eds), *Understanding Forest Disturbance and Spatial Pattern: Remote Sensing and GIS Approaches*. New York: Taylor & Francis.

Cochrane. M.A. (2003). Fire Science for Rainforests, *Nature, 421*, 913-919.

Cocke, A.E., Fulé, P.Z., & Crouse, J.E. (2005). Comparison of burn severity assessments using Differenced Normalized Burn Ratio and ground data, *International Journal of Wildland Fire,14*, 189–198.

Comert, R., Matci, D.K., & Avdan, U. (2019). Object Based Burned Area Mapping With Random Forest, *International Journal of Engineering and Geosciences (IJEG), 4*(2), 078-087.

Darwish, A., Leukert, K., & Reinhardt, W. (n.d). Image Segmentation for the Purpose of Object Based Classification, GIS Lab (AGIS), University of the Bundeswehr Munich, Neubiberg, Germany.

Fuller, D.O., & Fulk, M. (2001). Burned area in Kalimantan, Indonesia mapped with NOAA-AVHRR and Landsat TM Imagery, *International Journal of Remote Sensing, 22*(4), 691–697.

Giglio, L., Loboda, T., Roy, D.P., Quayle, B., & Justice, C.O. (2009). Remote Sensing of Environment An active- fire based burned area mapping algorithm for the MODIS sensor. *Remote Sensing of Environment, 113*(2), 408–420. https://doi.org/ 10.1016/j.rse.2008.10.006

Ji, L., & Peters, A.J. (2007). Performance Evaluation of Spectral Vegetation Indices Using a Statistical Sensitivity Function. *Remote Sensing of Environment, 106*, 59-65.

Liu, Z., Yang, J., & Dwomoh, F. (2016). Mapping recent burned patches in Siberian larch forest using Landsat and MODIS, *European Journal of Remote Sensing, 49*(1), 861-887, DOI: 10.5721/ EuJRS20164945

Purwadhi, Sri Hardiyanti. (2001). Interpretasi Citra Digital. PT. Gramedia Widiasarana Indonesia. Jakarta.

Suwarsono, Rokhmatullah, & Waryono, T. (2013). Pengembangan Model Identifikasi daerah Bekas Kebakaran hutan dan Lahan (Burned Area) menggunakan Citra Modis di Kalimantan (Model Development of Burned Area Identification Using Modis Imagery in Kalimantan). *Jurnal Penginderaan Jauh 10*(2), 93-112.

Tacconi, L. (2003). Fires in Indonesia: Causes, Costs, and Policy Implications. CIFOR Occasional Paper No.38. Bogor.

Torralbo, A.F., & Benito, P.M. (2012). Landsat and MODIS Images for Burned Areas Mapping in Galicia, Spain. Master's of Science Thesis in Geoinformatics TRITA-GIT EX 12-006. School of Architecture and the Built Environment Royal Institute of Technology. Stockholm, Sweden.

AN ENHANCEMENT TO QUANTITATIVE PRECIPITATION ESTIMATION USING RADAR-GAUGE MERGING (CASE STUDY: EAST JAVA)

Abdullah Ali[1]*, Gumilang Deranadyan, Iddam Hairuly Umam
[1]Remote Sensing Data Management Division, Center for Public Weather Service, Indonesia Agency for Meteorology Climatology and Geophysics (BMKG)
*e-mail: alibinakhsan@gmail.com
Received: 11 March 2020; Revised: 22 June 2020; Approved: 24 July 2020

Abstract. Quantitative precipitation estimation (QPE) provides valuable information for hydrology purposes. Its dense spatial and temporal resolution can be combined with surface observations to enhance the accuracy of estimations. This paper presents an enhancement to QPE achieved by adjusting estimation drawn from the Indonesian Agency for Meteorology, Climatology, and Geophysics (BMKG) weather radar network at Surabaya, to real-data observations from 58 rain gauges. The Mean Field Bias (MFB) method is used to determine the correction factor through the difference between radar estimations and rain-gauge observation values. The correction factor obtained at each gauge points is interpolated to the entire radar grid in a multiplicative adjustment. Radar–gauge merging results in a significant improvement, revealed by the decreasing of mean absolute error (MAE) and false alarm ratio (FAR) by about 40% as well as increasing the possibility of detection (POD) by more than 50% in all rain categories (light rain, moderate rain, heavy rain and very heavy rain). This performance improvement is likely to provide significant benefits for operational use by BMKG and other hydrological information users.

Keywords: *quantitative precipitation estimation, radar–gauge merging, mean field bias method*

1 INTRODUCTION

The need for rainfall accumulation estimation tools with high-level spatial resolution is growing along with the increasing application of hydrological and weather forecast models. These tools are used widely in water resource analysis, flood forecasting and warnings over sparsely gauged catchments (e.g. Aghakouchak, Habib, & Bardossy, 2010; Zhu, Xuan, & Cluckie, 2014). Accurate accumulation values at tight resolution levels will significantly impact on the performance of these models.

As observation instruments measuring the backscattered power from hydrometeorology particles at particular heights, weather radar can provide estimated values of precipitation at surface levels. Even though such radar have high spatial and temporal resolution, there are still many sources of error that can affect the accuracy of the rainfall estimation values they produce. Sources of error include variation in Z-R relationship, errors in estimating radar reflectivity factor (Wu Hsu, Lien, & Chang, 2015; Wu et al., 2015), difference in radar–gauge sampling (Wilson & Brandes, 1979), natural variability of drop-size distribution, and instrument errors (Joss & Wadvogel, 1990).

The reflectivity observations of radar itself can experience several errors, such as calibration errors, radio emitter interferences and contamination from

http://dx.doi.org/10.30536/j.ijreses.2020.v17.a3316

non-meteorological echo, as well as the effect of distance attenuation or increased sampling volume due to beam broadening (Goudenhoofdt & Delobbe, 2009). Uncertainty increases when the estimated rainfall process is being carried out on the surface, resulting from non-uniform vertical reflectivity profile (VPR) and the Z-R relationship. These sources of uncertainty can be minimized by utilizing point data from surface rain-gauge observations, as these have a higher degree of accuracy. Extensive spatial observation range data from radar and accurate point observation data from rain gauges can be combined to enhance the value of estimations.

Radargauge merging has been carried out since the beginning of weather radar operations in the 1970s, and many complex methods have been applied to merge radar and rain-gauge data, including co-kriging (Krajewski, 1987; Sun et al., 2000), objective statistical analysis methods (Pereira Fo, Crawford, & Hartzell, 1998) and Kalman filtering approach (Todini, 2001; Seo & Breidenbach, 2002; Chumchean, Sharma, & Seed, 2006). Before the merging is executed, quality control of the radar data must be carried out, such as elimination of ground clutter, attenuation correction and VPR correction (e.g. Germann, Galli, Boscacci, & Bolliger, 2006; Tabary, 2007; Uijlenhoet & Berne, 2008), because adjustments to uncorrected radar data do not produce significant corrections to QPE. Rain-gauge density is also very influential on the adjustment process, as tested by Sokol (2003) and Chumchean et al. (2006).

The objective of this research is to enhance the accuracy of QPE obtained from weather radar by merging it to surface observations (rain-gauge data) that represent more accurate accumulation values. The final result of this study is expected to be that radar–gaugemerged QPE has better accuracy than radar-only QPE.

2 MATERIALS AND METHODOLOGY

In this study, C-Band single polarimetric radar manufactured by Gematronik Radar with maximum range of 240 km, 250m spatial resolution and nine elevation angles is used (Figure 2-1).

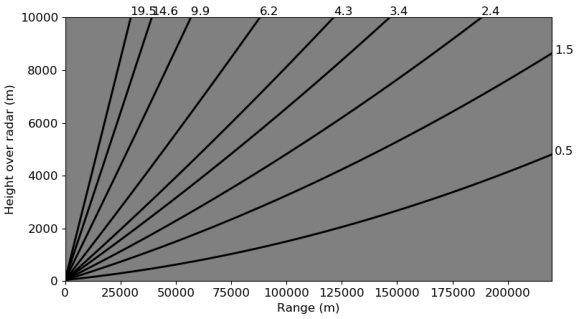

Figure 2-1: Surabaya radar scan strategy

Table 2-1: Radar hardware specification

Parameter	Value
Radar site name	Surabaya
Latitude	-7.41028° S
Longitude	112.76056° E
Altitude	3 m
Tower height	23 m
Frequency	5640 H
Beam width	<1°
Pulse width	0.5–2.0 µs
PRF min	250 Hz
PRF max	1200 Hz
Signal processor	GDRX-SP
Transmitter type	Coaxial magnetron
Polarization	Single
Installation year	2006
Manufacturer	Selex SI Gematronik Radar
Z-R relationship	200 $R^{1.6}$

Radar hardware specification is shown in Table 2-1. The topography around the radar site is variable and contains six volcanoes: Mt. Arjuna, Mt. Kawi, Mt. Bromo, Mt. Ngliman and Mt. Roar. The beam-blockage analysis based on digital elevation data from the SRTM static model is shown in Figure 2-2. The most significant blocking is in the southerly direction, derived from Mt. Arjuna, Mt. Kawi and Mt. Bromo.

2.1 Location and Data

The study area comprises 250 km around Surabaya. The weather radar used covers all of the East Java region, except those areas that are blocked by terrain. Rain-gauge distribution overlaid with beam-blockage analysis at the two lowest elevations is shown in Figure 2-3. There are 145 rain gauges in East Java province that are covered by the radar's maximum observation range, but 34 of these are blocked at 0.5° elevation, and 10 are blocked at 1.5° elevation angle.

Raw data obtained by the Surabaya weather radar with Rainbow5 format is used and calculated to hourly QPE and rewritten to NetCDF format. Full hourly QPE data for the day is then calculated to create the one-day QPE to be adjusted.

In the adjustment process, the rain gauges used are only those that operate for 24 hours, with those that do not cover the full 24-hour period because of instrumentation problems or data-feed issues being excluded.

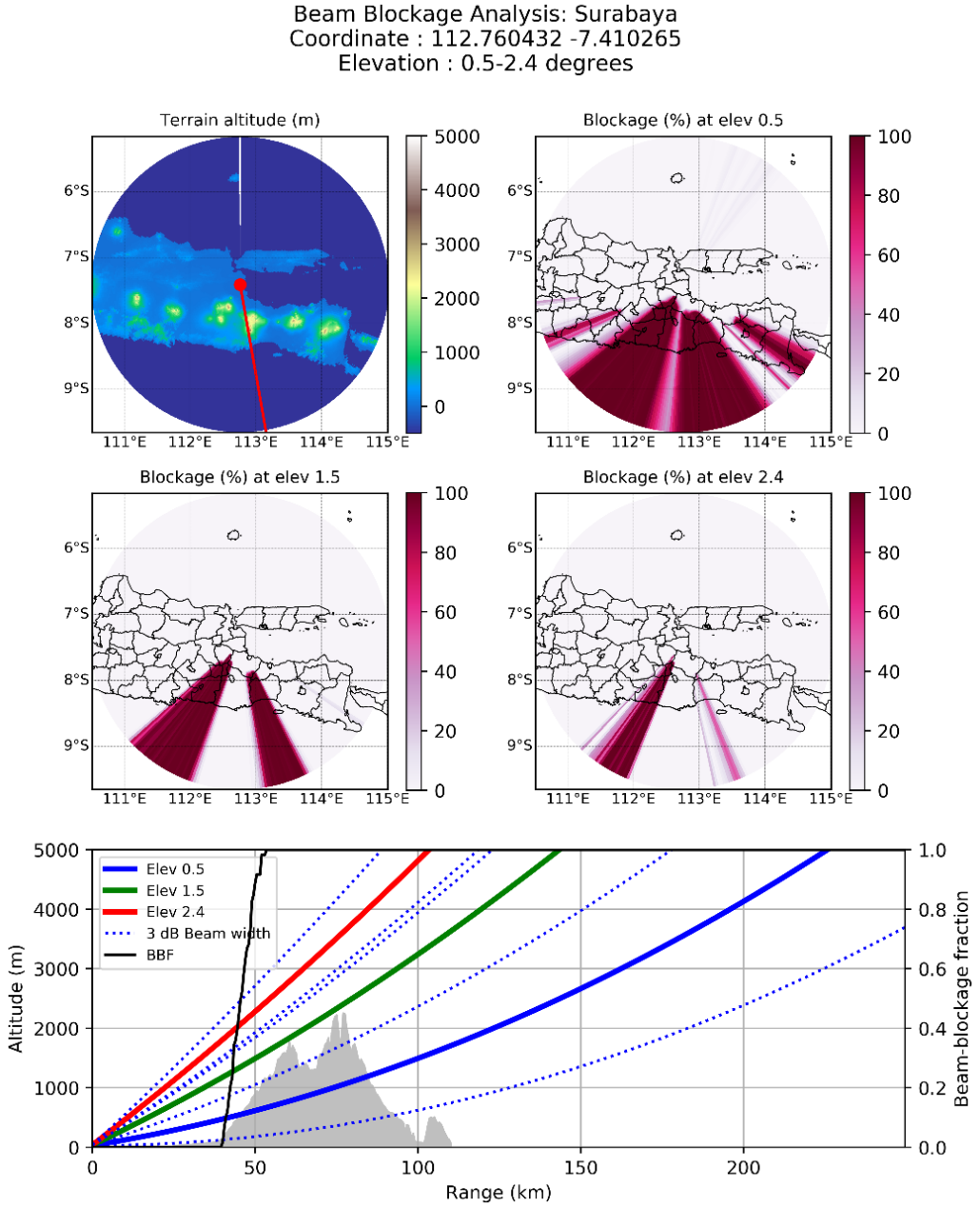

Figure 2-2: Beam-blockage analysis at Surabaya radar.

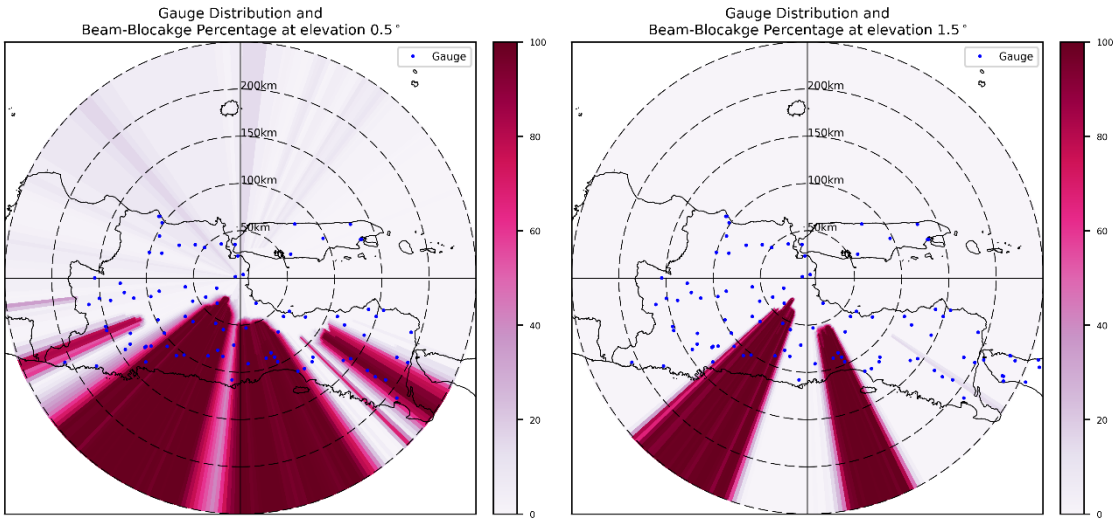

Figure 2-3: Rain-gauge distribution and blockage percentage

Because of the very significant effect of distance on precipitation estimation, this study only uses rain gauges at a distance of up to 150 km from the weather radar. In total, 58 rain gauges were used, and the case studies used are for events detected by weather radar on 17 and 19 March 2019.

2.3 Methods

Several methods have been developed to adjust radar data with rain-gauge data. In this paper, the mean field bias (MFB) method is used. It is important to note the amount of radar data sampling that will be merged with rain-gauge data (Villarini, Mandapaka, Krajewski, & Moore, 2008). In the study by Goudenhoofdt and Delobbe (2009), 9-pixel radar data from around the rain-gauge network was used to represent the value of rainfall accumulation at the corresponding rain-gauge points, and this is the method followed in this study. The use of 9 pixels for the corresponding raingauges can minimize the effect of wind gusts on droplets (Lack & Fox, 2007). The accumulated value used must be more than 1mm both for radar and rain gauges (Goudenhoofdt & Delobbe, 2009).

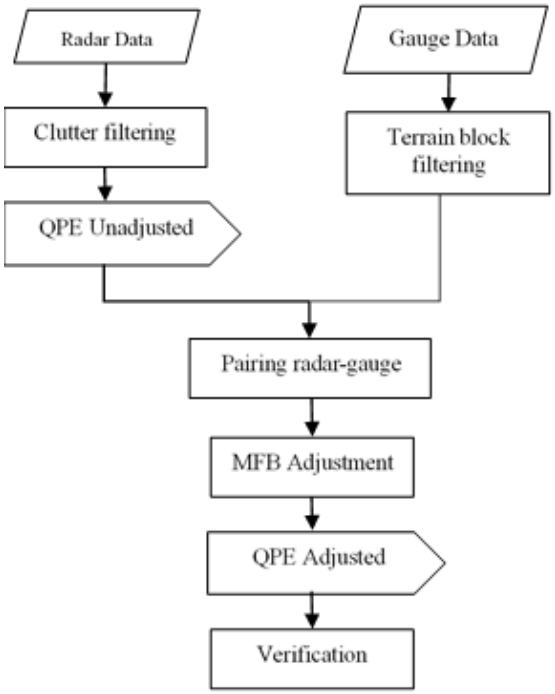

Figure 2-4: Research flowchart

The conversion of reflectivity into rainfall uses the Marshall Palmer Z-R relationship (Equation 2-2) with the input of maximum reflectivity values (Nova, 2017).

$$Z = \int_0^\infty N(D)\, D^6 dD \qquad (2\text{-}1)$$

$$Z = 200\, R^{1.6} \qquad (2\text{-}2)$$

With Z measured in mm^6/m^3 and R in mm/h. The calculation of hourly QPE is performed using Equation 2-2 (Selex SI, 2017).

Equation 2-3 is used to calculate the QPE from rain intensity obtained from Equation 2-2.

$$A_i = (t_i - t_{i-1}).\frac{R_i + R_{i-1}}{2} \quad (2\text{-}3)$$

Where A_i is the accumulation of rain of the i^{th} steps, ($t_i - t_{i-1}$) is the time step (time difference between two consecutive data in hours), and ($R_i + R_{i-1}$) is the accumulation of consecutive data. In one hour, there are six data, since the time difference between consecutive data is 10 minutes. After an hourly accumulation of radar QPE and rain-gauge data are obtained, adjustment is carried out using MFB, with the assumption that radar estimates are affected by a uniform multiplicative error that can result from bad electronic calibration or an erroneous coefficient in the Z-R relationship.

The MFB adjustment factor can be formulated as Equation 2-4:

$$C_{MFB} = \frac{\sum_{i=1}^{N} G_i}{\sum_{i=1}^{N} R_i} \quad (2\text{-}4)$$

Where N is the number of radar–gauge pairs, and Gi and Ri are the rainfall values detected by the gauge and radar.

One-hour adjusted QPE is then accumulated for one day and verification is then performed on that one-day data. Verification begins with plotting a correlation graph between the accumulation of radar and rain-gauge data. The quality of the adjustment is measured through the parameter of root mean squares error (RMSE) and mean absolute error (MAE), as shown in Equations 2-5 and 2-6.

$$RMSE = \sqrt{\frac{\sum_{i=1}^{N}(R_i - G_i)^2}{N}} \quad (2\text{-}5)$$

$$MAE = \frac{\sum_{i=1}^{N}|R_i - G_i|}{N} \quad (2\text{-}6)$$

Contingency table verification is also performed to obtain the possibility of detection (POD), false alarm ratio (FAR), and proportion correct (PC) values for the specified rainfall accumulation category. The accumulation categories refer to the classifications used by BMKG slight rain = 5–20 mm/day; moderate rain = 20–50 mm/day; heavy rain = 50–100 mm/day; and very heavy rain = more than 100 mm/day. The contingency table is presented in Table 2-2, while Equations 2-7, 2-8 and 2-9 show the POD, FAR and PC calculations, respectively. The complete research flowchart is presented in Figure 2-4.

Table 2-2: Contingency table for radar–gauge adjustment

Radar	**Gauge**	
	Yes	No
Yes	Hit (H)	False (F)
No	Miss (M)	Correct negative (N)

$$POD = \frac{H}{H + M} \quad (2\text{-}7)$$

$$FAR = \frac{F}{H + F} \quad (2\text{-}8)$$

$$PC = \frac{H + N}{H + M + F + N} \quad (2\text{-}9)$$

3 RESULTS AND DISCUSSION

Several quality controls were applied to the radar data through the pre- and post-processing tools contained in the Gematronik Radar system, including speckle removal, ground-clutter removal and attenuation correction. Radar data that remains exposed to significant non-meteorological echoes will result in very overestimated QPE, and in such situations, adjustment by gauge itself will have no significant

effect. Figure 3-1 presents the results of unadjusted and adjusted one-hour QPE for the first case study on 17 March 2019 at 11 UTC, at which time the most significant rainfall occurred. The calculation of one-day QPE is carried out after the adjustment is performed for each hour's QPE.

The MFB method does not account for distance as the weighting value to the correction factor, so it will be taken across the entire grid. There is an increasing rainfall accumulation after the adjustment. This increment is adjusted to the hourly gauge accumulation observed. Scatter plot verification at all gauges used (Figure 3-2) shows that radar data without adjustment (raw data) has an underestimated rainfall accumulation, indicated by its fit slope (blue line) being to the right (under) the centre line. This underestimated value is mostly probably caused by an error in Z-R relationship and the absence of differentiation estimation between convective and stratiform rain. After the adjustment is performed, the adjusted-fit slope (red line) shows very significant improvement it approaches the centre line meaning that the estimation is near perfect, though it is still slightly underestimated from the observed accumulation value.

The scale of error value can determine how far the adjustment improves the raw data. After the adjustment for all hours in one day, MAE, ME and RMSE are calculated. For the first case-study day (17 March 2018), the values of MAE, ME and RMSE for the radar data without adjustment are 22.76, 5.20 and 4.49 mm, respectively. After MFB adjustment these values become 13.15, 4.40 and 2.61 mm. Similarly to the first case, the second case (19 March 2019) also shows decreasing error, with MAE, ME and RMSE of 34.14, -23.22 and 8.32 mm, respectively, before adjustment and 13.06, -5.90, and 5.0 after adjustment.

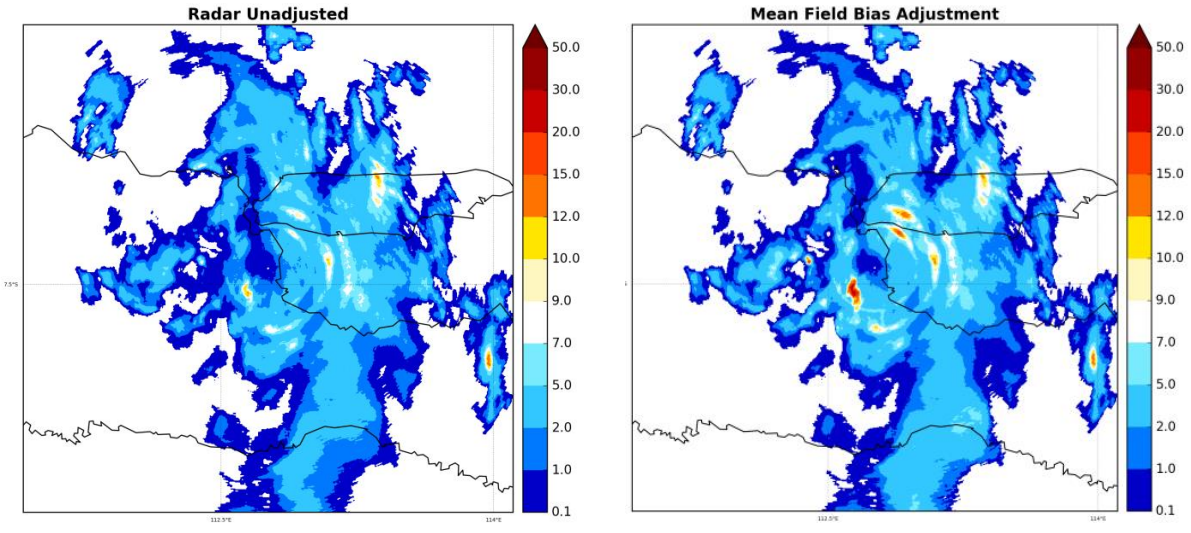

(a) (b)

Figure 3-1: The spatial results of the gauge adjustment at 17 March 2019 11 UTC, when the rain distribution is the most significant: (a) one-hour QPE unadjusted; (b) one-hour QPE MFB adjusted.

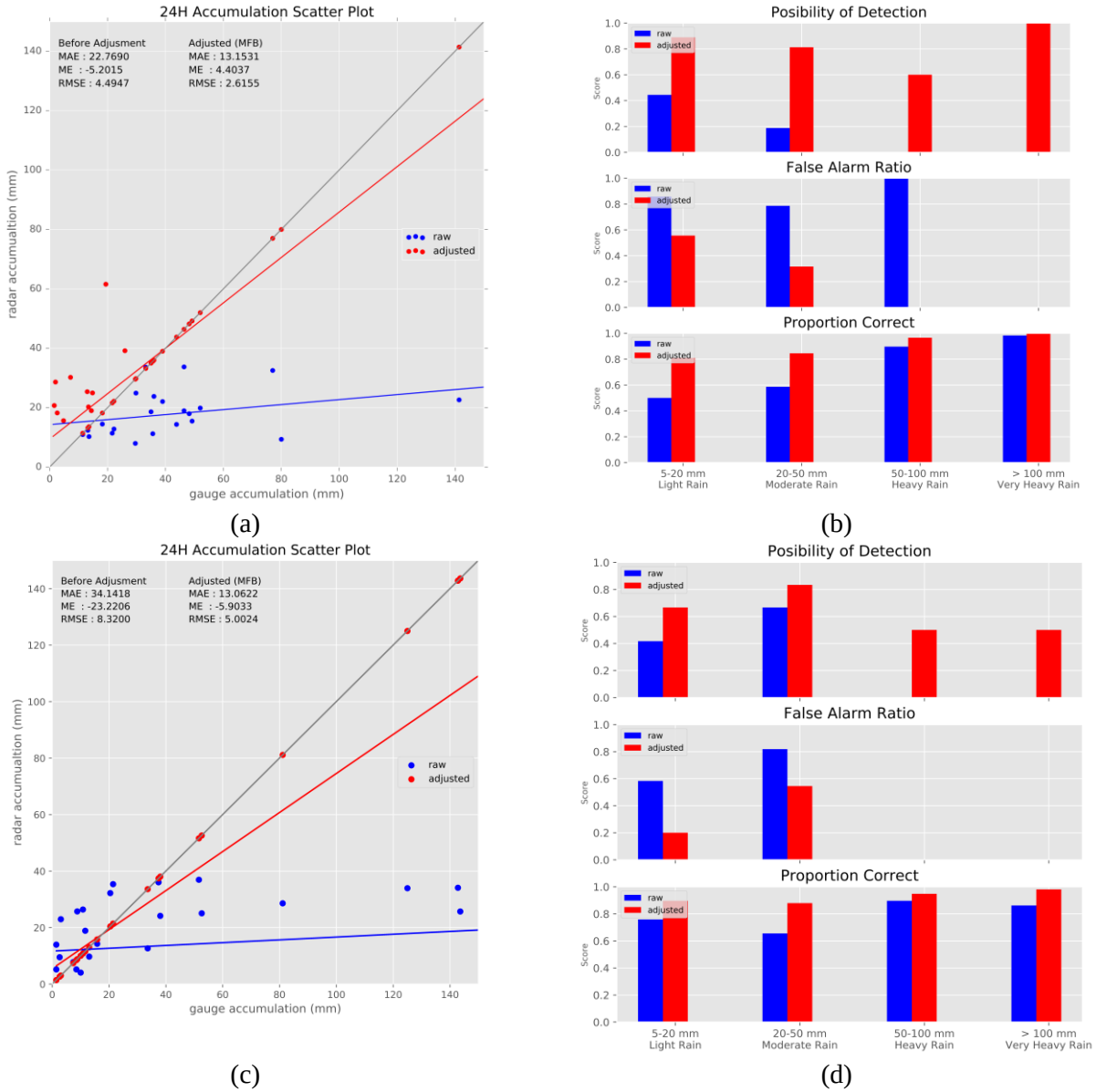

Figure 3-2: Scatter plot verification at all gauge used. The adjustment results a decreasing error value (a). Scatter plot verification for the first case (17 March 2019) while (c) for the second case (19 March 2019). (b) Contingency verification for the first case while (d) for the second case.

These results indicate that MFB adjustment can give better results in accumulation estimation. The RMSE value after MFB adjustment shows that the standard deviation of the residual between radar and gauge observations is only around 2.6 mm. Estimation accuracy is reinforced by the decreasing value of the MAE. The error value decreases about 40–60% compared to unadjusted radar accumulation (from 22.76 mm to 13.15 mm for the first case, and from 34.14 mm to 13.06 mm for the second case). This is a very good result, indicating that the adjusted radar QPE shows little error at a high spatial resolution.

Contingency table verification is performed for the adjustment process, and the values of POD, FAR and PC before and after MFB adjustment are shown in Figure 3-3. When the radar one-day accumulation value gives the same value as the accumulated rain-gauge data, this is counted as a hit. A value is considered as a miss when the estimation is overestimated or underestimated compared to the selected

rainfall accumulation classification. For example, moderate rain is observed by a gauge (accumulation of 30 mm/day) but the radar accumulation estimates more than 50 mm/day or less than 20 mm/day, this will be considered as a miss. POD can represent the radar's ability to detect the specific rainfall classification, while FAR describes how often the radar gives overestimated values.

Before rain-gauge data is merged, the first case gives the value of POD for each category (light rain, moderate rain, heavy rain, and very heavy rain) as 0.45, 0.33, 0 and 0, respectively. After MFB adjustment is applied, the POD values become 0.91, 0.83, 0.6 and 1.0. For the second case, the values of POD for unadjusted QPE at each category are 0.42, 0.67, 0 and 0 and after adjustment become 0.67, 0.83, 0.50 and 0.50.

There are quite large improvements of the POD calculations. The low POD value of unadjusted radar QPE in all rain categories is due to the underestimation of accumulation. There is no successful detection of heavy and very heavy rain events, as shown by the two zero POD values. After the adjustment is performed, all rain classes have more than 0.5 POD. This increment is coupled with PC score and accompanied by decrement in FAR score. Before the adjustment, FAR value for one-day accumulation exceeds 0.85, 0.76, 1.0 and 0 for the first case for each rain category. These values are quite high, and again, underestimation in accumulation is causing this. The decrement is compelling, with the adjustment decreasing FAR scores to 0.57, 0.46, 0 and 0 for light rain, moderate rain, heavy rain, and very heavy rain, respectively. For the second case, unadjusted QPE gives FAR values of 0.52, 0.82, 0 and 0 for each rain category, becoming 0.20, 0.55, 0 and 0 after adjustment.

4 CONCLUSION

The results of the rain-gauge adjustment to the hourly radar QPE and continued to the one-day QPE show significant incremental improvement in performance. Although the adjustment method does not take into account the distance of rain gauges from the radar pixels, the error value can be reduced significantly, by approximately 40%. The performance also improves more than 50% in all rain categories. The number and density level of rain gauges also significantly affects the correction process, with higher density of the rain-gauge network providing more significant correction. The presence of the rain-gauge selection filter is also influential on the adjustments. It is necessary to carry out further research into adjustment methods by taking into account rain-gauge distance to the radar pixels.

ACKNOWLEDGEMENTS

The data in this research is fully supported by BMKG Weather Radar Data Management Subdivision. The paper was improved by the helpful suggestions of Dr Hidde Leijnse from KNMI Netherlands. The author wishes to thank everyone who helped with this research.

AUTHOR CONTRIBUTIONS

An Enhancement to The Quantitative Precipitation Estimation Using Radar-Gauge Merging. Lead Author: Abdullah Ali, Co-Author: Gumilang Deranadyan and Iddam Hairuly Umam.

REFERENCES

Aghakouchak, A., Habib, E., & Bardossy, A. (2010). Modeling radar rainfall estimation

uncertainties: Random error model. *J. Hydrol. Eng. 15*, 265–274.

Chumchean, S., Sharma, A., & Seed, A. (2006). An integrated approach to error correction for real-time radar-rainfall estimation. *J. Atmos. Ocean. Tech., 23*, 67–79.

Germann, U., Galli, G., Boscacci, M., & Bolliger, M. (2006) Radar precipitation measurements in a mountainous region. *Q. J. Roy. Meteor. Soc. 132*, 1669–1692.

Goudenhoofdt, E., & Delobbe, L. (2009). Evaluation of radar-gauge merging methods for quantitative precipitation estimates. *Hydrol. Earth Syst. Sci., 13*, 2975–3003.

Joss, J., & Wadvogel, A. (1990). Precipitation measurement and hydrology. In D. Atlas (Ed.), *Radar in Meteorology: Battan Memorial and 40th Anniversary Conference on Radar Meteorology*, (pp. 577–606). Boston, MA: American Meteorology Society.

Krajewski, W. F. (1987). Cokriging of radar-rainfall and rain gauge data. J. *Geophys. Res., 92*, 95719580.

Lack, S. A., & Fox, N. I. (2007). An examination of the effect of wind drift on radar-derived surface rainfall estimations. *Atmos. Res., 85*, 217–229.

Pereira Fo, A. J., Crawford, K. C., & Hartzell, C. L. (1998). Improving WSR-88D hourly rainfall estimates, *Weather Forecast., 13*, 10161028.

Seo, D. J., & Breidenbach J. P. (2006). Real-time correction of spatially nonuniform bias in radar rainfall data using rain gauge measurement. *J. Hydrometeorol., 3*, 67–69.

Selex SI (2017). *Rainbow5 Product and Algorithm, Software Manual* 4, (pp. 127–128).

Sokol, Z. (2003). Utilization of regression models for rainfall estimates using radar-derived rainfall data and rain gauge data. *J. Hydrol., 278*, 144–152.

Sun, X., Mein, R. G., Keenan, T. D., & Elliott, J. F. (2000). Flood estimation using radar and rain-gauge data. *J. Hydro., 239*, 4–18.

Tabary, P. (2007). The New French Operational Radar Rainfall Product. Part I: Methodology. *Weather Forecast., 22*, 393–408.

Todini, E. (2001). A Bayesian technique for conditioning radar precipitation estimates to rain-gauge measurement. *Hydrol. Earth Syst. Sci., 5*, 187199.

Villarini, G., Mandapaka, P. V., Krajewski, W. F., & Moore, R. J. (2008). Rainfall and sampling uncertainties: A rain gauge perspective. *J. Geophys. Res., 113*. doi:10.1029/2007JD009214.

Wilson, J. W., & Brandes, E. A. (1979). Radar measurement of rainfall – A summary. *B. Am. Meteor. Soc., 60*, 1048–1058.

Wu, S. J., Hsu, C. T., Lien, H. C., & Chang, C. H. (2015). Modeling the effect of uncertainties in rainfall characteristic flash flood warning based on rainfall thresholds. *Nat. Hazards, 75*(2), 1677–1771.

Wu, S. J., Lien, H., Chsu, C. T., Chang, C. H., & Shen, J. C. (2015). Modeling probabilistic radar rainfall estimation at ungauged location based on spatiotemporal errors which correspond to gauged data. *Hydrol. Sci., 46*(1), 39–59.

Zhu, D., Xuan, Y., & Cluckie I. (2014). Hydrological appraisal of operational weather radar rainfall estimates in the context of different modelling structures. *Hydrol. Earth Syst. Sci., 18*, 257272.

OPTIMIZATION OF A RICE FIELD CLASSIFICATION MODEL BASED ON THE THRESHOLD INDEX OF MULTI-TEMPORAL LANDSAT IMAGES

Made Parsa [1]*, Dede Dirgahayu, Sri Harini, Dony Kushardono
Remote Sensing Application Center
Jln. Kalisari No. 8, Pekayon, Pasar Rebo, Jakarta 13710
*email: made.parsa@lapan.go.id
Received: 5 May 2020; Revised: 12 August 2020; Approved: 14 August 2020

Abstract. The development of rice land classification models in 2018 has shown that the phenology-based threshold of rice crops from the multi-temporal Landsat image index can be used to classify rice fields relatively well. The weakness of the models was the limitations of the research area, which was confined to the Subang region, West Java, so it is was deemed necessary to conduct further research in other areas. The objective of this study is to obtain optimal parameters of classification model of rice and land based on multi-temporal Landsat image indexes. The study was conducted in several districts of rice production centers in South Sulawesi and West Java (besides Subang). The threshold method was employed for the Landsat Image Enhanced Vegetation Index (EVI). Classification accuracy was calculated in two stages, the first using detailed scale reference information on rice field base, and the second using field data (from a survey). Based on the results of the analysis conducted on several models, the highest accuracy is generated by the three index parameter models (EVI_min, EVI_max, and EVI_range) and adjustable threshold with 94.8% overall accuracy. Therefore this model was acceptable for used for nationally rice fields mapping.

Keywords*: multi-temporal, EVI, threshold, optimization*

1 INTRODUCTION

The Decree of The Ministry of Agrarian Affairs and Spatial Planning (ATR)/Head of National Land Agency (BPN-RI) No.339 of 2018 dated October 8, 2018 shows that the area of rice fields in Indonesia in 2018 was 7,105,145 hectares, down from 7,750,999 hectares in 2013. Meanwhile the 2016 data show that the area of rice fields in South Sulawesi Province was 656,610 Ha of which were irrigated fields and the remaining 40 % (262,767 Ha) were non-irrigated/rainy lowland. The irrigated rice fields consists of 83.5% PI 2 (rice cropping twice a year); 8.0% IP 3 (rice cropping three times a year) and 7.6% PI 1(rice cropping once a year). The remaining 0.8% are other crops or not cropped. The distribution of irrigated rice fields is mostly found in Maros, Pinrang, Bone, Sidrap, Luwu, Wajo, East Luwu, and Soppeng Regencies. 64.1% of non irrigated rice fields are PI 1, 32.9% PI 2, 1.3% PI 3, and the remaining 1.6% are other crops or not cropped (South Sulawesi Provincial Government, 2016).

Parsa, *et al.*, 2019 state that rice fields can be easily recognized on optical images because they have different characteristics compared to other land uses. In the original Landsat-8 channel 6 (SWIR),5 (NIR),4 (Red) color composite image, for example, rice fields cropped with rice are easily identified based on key interpretations, with three different types of appearance. Rice fields will appear blue when in a state of

http://dx.doi.org/10.30536/j.ijreses.2020.v17.a3333

watering/tillage up until the beginning of cropping), will turn green during the vegetative/generative phase and then turn red after harvest/fallow.

Research by Parsa et al. (2013), in cited in Parsa et al. (2019) mentioned that statistical analyzed of the NDVI multi-temporal (mean, maximum, and minimum value) can be used to make RGB image composite. Based on image, demonstrating that they were able to provide a contrasting appearance between rice crops and other crops, due to the real effect of the difference between the maximum and minimum NDVI values. The results of this identification indicate that of the four index values, the mean value is the most significant effect for mapping rice fields compared to the other three indices. Combining the four multi-temporal statistical value (NDVI) criteria can be used for rapid digital mapping of rice fields (rice) with an accuracy of 87.4%.

The research of Chen et al. (2011) used Chinese HJ-1A/B Environmental Satellite Imagery (30 m spatial resolution) to monitor rice cultivation areas in Guangdong province in southern China. Temporal The NDVI characteristics of lowland rice were analyzed in the study to monitor changes in lowland NDVI. Their results indicate that the Chinese Environmental Satellite HJ-1A/B had great potential in developing an operating system to monitor the growth of rice in South China. Research using MODIS and Landsat 8 imagery to map rice in the Panjin Plain, Northeast China produced a map at a spatial resolution of 30m built on pixel-based and phenology algorithms in rice field and wetland areas. A validation test showed high accuracy of rice rice map. Comparison of the map with others showed a high level of consistency and that it provided more detailed information about the distribution of rice fields because of its higher spatial resolution. The resulting rice map was evaluated with in-situ soil data and Google Earth images. The estimated overall accuracy and coefficient of kappa were 95% and 0.90 respectively (Zhou et al. 2016, in Parsa et al. 2019).

Based on the above description, optimization research and classification parameters of rice fields based on the phenology of rice crops have been developed, as reflected in the vegetation index using EVI (Enhanced Vegetation Index) of multi-temporal Landsat imagery. The purpose of this study is to obtain optimal parameters from the classification model of rice fields based on the phenology of rice crop EVI multi-temporal Landsat imagery. Through the research, it is expected that optimal parameters and thresholds can be obtained for the classification of rice fields in order to support the operational activities of monitoring rice phases more accurately.

2 MATERIALS AND METHODS

2.1 Location and Data

The study was conducted by taking the objects of several districts in the provinces of South Sulawesi and West Java. The data used were every scene during one year (2018) of Landsat-8 data from USGS in the Google Earth Engine (GEE) Cloud System. In addition, supporting data were used, namely detailed scale (1: 5000) maps of rice fields from the national Mapping Agency (BIG, 2017) and data from field survey results.

2.2 Standardization of Data

The satellite data used is the atmospherically corrected surface reflectance of the Landsat 8 OLI/TIRS sensors from USGS which can be accessed using the GEE platform. These

images contain five visible and near-infrared (VNIR) bands and two short-wave infrared (SWIR) bands, processed to orthorectify surface reflectance, and two thermal infrared (TIR) bands processed to orthorectify brightness temperature.

Vegetation Index of EVI can be obtained by using the following formula :

$$EVI = 2.5 \times \frac{\rho_{nir} - \rho_{red}}{\rho_{nir} + 6 \times \rho_{red} - 7.5 \times \rho_{blue} + 1} \quad (2\text{-}1)$$

If Red < NIR OR Blue < Red Else EVI = 1.5*(NIR – Red)/(0.5 + Nir + Red) (Kontgis *et al.*, 2015; Dong *et al.*, 2016; Zhou *et al.*, 2016; Dirgahayu, D., 2016)

2.3 Methods

The research is a follow-up study, therefore the method used follows that of the previous research (Parsa et al., 2019). Method development was undertaken by conducting further analysis of pixels that were not included in the rice field class (adjustment). The phased examination of the classification results was based on the range of EVI values of the mean and standard deviations, assuming the distribution was close to normal. The statistical value of each parameter (EVI Max, EVI Min, EVI Range, and EVI Mean) was calculated on the LBS that is definitely known to be a rice field. The range of EVI parameter values used are presented in Table 2-1. The results of the classification of each combination of parameters were tested in two stages, first using the reference data for Rice Field Base (LBS) and second using survey data (Kushardono, 2017; Hestie *et al.*, 2017). Considering the results of the classification and reference data have a raster format, the test is raster to raster. While the field data is point data, the second stage is a point to point test by paying attention to the 8 pixels around it, forming a 3x3 pixels area of satellite data used. The LBS reference data used in 2017 were the result of verification by a team led by BIG (BIG, 2017). Field data in this study were obtained in two ways: first, a field survey conducted in the South Sulawesi region, which included 358 sample points in ten districts. Field data retrieval was made by direct and indirect observation (using drones). Verification for the West Java region was made by comparing the results of the classification with Google data in four districts. The sample points were made using the Systematic Random Sampling method. The first point was determined randomly while the next point is determined systematically with a distance of 2.5 km south-north and west-east (Figures 2-1 and 2-2).

Table 2-1: Range of EVI parameter values

Parameter	1 Stdev.		1.5 Stdev.		2.0 Stdev.		2.5 Stdev.		Adjustment	
	Lower limit	Upper limit	Lower limit	Upper limit	Lower limit	Upper limit	Lower limit	Upper limit	Lower limit	Upper limit
EVI_Min	-0.113	0.170	-0.184	0.241	-0.254	0.311	-0.325	0.382		0.188
EVI_Max	0.373	0.428	0.359	0.441	0.345	0.455	0.331	0.469	0.350	
EVI_Mean	0.177	0.297	0.147	0.327	0.117	0.357	0.087	0.388	0.236	0.400
EVI_Med	0.184	0.301	0.155	0.331	0.126	0.360	0.096	0.389		
EVI_Range	0.243	0.500	0.179	0.565	0.114	0.629	0.050	0.693		

Figure 2-2: Distribution of sample points for West Java (blue, purple, green, and brown points)

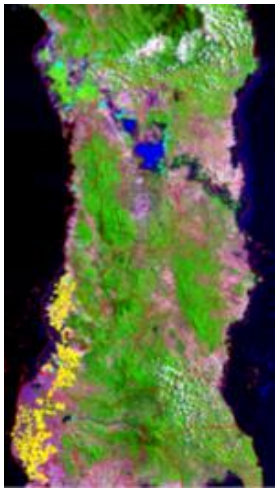

Figure 2-1: Distribution of field sample points for South Sulawesi (yellow and cyan points)

3 RESULTS AND DISCUSSION

In the research, several combinations of parameters of EVI statistical value have been conducted and for the classification of rice fields in South Sulawesi and West Java. In the EVI composite image of rice fields planted with rice, these appear green, with bright to dark gradations. This is due to using three EVI values, namely average, maximum and minimum, as shown in Figure 3-1. The results are presented in Figures 3-2 to Figure 3-13.

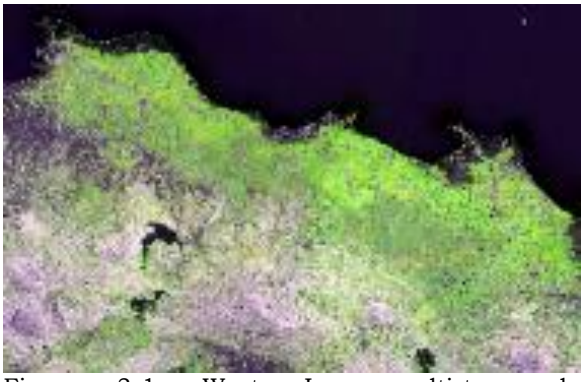

Figure 3-1: West Java multi-temporal composite EVI (mean, max, min) image, January-December 2018

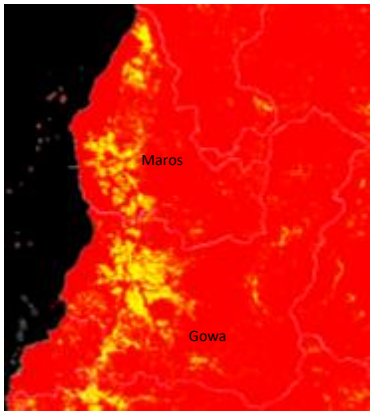

Figure 3-2: Results of the classification of rice fields based on EVI (min, max, mean) stdev 1.0 Maros and Gowa, 2018

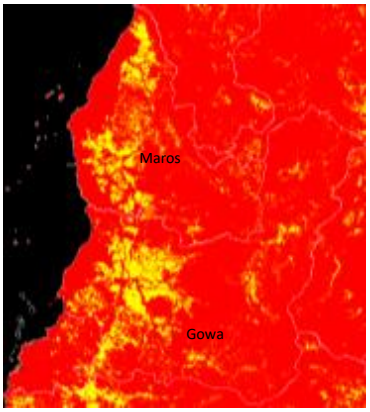

Figure 3-3: Results of the classification of rice fields based on EVI (min, max, mean) stdev 1.5 Maros and Gowa, 2018

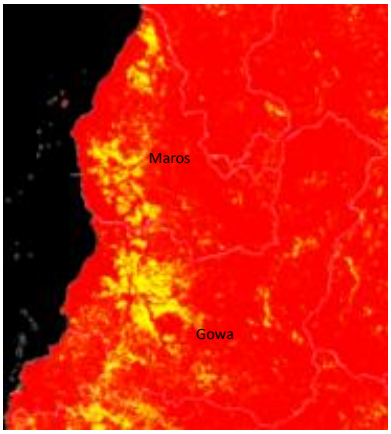

Figure 3-4: Results of the classification of rice fields based on EVI (min, max, range, mean) stdev 1.0, Maros and Gowa, 2018

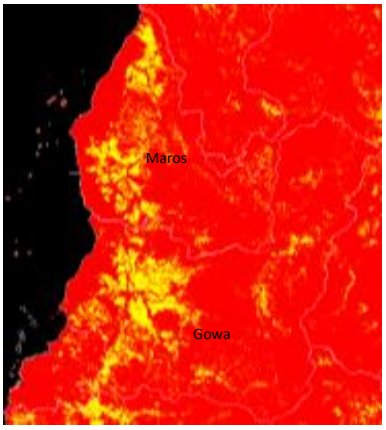

Figure 3-5: Results of the classification of rice fields based on EVI (min, max, range, mean) stdev 1.5, Maros and Gowa, 2018

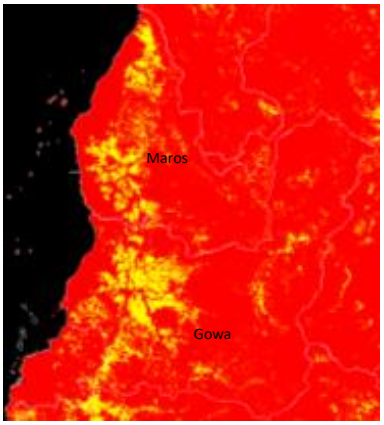

Figure 3-6: Results of the classification of rice fields based on EVI (min, max, mean) threshold are adjusted, Maros and Gowa, 2018

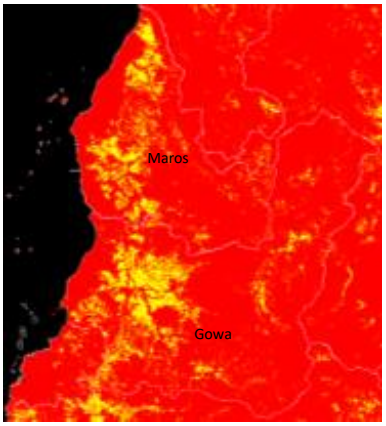

Figure 3-7: Results of the classification of rice fields based on EVI (min, max, range, mean) threshold adjusted, Maros and Gowa, 2018

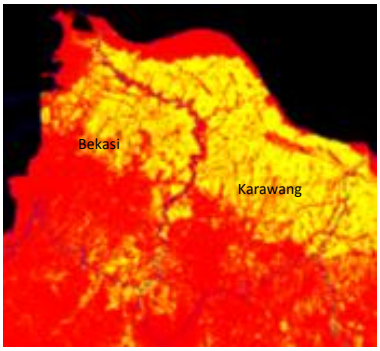

Figure 3-8: Results of the classification of rice fields based on EVI (min, max, mean) stdev 1.0 Bekasi and Karawang, 2018

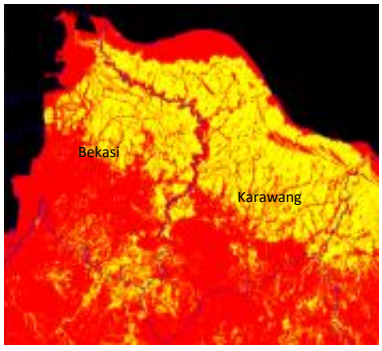

Figure 3-9: Results of the classification of rice fields based on EVI (min, max, mean) stdev 1.5 Bekasi and Karawang, 2018

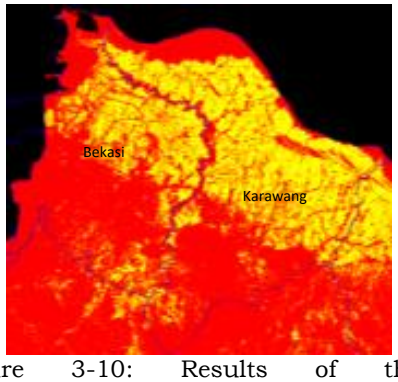

Figure 3-10: Results of the classification of rice fields based on EVI (min, max, range, mean) stdev 1.0 Bekasi and Karawang, 2018

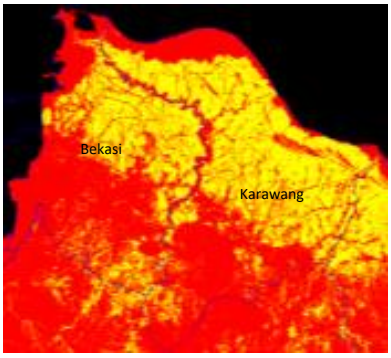

Figure 3-11: Results of the classification of rice fields based on EVI (min, max, range, mean) stdev 1.5 Bekasi and Karawang, 2018

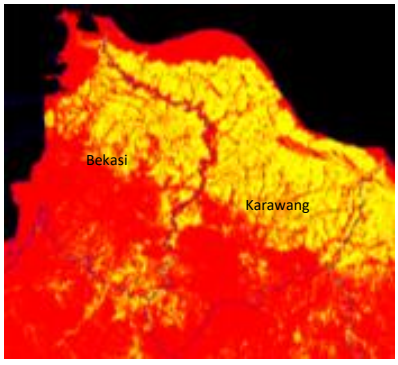

Figure 3-12: Results of the classification of rice fields based on EVI (min, max, mean) threshold adjusted Bekasi and Karawang, 2018

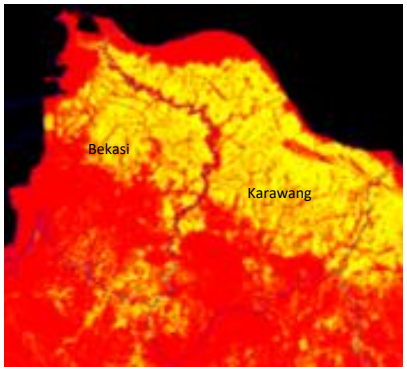

Figure 3-13: Results of the classification of rice fields based on EVI (min, max, range, mean) threshold adjusted Bekasi and Karawang, 2018

Information: Area in red: non-rice fields, yellow: rice fields

Examples of the accuracy analysis of the classification results are presented in Tables 3-1 and 3-2.

Table 3-1: Example of accuracy analysis based on LBS

		CLASSIFICATION	
	CLASS	**Ricefield**	**Nonrice**
LBS	Ricefield	8,917,475*	1,384,475
	Nonrice	130,307	8,949,943
	Overal Accuracy		92.18%

Description *= pixels

Table 3-2: Example of accuracy analysis based on data sample

		CLASSIFICATION	
	CLASS	**Ricefield**	**Nonrice**
LBS	Ricefield	455**	26
	Nonrice	1	148
	Overall Accuracy		95.71%

Description **= sum of point sample

The results of the two stages of testing the accuracy of all models are presented in Table 3-3. The table 3-3 above shows that the LBS-based data accuracy has the same tendency, while the thee parameter classification model has a higher level of accuracy (although not significant) compared to the four parameter model one. Judging from the standard deviations used, it is seen that 1.5 STDEV results in higher accuracy than the 1.0 threshold. For adjusted threshold treatments, higher accuracy is a result of a combination of three rather than four EVI parameters. This shows that the research has not been able to find the optimal threshold value for the treatment of the four EVI parameters, because logically greater number of

parameters used should produce better accuracy. On the other hand, the classification results tested with the field data show a slightly different trend, with the highest accuracy still from the adjusted threshold treatment (94.75%); followed by the treatment of four EVI parameters (min, max, range, mean) 1.5 stdev at 94.11% then four EVI_ parameters (min, max, range, mean) threshold adjusted at 93.78%; and with the lowest treatment being three EVI_ parameters (min, max, range) 1.0 stdev, at 85.85%.

When viewed as a whole from the results of the two testing techniques, it is shown that in general the classification model tends to be similar to the LBS data. A mismatch between the results of the classification model and LBS can be seen in several locations (Figures 3-13-3-15).

Table 3-3: Accuracy of the rice classification model based on the LBS data and field data for the South Sulawesi and West Java regions

Clasification Models	**Total Accuracy (%)**	
	Based on LBS Data	**Based on Field Data**
EVI_(min, max, range) 1.0 stdev	91.04	85.85
EVI_(min, max, range) 1.5 stdev	94.73	93.60
EVI_(min, max, range, mean) 1.0 stdev	90.89	86.60
EVI_(min, max, range, mean) 1.5 stdev	90.70	94.11
EVI_(min, max, range), adjustable threshold	94.15	94.75
EVI_(min, max, range, mean), adjustable threshold	93.30	93.78

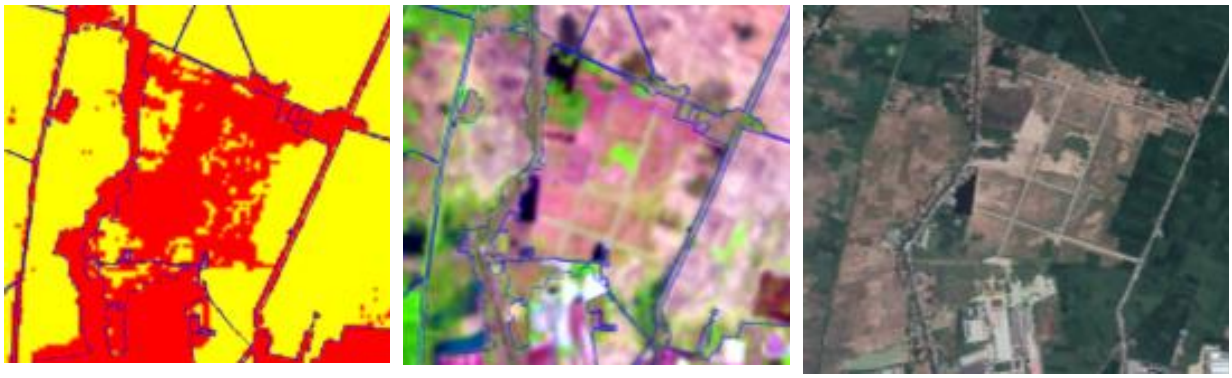

(a) (b) (c)

Figure 3-13 (a,b,c): One of the locations where there is a difference between the results of the model classification with LBS; a) the results of the classification are overlapped with LBS (blue vector), b) Landsat-8 imagery September 8, 2018; and c) high resolution imagery (Google, July 7, 2018).

(a) (b) (c)

Figure 3-14 (a,b,c): a) high resolution imagery 11 September 2016; b) 12 November 2016; and c) 26 July 2017

Source: Google

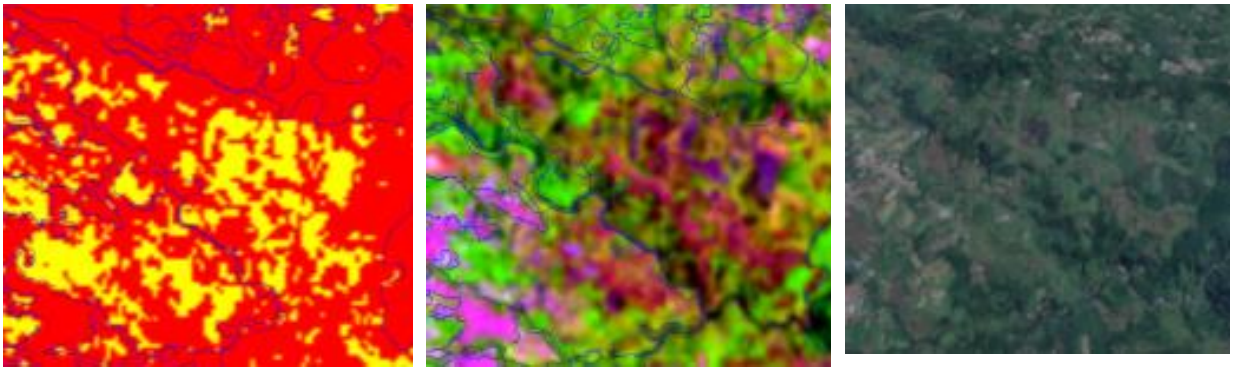

(a) (b) (c)

Figure 3-15: One of the two locations where there are differences between the results of the model classification with LBS; a) the results of the classification are overlapped with LBS (blue vector); b) Landsat-8 imagery September 8, 2018; and c) high resolution imagery (Google, July 7, 2018).

The difference here is estimated to be due to its location, being in the process of land conversion, and for which LBS map updates in this section are missing. This is clearly seen from the high resolution data for 2016-2017 (Figure 3-14 a, b, c).

A difference is also seen in the second location (Figure 3-15) which is estimated to be rainfed lowland mixed with non-rice. On the LBS map, this area is used as a class for all rice fields, which can be seen from the high resolution data of 7 July 2018 (Figure 3-15c). It can therefore be concluded that the classification model of rice land based on the multi-temporal Landsat image index is relatively accurate. Maximum accuracy is produced by a three-parameter model (min, max, range) with the following criteria: EVI_Min <= 0.344; EVI_Max> 0.328; EVI_Range> 0.104; threshold adjusted to an overall accuracy of 94.75%.

4 CONCLUSION

Based on the results of the analysis and discussion that have been presented, it can be concluded that:

a. Optimal parameters were obtained from the classification model of rice fields based on the phenology of rice crops (EVI vegetation index) multi-temporal Landsat imagery.

b. The optimal parameter for the classification of rice fields is use of the EVI min, max, range with adjusted threshold.

c. More in depth study needs to be conducted to obtain the optimal combination of parameters and thresholds to produce maximum classification accuracy.

ACKNOWLEDGMENTS

The author grateful for the collaboration of all the parties who helped conduct the research, including the Remote Sensing Data and Technology Center, which provided satellite imagery data; the Program Fields and Remote Sensing Utilization Centers, which helped with survey equipment; and its operators and resource people from BPTP South Sulawesi, who helped with the field data collection.

AUTHOR CONTRIBUTIONS

Optimization Of A Rice Field Classification Model Based On The Threshold Index Of Multi-Temporal Landsat Images. Lead Author: I Made Parsa and Dede Dirgahayu. Co-Author: Sri Harini and Dony Kushardono.

REFERENCES

Badan Informasi Geospasial, (2017), *Kick off meeting rice fields verification*. Available at: http://www.big.go.id/ berita-surta/show/. Accessed 25 January 2018

Dirgahayu, D., Noviar, H. dan Anwar, S., (2014), *Model pertumbuhan tanaman padi di pulau sumatera menggunakan data EVI modis multi-temporal*. Seminar Nasional Penginderaan Jauh Tahun. 21 April 2014. IPB International Convention Center. Bogor.

Dirgahayu, D., (2016). The new method for detecting early cropping and bare land condition in rice field by using vegetation-bare-water index. Proceedings of the 2nd International conference of Indonesian Society for Remote Sensing (ICOIRS), 2016, Yogyakarta. ISBN: 978-602-73620-1-7, 331-142.

Dong, J., Xiao, X., Menarguez, M.A., Zhang, G., Qin, Y., Thau, D. … More, B. III, (2016). Mapping rice rice cropping area in northeastern asia with landsat 8 images, fenologi-based algorithm and Google Earth Engine. Remote Sensing of Environment 185 (2016), 142-154.

Hestie, T., Tibshirani, R., & Fridman, J., (2017). The elements of statistical learning data mining, inference, and prediction. (2nd Ed.). Stanford, California: Springer.

Kontgis, C., Schneider, A., Ozdogan, M. (2015). Mapping rice rice extent and intensification in the Vietnamese mekong river delta with dence time stacks of Landsat data. Remote Sensing of Environment 169 (2015), 255-269.

Kushardono, D. (2017). Klasifikasi Digital Pada Penginderaan Jauh. Cetakan 1, November 2017. IPB Pres. Bogor. 75 p.

Parsa, I.M. & Dirgahayu, D., (2013). Multi-temporal vegetation index of Landsat image analysis for rice field quick mapping (rice crop), case study of Tanggamus, Lampung. *Internasional Journal of Remote Sensing and Earth Sciences*. 10(1), 19-24.

Parsa, I.M. & Dirgahayu, D. dan Harini, S. (2019*). Pengembangan metode klasifikasi lahan sawah berbasis indeks citra landsat multiwaktu. Jurnal Penginderaan Jauh Dan Pengolahan Data Citra Digital,* 16(1), 35-44.

Pusat Teknologi dan Data Penginderaan Jauh, Lembaga Penerbangan dan Antariksa Nasional. Available at: www://bdpjn-catalog.lapan.go.id/ catalog/index.php, Accessed 31 January 2019.

Qin, Y., Xiao, X., Dong, J., Zhou, Y., Zhu, Z., Zhang, G. … Li, X. (2015). Mapping rice rice cropping area in cold temperate climate region through analysis of time series Landsat 8 (OLI), Landsat 7 (ETM+) and MODIS imagery. *ISPRS Journal of Photogrammetry and Remote Sensing* 105 (2015), 220-233.

South Sulawesi Provincial Government, (2016). Luas lahan sawah menurut Kabupaten/Kota (hektar). Available at: https://sulselprov.go.id/upload/files/1-Lahan%20Sawah%20Total.pdf. Accessed 14 November 2019.

Zhou, Y., Xiao, X., Qin, Y., Dong, J., Zhang, G., Kou, W. … Li, X. (2016). Mapping rice rice cropping area in rice-wetland coexistent areas through analysis of Landsat 8 OLI and MODIS images. *International Journal of Applied Earth Observation and Geoinformation* 46, 1-12.

UTILISATION OF NASA - GFWED AND FIRMS SATELLITE DATA IN DETERMINING THE PROBABILITY OF HOTSPOTS USING THE FIRE WEATHER INDEX (FWI) IN OGAN KOMERING ILIR REGENCY, SOUTH SUMATRA

Hermanto Asima Nainggolan[1], Desak Putu Okta Veanti[2]*, and Dzikrullah Akbar[3]
[1]Mahasiswa Program Studi D4 Klimatologi, Sekolah Tinggi Meteorologi Klimatologi dan Geofisika
[2]Dosen Program Studi Klimatologi, Sekolah Tinggi Meteorologi Klimatologi dan Geofisika
[3]Dosen Program Studi Klimatologi, Sekolah Tinggi Meteorologi Klimatologi dan Geofisika
*e-mail: okta.veanti@stmkg.ac.id

Received: 13 September 2019; Revised: 31 August 2020; Accepted:31 August 2020

Abstract. This study examines the link found between the Fire Weather Index (FWI) and the probability of hotspots in Ogan Komering Ilir District, Indonesia. Although meteorological observation in the area is limited, it is possible to utilise NASA - GFWED and FIRMS satellite data to analyse the ability of the FWI to explain hotspot events. The study aims to determine hotspot density based on the FWI for each season. Furthermore, it aims to establish the probability of hotspots based on FWI class and determination to identify the probability of forest fires in Ogan Komering Ilir. FWI data from NASA-GFWED and hotspot data from 2001 to 2016 from FIRMS were employed for the analysis. Conditional probability analysis was used to ascertain the likelihood of hotspots. The highest hotspot density occurs during the late dry season (SON), followed by the early dry season period (June, July, August). Hotspot density during the rainy season is very low. The probability of hotspots is highest during a high to extreme FWI (around 0.1 to 3.8%) and extreme Fine Fuel Moisture Code (0.1 – 6%).

Keywords: *FWI, Hotspots, Forest Fires, Conditional Probability*

1 INTRODUCTION

Forest and land fires are amongst the biggest disasters faced in Indonesia (Rasyid, 2014b). One of the most vulnerable provinces is South Sumatra. Based on data from the International Carbon Accounting System (INCAS), on average a 50,000 hectare area in the region was burned annually in the 12 years between 2001 and 2012. In addition, in 2015 there was a massive forest fire which lasted for weeks, contributing to the amount of greenhouse gasses emitted into the atmosphere, which is rising each year. During the forest fire of 2015, a huge quantity of greenhouse gasses was released, such as (in Gt) 806,406 CO_2, 8,002 CH_4, 96 N_2O, while pollutant emissions were (in Gg) 85,268 CO, 1,168 NOx, 340 SO_2, 3,093 NMVOC, 1,041 NH_3, 259 BC, 1,957 OC, 4,118 $PM_{2.5}$ and 5,468 PM_{10}. (Pribadi & Kurata, 2017)

To prevent forest fires, the government needs to strengthen local governments and the role of non-state actors (Alamsyah, Saptawan, Ermanovida, Yustian, 2019). Disaster management requires solid coordination between government agencies through communication, control and leadership (Budiningsih, 2017). *Badan Meteorologi Klimatologi dan Geofisika* (BMKG) provides information about fire weather to help other agencies to work more efficiently. Therefore, understanding of the relationship between meteorological conditions and fire is needed.

In South Sumatra Province, Ogan Komering Ilir is the region with the most

http://dx.doi.org/10.30536/j.ijreses.2020.v17.a3202

forest and land fire cases. More than 37,000 thousand hectares of forest and land in Sumatra Selatan was burned in 2018, 20,000 hectares of which was in the Ogan Komering Ilir Regency area. (BPBD in CNN Indonesia, 2018). Most of the land in Ogan Komering Ilir is peat; therefore, once a fire ignites, it is hard to control. Achyar et al. (2015) state that Ogan Komering Ilir is categorised as being very vulnerable to fire.

Forest and land fires in Ogan Komering Ilir affect South Sumatra, nearby provinces, and even neighbouring countries, such as Malaysia, Singapore, Brunei Darussalam and Thailand. Smoke produced by peat fires spreads to the surrounding area, disrupting daily activities and causing severe health problems. Moreover, it has been the cause of diplomatic tension between Indonesia and its neighbouring countries.

In general, there are several factors that influence vulnerability to forest and land fires. These include climate parameters (air temperature, rainfall, and humidity), population density, building density, availability of fire extinguishers, availability of water supply, and the presence of peat and wood vegetation. Changes in the value of these factors makes land very vulnerable and makes it very difficult to extinguish any fires (Latifah & Pamungkas, 2013).

Fires are indicated by hotspots downloaded from the NASA Fire Information for Resource Management System (FIRMS). Hotspots are the result of detection of forest and land fires at specific pixel sizes (eg, 1km x 1km), A hotspot can be detected when the satellite is directly above the hotspot in relatively cloud-free conditions using a certain algorithm (Kaufman et al., 2003). In general, hotspots are used as indicators of the potential for forest and land fires, meaning the more hotspots that are indicated, the greater the potential for forest and land fires in particular areas (Autika et al., 2018).

Various studies to determine the chances of forest and land fires based on the fire index have been conducted.

The current fire weather index can be obtained through remote sensing satellites. One of the fire indices obtained using remote sensing technology is the Fire Weather Index (FWI), which is a system that has been developed since the 1960s in Canada. The FWI system consists of six structured fire code components, which describe the effect of weather, soil moisture conditions and the behaviour of a burning fire. The first three fire components are fuel moisture conditions. The next two components are qualitative indicators of the availability of fuel and the rate at which fire spreads when the fuel burns. The final index, FWI, indicates the intensity of the fire and how hard it is to control it once it ignites.

Some countries have used the FWI index to calculate fire potential, such as Argentina, New Zealand and Sweden (Van Wagner, 1974). Several studies have been conducted on the index, one of which compares the FFMC index and the FWI with the fire hazard behaviour system (SPBK) (Heriyanto et al., 2014). Other research (Veanti & Kloster, 2018) estimates the influence of weather parameter variability on changes in forest fires. This study mostly used FFDI. Therefore, the intention is to improve the research by using FWI, which is more complex and explains more diverse aspects by linking climate parameters and forest fires using fire indices.

FWI index data can be downloaded from the Global Fire Weather Database (GFWED) (Field et al., 2016). GFWED comprises eight different sets of FWI calculations, all using temperature, relative humidity, wind speed, and snow depth estimates from the NASA Modern-Era Retrospective Analysis for Research

and Applications, version 2 (MERRA-2) (Rienecker et al., 2011). Fire indicators are hotspots downloaded from NASA FIRMS satellite data.

Although forest and land fires are important, no study has analysed the conditional probability of hotspots based on the FWI in Indonesia. Therefore, this study aims to determine hotspot density based on the FWI and FFMC (Fine Fuel Moisture Code) in each season of December-January-February (DJF), March-April-May (MAM), June-July-August (JJA), September-October-November (SON) and throughout the year. Furthermore, it aims to establish the probability of hotspots based on FWI and

FFMC classes and the suitability of FWI in determining the probability of forest fires in Ogan Komering Ilir.

2 METHOD

2.1 Location

The research location was Ogan Komering Ilir Regency, South Sumatra. Geographically, the district is located at 104° 20' to 106° 00' E and 2° 30' to 4° 15' S. Ogan Komering Ilir Regency covers an area of 19,023.47 Km^2, with a density of 39 people/km2. More than 570,000 hectares of the total area of Ogan Komering Ilir regency is peatland, of which 308,862 hectares is controlled by three private companies. Such peatland means the region is one of the most vulnerable and fire-prone locations, causing huge losses to the communities and companies that work or operate there.

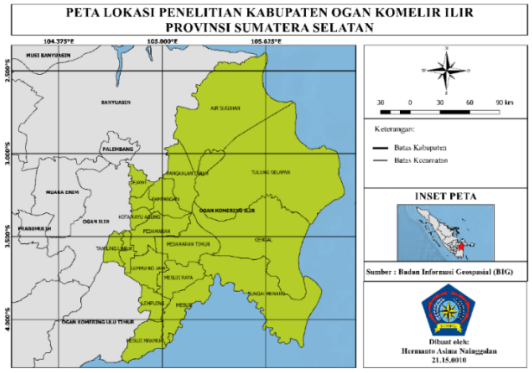

Figure 2-1: Map of Research Locations in Ogan Komering Ilir Regency

Data

The data used in the study can be seen in Table 2-1.

Table 2-1: List of Research Data

No.	Data Type	Data Period	Information
1.	Hotspot	December 1st, 2012 to December 31st, 2018	Data source: NASA-FIRMS. Resolution 1km x 1km
2.	FWI	December 1st, 2012 to December 31st, 2018	Data source: NASA-GFWED. Resolution 0.5^0 x 0.625^0
3.	FFMC	December 1st, 2012 to December 31 st, 2018	Data source: NASA-GFWED. Resolution 0.5^0 x 0.625^0
4.	Observation data of four weather parameters: rainfall, air humidity, wind speed and air temperature	July 1 2015 to November 30, 2016	Data source: Palembang Kenten Climatology Station

In the study, the FWI and FFMC indices from GFWED were verified against those calculated from observational weather parameter data. Because no observations are made in the region, data from the closest climatological station, Palembang Kenten, are used. In addition, the hotspot data are not verified, so only hotspots with a high confidence level (80%) were selected for analysis.

FWI System

To calculate the FWI and FFMC, four weather parameters arere needed as input: air temperature, humidity, 10 meter wind speed observed at 12 pm, and total 24 hour rainfall (Van Wagner, 1974). In addition, the calculation also needs the moisture indices from the previous day.

The FWI system consists of three moisture codes: the Fine Fuel Moisture Code (FFMC), Duff Moisture Code (DMC) and Drought Code (DC). Moisture codes are defined as the value used to calculate the moisture content of fuel in wet or dry conditions. In addition, moisture content is defined as the total mass of water contained in the fuel compared to the total mass of the fuel when it reaches dry conditions without any water in it (Stocks et al., 1989). The moisture code is inversely proportional to its moisture content. An increase in the value of the moisture code means less water content in the fuel. The decreasing rate of fuel moisture occurs exponentially (Van Wagner, 1974).

Table 2-2: Interpretations of the FFMC Class

FFMC Value	Class	Fire Characteristic
0-36	Low	Low possibility of ignition
37-69	Medium	Fire that propagates only on the surface
70-83	High	Fire quickly spreads, or moderate to high fire intensity
> 83	Extreme	Fast spread or high fire intensity, depending on BUI

FFMC is the moisture content from stems, twigs, leaves and other parts of plants that have fallen, and which are generally called fine fuels. The dry weight of these is 0.25kg/m^2, and the depth of the layer ranges from 0 to 5 cm from the ground surface. FFMC is an indicator of how easy a certain area ignites, especially in dry conditions. The FFMC value code is very sensitive to changes in daily temperature and relative humidity. (Van Wagner,1974).

FFMC is divided into four classes, as shown in Table 2-2, which explains the fire characteristics for each FFMC class and its danger rate**.**

The Duff Moisture Code (DMC) is the moisture content of medium-sized wood material or material that has been, or is being, decomposed in the soil. DMC is a layer of fermentation or topsoil on the forest floor. DMC dry weight is around 5kg/m2, and the depth of the layer ranges from 5 to 10 cm below the FFMC layer.

DMC time lag is modeled for around 15 days (Van Wagner, 1974).

The Drought Code (DC) is the moisture content of a solid piece of wood under the surface of the soil. DC has a dry weight of 44kg/m^2, and the depth of the layer ranges from 10 to 20cm under the DMC layer, with a time lag of 52 days (Turner, 1972).

Table 2-3: Interpretation of FWI Value

FWI Value	Class	Fire Characteristics
0-1	Low	Low intensity fire, which will spread slowly, and even extinguish itself.
2-6	Medium	Medium intensity fire. However, it can still be controlled directly using hand tools and water.
7-13	High	High intensity fire. Fire control requires an electric pump and/or the manufacture of firebreaks.
> 13	Extreme	Very high intensity fire, which are very difficult to control.

The next two indices measure fire behaviour and the total fuel available for burning. The first is the Initial Spread Index (ISI), which is a numerical index which estimates the rate of fire spread after ignition in very flammable areas. The ISI estimates the effects of wind and FFMC on the rate of fire spread and illustrates how fires will spread shortly after igniting, without consideration of the influence of available fuels. The second index is the BuildUp Index (BUI), which comprises the FWI components that take into account the total amount of fuel to be consumed based on a combination of DMC and DC components. The final component, the Fire Weather Index (FWI) is a numerical rating of fire intensity. It combines the Initial Spread Index and the Buildup Index, and is suitable as a general index of fire danger (Van Wagner, 1974).

The FWI is divided into four classes (low, medium, high, extreme), as shown in Table 2-3, and explains fire intensity.

Conditional Probability

Observation data using the Pearson correlation method was used to determine the feasibility of the data in representing inadequate observation data. If the correlation between FWI and FFMC obtained from remote sensing results and that obtained from observational weather data has a significant value, then the FWI and FFMC data are considered suitable for use in research.

Ogan Komering Ilir Regency was divided into several grids, with each grid 0.625 x 0.5 degrees in size. The division was based on the resolution of the FWI and FFMC data from the remote sensing system, so that spatial analysis could be performed more efficiently. The research area can be seen more clearly in Fig. 2-2.

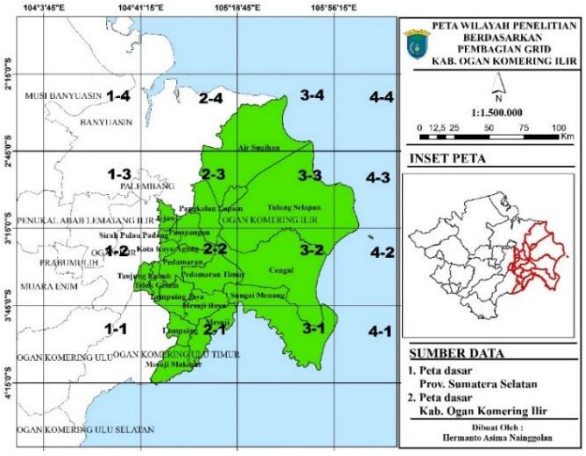

Figure 2-2: Map of the study area divided into grids sized 0.625 x 0.5 degrees

The grids included in the research area are ones which cover the land area of the Ogan Komering Ilir district. Eleven grids were produced, which are the focus of the research area and are designated 1-2, 2-1, 2-2, 2-3, 2-4, 3-1, 3-2, 3-3, 3-4, 4-2 and 4-3.

The downloaded hotspot data were regridded at a resolution of 0.5 x 0.625 per grid to match the resolution of the FWI data. The number of hotspots per grid is considered to be 1 if there is a fire event and 0 if there is no fire event. Note that if more than one event occurs on the same day, the hotspot value is still considered to be 1.

Probability is a value that is used to measure the level of occurrence of a random event, with the scale measured in a range of 0 to 1. The probability of 0 means an event is unlikely to occur, and the probability of 1 means an event must occur (De Groot et al., 2012).

If event A are hotspots, then the climatological probability of the event is P(A). Then, if FFMC and FWI are considered as event B, with the probability P(B), conditional probability can be determined. Conditional probability is the possibility that event B will occur, provided that event A has occurred first. Conditional probabilities are used in this study to determine which indexes in the range of values will produce a specific number of hotspots in an area of the grid. Conditional probability includes a condition that can limit the sample space for an event. The conditional probability notation is expressed by:

$$P(B|A) = \frac{P(A \cap B)}{P(A)} \quad (3\text{-}1)$$

The probability of a "B" event is required by an "A" event. Conditional probabilities occur naturally in a study in which the results of a trial can affect those of subsequent trials. If the probability of an event changes when we consider the first event, then it can be said that the probability of event B occurring depends on the occurrence of event A (Pourghasemi et al., 2012).

Conditional probability is used as a method of determining the probability of a hotspot based on the FWI interpretation value. Symbol "A" represents the probability of a hot spot, while symbol "B" represents the value of the FWI interpretation. Therefore, conditional probability states the probability of a hotspot occurring with certain FWI values.

3 RESULTS AND DISCUSSION

Data Comparison

FWI data and FFMC observations were calculated based on weather parameters such as rainfall, air temperature, humidity and wind speed. The four types of data were then processed based on the FWI and FFMC calculation formulas from Van Wagner (1974) to obtain the required index values. The FWI and FFMC observation data were then correlated using Pearson correlation with the FWI and FFMC data from GFWED. The correlations of the two types of data are shown in the distribution plot graph in Fig. 3-1.

Figure 3-1: Correlation graph of FWI and FFMC satellite data and observation data

Daily observational data for 519 days from 1 July 2015 to 30 November

2016 were used. The correlation between the observational FWI and FFMC and the data from GFWED was positive. Therefore, the fire indices derived from observation and those from GFWED had a statistical relationship. The value of R^2 on FWI was 0.8207, while that on FFMC was 0.4422. These correlation values were considered large enough for the FWI and FFMC reanalysis data to represent the FWI fire index for the research in the Ogan Komering Ilir district.

Seasonal Distribution of Hotspots

Figure 3-2 shows that the distribution of hotspots in Ogan Komering Ilir in each season. During the second half of the dry season in Indonesia (September, October and November), the concentration of hotspots is at its highest. This is similar to the results from Meiriza et al. (2017), who found that the "Based on temporal aspects most hotspots occurred on August, September, and October in South Sumatera with hotspots data from 2005 to 2015.

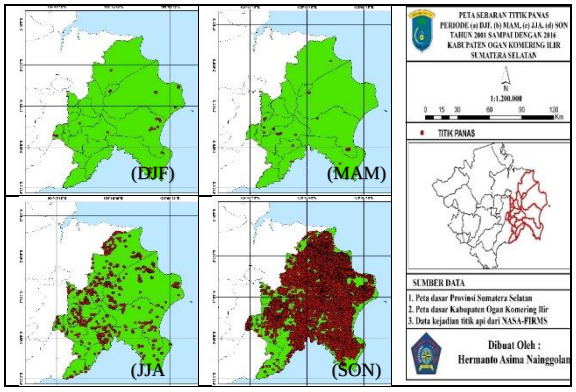

Figure 3-2: Distribution of hotspots in each seasonal period

The concentration of hotspots varied between the different areas. The number occurring indicates how vulnerable a point is, and how often it has experienced a forest fire. The densest hotspots are in grid 1-2, and the sparsest in grid 4-2. This situation is possibly because only a small portion of the Ogan Komering Ilir district is represented on the grid. With regard to grid 4-2 having the fewest hotspots, this due to the fact that almost all of the grid is located in the ocean, with the land area bing only a small part.

Conditional Probability Analysis

The probability of hotspots occurring during certain FWI and FFMC events is shown in Table 6, which indicates the probability for each FWI and FFMC class. Low FWI/FFMC indicates that the weather conditions are not suitable for fires, while the extreme class shows the opposite. This study found a close relationship between the probability of hotspots and FWI/FFMC indices. The highest hotspot probability is found in high or extreme FWI classes. Consequently, extreme classes of FFMC always show the highest hotspot probability (Table 3-1). The non-existence of hotspots during low FFMC is because ignition is impossible. However, although there is a possibility that fires might take place during low to medium FWI or during medium to high FFMC, Ogan Komering Ilir is more vulnerable during high to extreme FWI and/or extreme FFMC. Therefore, the influence of atmospheric conditions on forest fires is clear.

Table 3-1: Hotspot probability for each class of FWI and FFMC on the 11 Ogan Komering Ilir district grids

	FWI					FFMC				
GRID	Low	Medium	High	Extreme	TOTAL	Low	Medium	High	Extreme	TOTAL
1-2	2.7	2.6	3.2	1.8	10.4	0.0	1.9	2.5	6.0	10.4
2-1	0.4	0.5	1.0	2.8	4.7	0.0	0.3	0.6	3.8	4.7
2-2	0.7	1.3	2.3	3.3	7.6	0.0	0.5	1.2	5.9	7.6
2-3	0.5	1.1	2.4	1.9	6.0	0.0	0.3	0.9	4.7	6.0
2-4	0.5	1.1	2.4	1.9	6.0	0.0	0.3	0.9	4.7	6.0
3-1	0.4	0.9	1.2	3.8	6.2	0.0	0.3	1.0	4.9	6.2
3-2	1.0	1.2	1.7	3.0	7.0	0.0	0.8	1.4	4.8	7.0
3-3	0.6	1.0	2.3	3.0	6.9	0.0	0.5	1.1	5.2	6.9
3-4	0.3	0.5	1.3	2.4	4.5	0.0	0.3	0.6	3.6	4.5
4-2	0.1	0.1	0.1	0.1	0.3	0.0	0.1	0.1	0.1	0.3
4-3	0.2	0.2	0.4	1.3	2.1	0.0	0.2	0.2	1.7	2.1

Even so, studies which compare the influence of climatological conditions and human activities on forest fires are still needed. Ones which have confirmed the influence of human activities on forest fires (Tuhulele, 2014; Mapilata, et al. 2013) and those which have verifed the impact of atmospheric conditions (Aflahah, 2019; Syaufina, 2018) have already given us strong evidence of the relationship between forest fires, human activities and natural causes. However, the interplay between all the factors is less understood and needs further research.

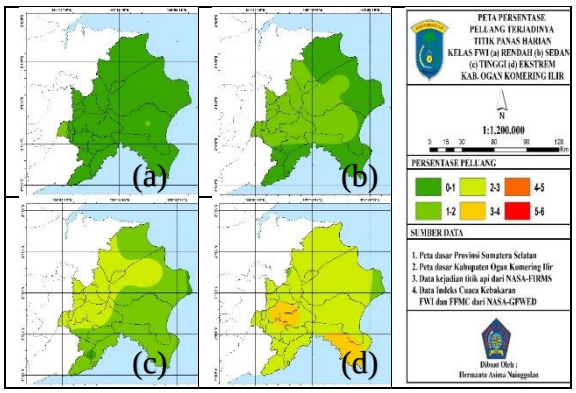

Figure 3-3: Probability of daily hotspots based on the FWI index for each class: (a) low, (b) medium, (c) high, (d) extreme

The four images shown in Figure 3-3 are the results of interpolation from the probability of the occurrence of hot spots for each class on the eleven grids in Ogan Ilir Regency. From the four maps, the low and medium classes show a smaller chance of hot spots compared to the high and extreme classes. The highest probability is in the range of 3 to 4 percent for the extreme FWI class (orange), while for the high class, the highest odds are in the range of 2 to 3 percent. For the middle class, most have a 1 to 2 percent chance, and in the low class most only have a 0 to 1 percent chance in almost all regions of Ogan Komering Ilir Regency.

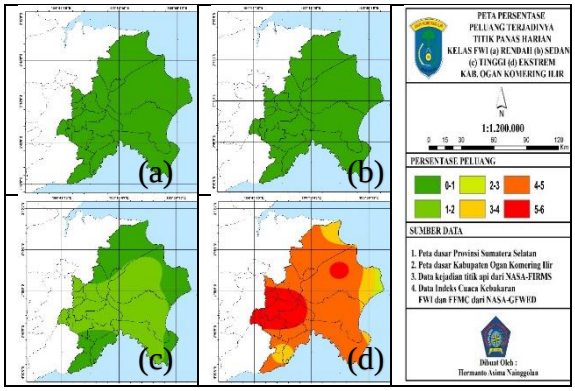

Figure 3-4: Probability of daily hotspots based on the FFMC index for each class: (a) low, (b) medium, (c) high, (d) extreme

In particular, the low FFMC class on the whole grid has a 0% probability. Statistically, there is absolutely no chance of a hotspot occurring in the low class over the whole grid. Meanwhile, the range is 0 to 1 percent for medium FFMC. For high FFMC, the chance of hotspots in all regions is higher than in the previous class (in the range of 2 to 3 percent). On

the other hand, the extreme FFMC class shows significant differences when compared to the previous class. In the extreme FFMC class all regions show a chance of hotspots of above 3 percent, with the highest percentage of opportunities being in the range of 5 to 6 percent in some regions (shown in red).

The rate of hotspot occurence varies between seasons. The density of hotspots for each season can be seen in Figures 3-5 to 3-14.

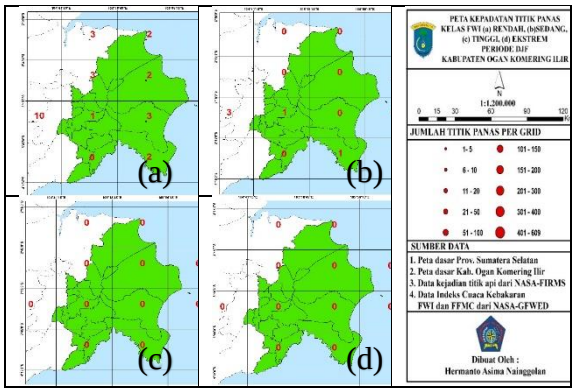

Figure 3-5: Hotspot density December, January, February (DJF) period. FWI class:
(a) low (b) medium (c) high (D) extreme

In the DJF period (December January February) the density of hotspots in each grid is very low. This is in line with the results of Prayoga et al. (2017). However, it can be seen that in this season, hotspots actually occur in low and moderate FWI classes. This is interesting, because the high and extreme FWI classes actually did not experience any hotspot events at all, while the low and moderate classes did experience hotspot events, with even the low class densely packed with hotspots.

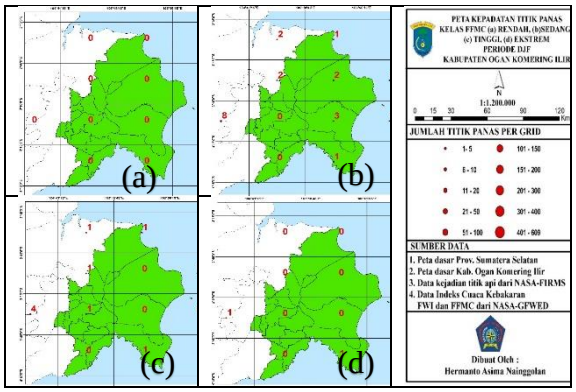

Figure 3-6: Hotspot density December, January, February (DJF) period. FFMC class:
(a) low (b) medium (c) high (D) extreme

IN the DJF FFMC index period (December, January and February), the most numerous hotspots were in the medium class, followed by the high class. In the low class there are no hotspots at all, and in the extreme class just one occurence. Compared to the FWI index, in the DJF period there was little resemblance to the points where the hotspots appeared most densely in the class that should have had the lowest chance of fires.

The general conditions in the DJF period need to be noted. This distribution is normal because this season rarely has high to extreme FWI and FFMC indices due to high rainfall and humidity. Besides, there are only a miniscule number of hotspots, which might not be related to large forest fire events, but to other activities.

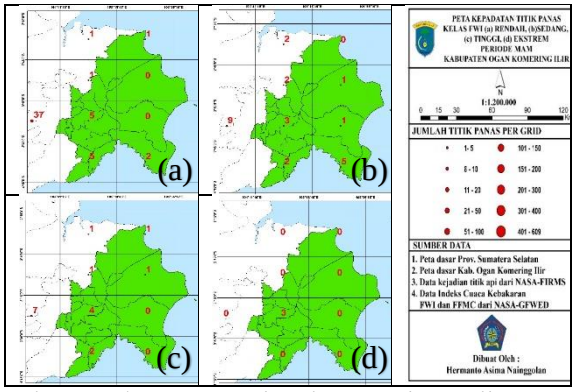

Figure 3-7: Hotspot density March, April, May (MAM) period. FWI class: (a) low (b) medium (c) high (D) extreme

Hotspot density in the MAM period is still small (less than 10), and these are spread evenly across all FWI classes. Hotspots start appearing in several grids in the high and extreme classes.

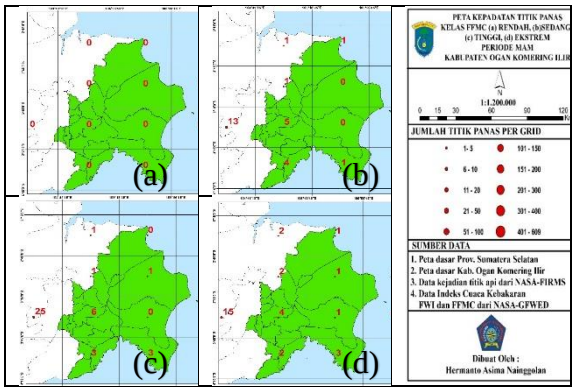

Figure 3-8: Hotspot density March, April, May (MAM) period. FWI class: (a) low (b) medium (c) high (D) extreme

The FFMC maps for the MAM period show higher hotspot densities compared to the DJF period. The number is similar in the medium, high and extreme FFMC. Although MAM is a transitional period from the rainy to the dry season, there is no notable increase in the number of hotspots. This indicates that the fuel is not dry enough and the weather does not support the emergence of forest fire.

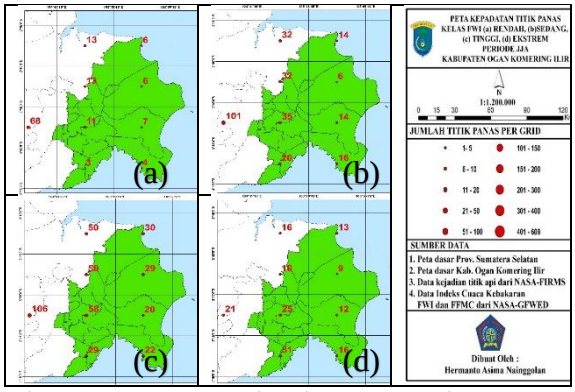

Figure 3-9: Hotspot density June, July, August (JJA) period. FWI class: (a) low (b) medium (c) high (d) xtreme

During the JJA period, the densest hotspots occur on the high FWI map, followed by hotspots on the extreme FWI map. It can be seen that the low and moderate classes also contain hotspots, but their density is lower. Hotspot density in general is higher compared to the previous seasons. During the JJA period, rainfall is low and temperatures are high. Therefore, more hotspots are expected.

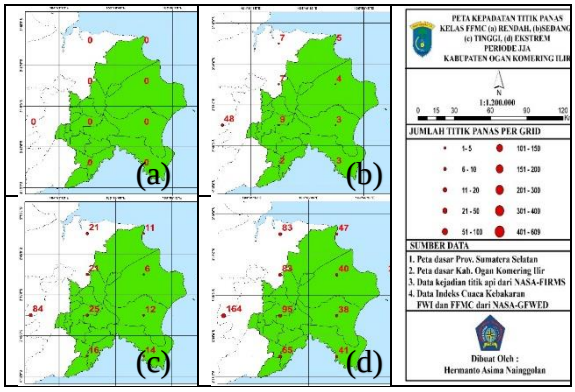

Figure 3-10: Hotspot density June, July, August (JJA) period. FFMC class: (a) low (b) medium (c) high (d) extreme

In the JJA FFMC index, the densest hotspots occur in the extreme class, followed by the high class. Meanwhile, in the middle class, there are still several hotspots. In the low class, no hotspots

occur. The JJA season is characterised by low rainfall, low humidity and high temperatures, resulting in the increase from high to extreme FWI and FFMC. Low rainfall during August was recorded in the study by Meliani et al. (2020). Compared to rainfall in April, in August it is considerably lower. In this period, the FFMC index is increasingly relevant to explain the emergence of hotspots in Ogan Komering Ilir district.

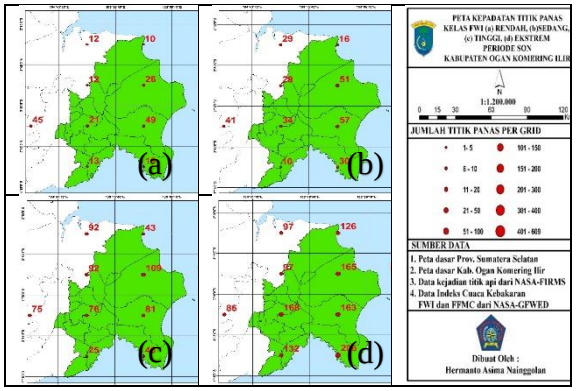

Figure 3-11: Hotspot density September, October, November (SON) period. FWI class: (a) low (b) medium (c) high (d) extreme

In the SON period, the FWI experiences the most intense hotspots in the extreme class, followed by the high class, while for medium and low classes, there are still several hotspots. In this season, over the entire grid the most dominant hotspots occur in the extreme classes. In line with the dry conditions of the season, the FWI index is increasingly relevant to the incidence of hotspots.

In line with the hotspot conditions in the previous FWI index, in the FFMC index the most intense fires occur during the SON season period (September, October and November), with the most dominant in the extreme classes. Hotspots occur relatively frequently in the high class, and several times in the medium class. On the other hand, in the lower classes, there are no fires. The SON season period, which is the dry season shows that the FFMC index is more suitable for the hotspot events in Ogan Komering Ilir district.

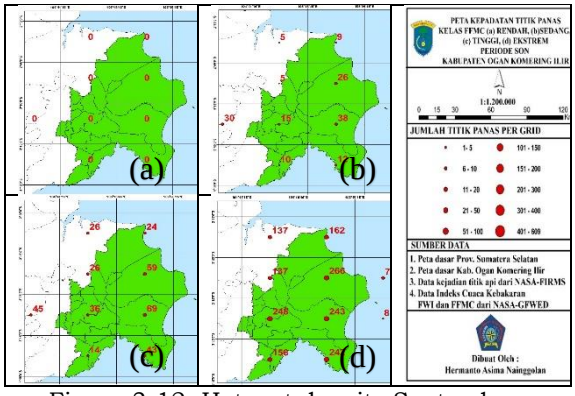

Figure 3-12: Hotspot density September, October, November (SON) period. FFMC class: (a) low (b) medium (c) high (d) extreme

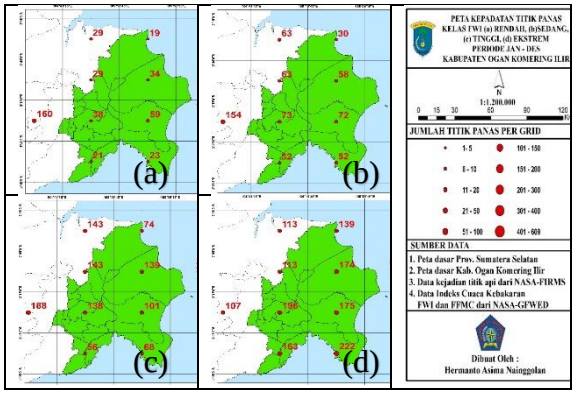

Figure 3-13: Comparison of FWI interpretation classes January-December seasons. (a) low (b) medium (c) high (d) extreme

The FWI index throughout the year, from January to December, has the most intense hotspots in the extreme class, followed by the high class. Hotspots occur several times in the low and moderate classes, but do not dominate. For this reason, the FWI index is generally suitable with regard to the occurrence of hotspots. When it shows values that are in the range of the high or extreme classes, the potential for hotspots is very high.

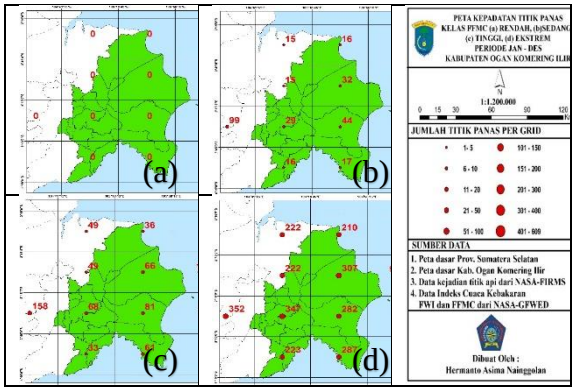

Figure 3-14: Comparison of FFMC interpretation classes January-December:
(a) low (b) medium (c) high (d) extreme

On the FFMC index throughout the year, the densest hotspot events occur in the extreme classes, followed by the high classes. Several hotspots occurred in the medium class, but in the low class there were no hotspots. This indicates that the FFMC is relevant to the occurrence of hotspots; when it shows values that are in the high or low class, hotspots have the potential to be relatively large.

4 CONCLUSION

The highest hotspot density takes place during the late dry season (SON), followed by the early dry season (JJA). Hotspot density during the rainy season is very low. The probability of hotspots is highest during high to extreme FWI (around 0.1 to 3.8%) and extreme FFMC (0.1 – 6%). FWI and FFMC can link weather conditions and the occurrence of hotspots well.

ACKNOWLEDGMENTS

The authors would like to thank to God Almighty for his power and wisdom and for enabling us to complete the work successfully. We would also like to thank the STMKG educational institution for providing facilities and support during the process of completing this paper.

AUTHOR CONTRIBUTION

Utilisation of Nasa - GFWED and FIRMS Satellites in Determining the Probability of Hotspots using the Fire Weather Index (FWI) in Ogan Komering Ilir Regency. South Sumatra. Lead author: Hermanto Asima Nainggolan. Co-author: Desak Putu Okta Veanti. Dzikrullah Akbar.

REFERENCES

Achyar, E., Schmidt-Vogt, D., & Shivakoti, G. P. (2015). Dynamics of the multi-stakeholder forum and its effectiveness in promoting sustainable forest fire management practices in South Sumatra, Indonesia. *Environmental Development*, *13*, 4-17.

Aflahah, Elania, Rini Hidayati, & Rahmat Hidayat. (2019). Pendugaan hotspot sebagai indikator kebakaran hutan di Kalimantan berdasarkan faktor iklim [Hotspot estimation as an indicator of forest fires in Kalimantan based on climatic factors]. *Jurnal Pengelolaan Sumberdaya Alam dan Lingkungan (Journal of Natural Resources and Environmental Management) 9*(2), 405-418.

Alamsyah, A., Saptawan, A., Ermanovida, E., & Yustian, I. (2019). Actor Networking in Forest Fires Mitigation, Ogan Komering Ilir District, South Sumatra Province, Indonesia. *JKAP (Jurnal Kebijakan dan Administrasi Publik)*, *23*(2), 92-108.

Budiningsih, Kushartati. (2017). Implementasi Kebijakan Pengendalian Kebakaran Hutan Dan Lahan Di Provinsi Sumatera Selatan. *Jurnal Analisis Kebijakan Kehutanan 14*(2), 165-186.

DeGroot, Morris H., & Mark J. Schervish. (2012). *Probability and statistics*. Pearson Education. city of publication missing

Field, R.D., G. van der Werf, T. Fanin, E. Fetzer, R. Fuller, H. Jethva … H.M. Worden. (2016). Indonesian fire activity and smoke pollution in 2015 show persistent nonlinear sensitivity to El Niño-induced drought. *Proc. Natl. Acad. Sci.*, *113*(33), 9204-9209, doi:10.1073/pnas.1524888113.

Heriyanto. E.. Syaufina. L. & effendy. S. (2014). Perbandingan indeks fine fuel moisture code (ffmc) dan fire weather index (fwi) pada sistem peringkat bahaya kebakaran hutan/lahan luaran wrf dengan observasi (periode: juni-agustus 2013). 15.

https://www.cnnindonesia.com/nasional/20181105122259-20-344060/lahan-sumatra-selatan-terbakar-37-ribu-hektare-sepanjang-2018 (accessed Jan 2020).

Incas. (2015). *Sekilas tentang sumatera selatan* [online]. Kementrian lingkungan hidup dan kehutanan republik indonesia. Available: http://www.incas-indonesia.org/id/data/south-sumatra/ [accessed 10 2018].

Kaufman. Y.. Ichoku. C.. Giglio. L.. Korontzi. S.. Chu. D.. Hao. W.. Li. R.-r. & justice (2003), Fire and smoke observed from the earth observing system modis instrument--products. Validation. And operational use. *24*, 1765-1781.

Latifah. R. N. & pamungkas. (2013). Identifikasi faktor-faktor kerentanan terhadap bencana kebakaran hutan dan lahan di kecamatan liang anggang kota banjarbaru. 2**.** C207-c210.

Mapilata, Eko, Komarsa Gandasasmita, & Gunawan Djajakirana. (2013). Analisis daerah rawan kebakaran hutan dan lahan dalam penataan ruang di Kota Palangka Raya, Provinsi Kalimantan Tengah. *Majalah Ilmiah Globe 15*(2)

Meiriza, Alsella, Reza Firsandaya Malik, & Siti Nurmaini. (2017). Spatio-temporal analysis of south sumatera hotspot distribution. *2017 International Conference on Electrical Engineering and Computer Science* (ICECOS). IEEE.

Meliani, F., Sulistyowati, R., Permata, Z. D. O., Sumargana, L., Amaliyah, R., Purwandani, A., ... & Ramadhan, A. R. (2020, June). Preliminary study on validation of HIMAWARI-8 data with ground based rainfall data at South Sumatera, Indonesia. In *IOP Conference Series: Earth and Environmental Science* (Vol. 500, No. 1, p. 012031). IOP Publishing.

Pourghasemi, Hamid Reza, Majid Mohammady, & Biswajeet Pradhan(2012). Landslide susceptibility mapping using index of entropy and conditional probability models in GIS: Safarood Basin, Iran. *Catena 97*, 71-84.

Prayoga, M. Bayu Rizky, & Ardila Yananto. (2017). Analisis korelasi kerapatan titik api dengan curah hujan di pulau Sumatera dan Kalimantan. *Jurnal Sains & Teknologi Modifikasi Cuaca 18*(1), 17-24.

Pribadi, A., & G. Kurata. (2017). Greenhouse gas and air pollutant emissions from land and forest fire in Indonesia during 2015 based on satellite data. *IOP Conference Series: Earth and Environmental Science*, *54*(1). IOP Publishing.

Rasyid, Fachmi. (2014). Permasalahan dan dampak kebakaran hutan. *Jurnal Lingkar Widyaiswara 1*(4), 47-59.

Rienecker, M. M., Suarez, M. J., Gelaro, R., Todling, R., Bacmeister, J., Liu, E., ... & Bloom, S. (2011), MERRA: NASA's modern-era retrospective analysis for research and applications. *Journal of Climate*, *24*(14), 3624-3648.

Stocks, B. J., Lynham. T., Lawson. B. Alexander. M.. Wagner. C. V. Mcalpine. R. & dube. (1989). Canadian forest fire danger rating system: an overview. *65*, 258-265. journal name? Check author names

Syaufina, Lailan, & Dinda Aisyah Fadhillah Hafni (2018), Variabilitas Iklim Dan Kejadian Kebakaran Hutan Dan Lahan Gambut Di Kabupaten Bengkalis, Provinsi Riau [Variability of Climate and Forest and Peat Fires Occurrences in Bengkalis Regency, Riau] *Jurnal Silvikultur Tropika 9*(1), 60-68. don't use capitals for title

Tuhulele, Popi Tuhulele. (2014). Kebakaran Hutan di Indonesia dan Proses Penegakan Hukumnya Sebagai Komitmen dalam Mengatasi Dampak Perubahan Iklim.*Supremasi Hukum: Jurnal Kajian Ilmu Hukum, 3*(2), page numbers missing

Turner. J. (1972), *The drought code component of the canadian forest fire behavior system*. Department of the Environment, Ottawa. On. Ca.

Van wagner. C. E. (1974). *Structure of the canadian forest fire weather index*. Citeseer.tands. 2**.** 34-39. Type of reference not clear. Incomplete? Check font.

Veanti, Desak Putu Okta, & Silvia Kloster. (2018). The change in forest fire danger and burnt area related to the change in meteorological forcing variability. *AIP Conference Proceedings*. *1987*(1). AIP Publishing LLC.

INTERNATIONAL JOURNAL OF REMOTE SENSING AND EARTH SCIENCES

Instruction for Authors

Scope

International Journal of Remote Sensing and Earth Sciences (IJReSES) publishes research results on remote sensing and earth sciences, with special interest in Asian region.

Manuscript Submission

Manuscripts submission to the IJReSES must be original with a clear definition of the objective(s), material used (data), methods applied, results, and should not have been published or offered for publication or submitted elsewhere. The manuscript should be written in English, using single line spacing on single-sided A4 size paper with 2.5 cm left and right margins, 2.5 cm upper and lower margins . The author(s) is (are) also required to submit original version of figures embedded in the paper along with their captions. All figures should be in tiff or jpeg format with high resolution (300 or 600 dpi). Submit your paper in Word to IJReSES secretariat via: jurnal.lapan.go.id.

Manuscript Preparation

- Title should be concise and informative and not exceeding 15 words.
- The author name(s) and affiliation(s) should be written in the footnotes at the bottom of the title page.
- Abstract should contain a summary of the paper including brief introduction, the objective(s), method, and principal conclusions. Abstract should not exceed 250 words. Keywords are between 3 to 5 words and must be relevant to the subject. Do not use any sub-headings.
- Materials and methods used should clearly and concisely describe the experiment with sufficient details for independent repetition.
- Results should be presented with optimum clarity and without unnecessary detail. Results should also be presented in figures or tables but not duplicated in both format. Tables should be typed with same font size as the text and given consecutive Arabic number.
- Discussion should explain the significant findings and other important aspects of the research. Do not repeat material and methodology.
- Citation should be written in the text by the author's last name and year in one or two forms: Field *et al*. (1996) or (Field *et al*., 1996). For references with more than two authors, list the first author plus *et al*.
- Conclusion should be concise and answer the objective(s).
- Acknowledgment, if any, should be kept at minimum (less than 40 words)
- References should be in alphabetical order. It should be written as follows:
  Field, C.B., M.J. Behrenfeld, J.T. Randerson, and P. Falkowski, 1998, Primary production of the biosphere: integrating terrestrial and oceanic components. *Science*, 281(5374):237-240.
- Acronym or uncommon abbreviations must be given in full at the first text mentioned. New abbreviation should be coined only for unwieldy names and should not be used at all unless the names occur frequently.
- Latin name and family of the species should be given besides its common name at the first mention in the manuscript , and the common name only for subsequent mentions.
- International Standard unit system (kg, m, s, etc) should be used for all manuscripts.

International Journal of
Remote Sensing and Earth Sciences

June 2020

Published by:

National Institute of Aeronautics and Space of Indonesia (LAPAN)

Secretariat:
National Institute of Aeronautics and Space of Indonesia (LAPAN)
Jl. Kalisari No. 8, Pekayon, Pasar Rebo, Jakarta 13710, INDONESIA
Telp. (021) 8710065, Fax. (021) 8722733
Pukasi.lapan@gmail.com

INTERNATIONAL JOURNAL OF
REMOTE SENSING AND EARTH SCIENCES
Vol. 17 No. 1 June 2020
P-ISSN 0216-6739; E- ISSN 2549-516X
Accreditation No. 30/E/KPT/2018

Contents

Published by:
National Institute of Aeronautics and Space of Indonesia (LAPAN)